Analysis of Lipids in Kidney Tissue Using High Resolution MALDI Mass Spectrometry Imaging

Dissertation

zur Erlangung des akademischen Grades

doctor rerum naturalium

(Dr. rer. nat.)

im Fach Chemie

eingereicht an der

Mathematisch-Naturwissenschaftliche Fakultät

der Humboldt-Universität zu Berlin

von

Sarah Ahmed Aboulmagd Khodier, M.Sc. Pharmazeutischewissenschaften

Präsidentin der Humboldt-Universität zu Berlin

Prof. Dr.-Ing. Dr. Sabine Kunst

Dekan der Mathematisch-Naturwissenschaftlichen Fakultät

Prof. Dr. Elmar Kulke

Gutachter: 1. PD Dr. Michael G. Weller 2. Prof. Dr. Michael W. Linscheid

Tag der mündlichen Prüfung: 18.06.2018

Berlin

Eidesstattliche Erklärung

Hiermit erkläre ich an Eides statt, dass die vorliegende Arbeit selbstständig und nur unter Nutzung der angegebenen Hilfsmittel angefertigt wurde.

Berlin, den 18.06.2018 Sarah Aboulmagd

Acknowledgments

There are many people whom I would like to thank for the encouragement and support they have given me throughout the course of my PhD.

First, I would like to express my sincere gratitude to my supervisor, Prof. Dr. Michael W. Linscheid for giving me the chance to perform my doctoral studies in his research group. I am very thankful for his encouragement, valuable guidance, and continuous support.

I am also very grateful to Dr. Petra Esperling for her continuous friendly support and great assistance.

I dedicate my deepest appreciation to Dr. Diego Esteban-Fernández for his guidance and all his support to overcome the difficulties throughout my whole PhD. I am also deeply indebted to Dr. Estefanía Moreno-Gordaliza for her competent support and useful suggestions. I am very thankful to Boris Neumann for his expert support, valuable advices, and constructive discussions.

I would like to express my gratitude to Dr. Sebastian Beck for the constructive discussions and useful advices. Also, I would like to express my appreciations to Dr. Violette Frochaux, Dr. Ulrike Hochkirch, Dr. Kathrin Brückner, Dr. Georg Kubsch, Dr. David Benda, Yeliz Akyürek, Dr. Rajko Winkler, Dr. Lena Ruhe, René Becker, Dr. Sabrina Trog, Angelika Woyda, Pablo Loreo Lares, Dr. Kathleen Schwarz, Dr. Gunnar Schwarz, Sandra Walter, Stefanie Ickert and the whole former and current group members for their assistance and helpful discussions.

I would like to specially thank my colleagues, whom their support made this journey enjoyable and memorable. I am grateful to Dr. Ahmed Hussein El-Khatib for his constructive advices and support in the lab work. My special appreciation to my dear friend, Dr. Oleksandra Kuzmich for her advices and our long discussions throughout my PhD. Many thanks to Dr. Yide David He for his advices, especially at the beginning of my PhD. I would also like to deeply thank Dr. Essa M. Saied and Kevin Prause for their help with translating the thesis summary.

I would also like to express my sincere gratitude to the Yousef Jameel Academic Program for the scholarship and continuous support. Special thanks are directed to Dr. Uta Hoffmann for her valuable advices and continuous support throughout my PhD.

Last but not least, I would like to thank my dear husband and best friend, Sameh, for his unconditional love, patience, and constant support. I would like to thank my lovely children, Nadine and Adam, for allowing me to grow into the person who I became today. My heartfelt thanks are due to my wonderful family in Cairo, especially my parents, for their continuous care, and all the help and support which contributed greatly to the fulfillment of this work.

Abstract

Mass Spectrometry Imaging (MSI) has become an indispensable tool for studying the spatial distribution of molecules within a diverse range of complex biological samples. It exploits the advantages of modern mass spectrometers including enhanced sensitivity, mass accuracy, and resolving power to produce images that visually represent tissue biology. This contributes to the understanding of complex biochemical processes by revealing the identity of molecular entities and their tissue distribution.

Since the introduction of MSI, Matrix-Assisted Laser Desorption Ionization (MALDI) has become a dominant imaging method of MS, which proved its usefulness to sort out the complexity of lipid structures in biological tissues. Lipids are particularly suitable for MALDI MSI because they are abundant components of biological tissues, they ionize easily due to their polar head groups, and their molecular weights are generally below 1000 Da, which is optimal for sensitive and high resolution mass analysis.

The mapping of tissue lipids by MSI contributed to the understanding of pathophysiological changes associated with different therapeutic treatments or disease evolution. One example where this aspect could be particularly useful is the toxicity mechanisms of platinum-based therapeutics including the antitumor drug, cisplatin. The role of cisplatin in the treatment of several human malignancies is well-established. However, nephrotoxicity is a limiting side effect that hinders the use of higher doses to maximize its antineoplastic effects. Cisplatin-induced nephrotoxicity involves an acute injury of the proximal tubule, where renal accumulation of cisplatin was found. Also increased lipid peroxidation and impaired cell membrane integrity with altered lipid profile of the kidney were reported.

Previous works have shown that lipid imaging in kidney helped distinguish specific lipids within the kidney substructures and identify alterations occurring during kidney diseases. This evolved the motivation to map the lipid composition of the kidney tissue in cisplatin-treated rats to shed light on the lipid alterations occurring in cisplatin-induced nephrotoxicity and the biochemical and pathophysiological processes involved.

In the first part of this work, a robust method for imaging of lipids in rat kidney sections using MALDI-LTQ-Orbitrap was developed. To enhance the method sensitivity,

evaluating the matrix compound of choice and optimizing the deposition of the matrix solution were considered. Following the developed method, imaging measurements of kidney sections of healthy control and cisplatin-treated rats were performed utilizing the high performance of the Orbitrap mass analyzer. Its high mass resolution and accuracy enabled database assignment of the lipid species based on their exact mass. The identification of lipids was confirmed by on-tissue MS/MS followed by fragment ion imaging. The distribution comparison of renal lipids in control and cisplatin-treated tissues revealed clear differences, which could be correlated to the proximal tubule injury. The findings highlight the usefulness of MALDI MSI as potential complementary tool for clinical diagnostics, which might contribute to the understanding of lipid signaling pathways and mechanisms involved in cisplatin-associated nephrotoxicity.

However, the demonstrated differences in the distribution of kidney lipids in control and cisplatin-treated groups have mainly considered qualitative aspects. The use of ion images for reliable intersample comparison on relative quantitative basis was limited by the variable influence of experimental and instrumental conditions. In addition, sample-originated matrix effects including tissue surface microenvironment, result in inhomogeneous matrix-analyte crystal formation. Consequently, non-linear variability in extraction, desorption and ionization of analytes across the tissue could be found.

Accordingly, the challenge to develop a method for normalization of lipid signals in kidney tissues, arose. The work strategy was designed with the aim to allow relative quantitative comparison of lipid intensity in MALDI imaging measurements of different kidney samples. It utilized a mixture of the MALDI matrix and dual lipid-metal internal standards. To ensure homogenous and reproducible deposition, the mixture was automatically applied by means of a commercially available inkjet printer, avoiding expensive matrix deposition devices. The lipid internal standard was used to normalize the signal intensity of tissue lipids, whereas the metal internal standard allowed to confirm the consistency of the matrix and internal standards application. The latter being monitored by total metal content determination using inductively-coupled plasma mass spectrometry (ICP-MS). Normalization of lipids signals demonstrated excellent image correction with respect to variability of laser energy deposition observed in MALDI tissue imaging measurements. Applying the method to normalize

ion intensities of kidney lipids in control and cisplatin-treated rats successfully enabled the comparison of lipid images in both groups on relative quantitative basis.

The results conclude the ICP-MS-controlled application of matrix and internal standards as crucial, when relative quantitative comparison of MALDI MSI data is intended. They also foresee the use of multimolecular internal standards extended to a wider range of lipid classes to be of great potential for MALDI imaging of tissue lipids, enabling improved pixel-based normalization of different lipid species simultaneously.

Zusammenfassung

Massenspektrometrie Imaging (MSI) hat sich zu einem unverzichtbaren Werkzeug für die Untersuchung der räumlichen Verteilung von Molekülen in einer Vielzahl von komplexen biologischen Proben entwickelt. Es nutzt die Vorteile moderner Massenspektrometer einschließlich verbesserter Empfindlichkeit, Massengenauigkeit und Auflösungsvermögen, um Bilder zu erzeugen, die Gewebebiologie visuell darstellen. Dies trägt zum Verständnis komplexer biochemischer Prozesse bei, indem es die Identität von molekularen Einheiten und deren Gewebeverteilung aufdeckt.

Seit der Einführung von MSI ist die Matrix-unterstützte Laser-Desorption Ionisation (MALDI) zu einer dominierenden Bildgebungsmethode der MS geworden, die sich als nützlich erwiesen hat, um die Komplexität von Lipidstrukturen in biologischen Geweben zu bestimmen. Lipide sind besonders für MALDI-MSI geeignet, da sie Bestandteile von vielen biologischen Geweben sind, sie aufgrund ihrer polaren Kopfgruppen leicht zu ionisieren sind und ihr Molekulargewicht im Allgemeinen unter 1000 Da liegt, was für eine empfindliche und hochauflösende Massenanalyse optimal ist.

Die Kartierung von Gewebslipiden durch MSI trägt zum Verständnis von pathophysiologischen Veränderungen bei, die mit verschiedenen therapeutischen Behandlungen oder der Krankheitsentwicklung zusammenhängen. Ein Beispiel, bei dem dieser Aspekt besonders nützlich sein könnte, sind die Toxizitätsmechanismen von Therapeutika auf Platinbasis einschließlich des Antitumorwirkstoffs Cisplatin. Die Rolle von Cisplatin bei der Behandlung von mehreren malignen Erkrankungen beim Menschen ist gut etabliert. Die Nephrotoxizität ist jedoch ein begrenzender Nebeneffekt, der die Verwendung höherer Dosen zur Maximierung ihrer antineoplastischen Wirkungen verhindert. Cisplatin-induzierte Nephrotoxizität beinhaltet eine akute Verletzung des proximalen Tubulus, wo Nierenakkumulation von Cisplatin gefunden wurde. Auch erhöhte Lipidperoxidation und gestörte Zellmembranintegrität mit verändertem Lipidprofil der Niere wurden berichtet.

Frühere Arbeiten haben gezeigt, dass Lipid-Bildgebung in der Niere dabei hilft, bestimmte Lipide innerhalb der Nierensubstrukturen zu unterscheiden und Veränderungen zu identifizieren, die während der Nierenerkrankungen auftreten. Dies

entwickelte die Motivation, die Lipidzusammensetzung des Nierengewebes in Cisplatin-behandelten Ratten zu kartieren, um Licht auf die Lipidveränderungen zu werfen, die in Cisplatin-induzierter Nephrotoxizität und den beteiligten biochemischen und pathophysiologischen Prozessen auftreten.

Im ersten Teil dieser Arbeit wurde eine robuste Methode zur Darstellung von Lipiden in Rattennierenschnitten mit MALDI-LTQ-Orbitrap entwickelt. Um die Sensitivität der Methode zu verbessern, wurde die Matrixverbindung der Wahl untersucht und die Abscheidung der Matrixlösung optimiert. Nach dem entwickelten Verfahren wurden bildgebende Messungen von Nierenschnitten gesunder Kontroll- und Cisplatin-behandelter Ratten unter Verwendung der hohen Leistung des Orbitrap-Massenanalysators durchgeführt. Dessen hohe Massenauflösung und Genauigkeit ermöglichte die Datenbankzuordnung der Lipidspezies basierend auf ihrer genauen Masse. Die Identifizierung von Lipiden wurde durch MS / MS im Gewebe, gefolgt von Fragment-Ionen-Bildgebung, bestätigt. Der Verteilungsvergleich der Nierenlipide in Kontroll- und Cisplatin-behandelten Geweben zeigte deutliche Unterschiede, die mit der proximalen Tubulusverletzung korreliert werden konnten. Die Ergebnisse unterstreichen die Nützlichkeit von MALDI MSI als potentielles komplementäres Werkzeug für die klinische Diagnostik, das zum Verständnis von Lipid-Signalwegen und Mechanismen, die an Cisplatin-assoziierter Nephrotoxizität beteiligt sind, beitragen könnte.

Die nachgewiesenen Unterschiede in der Verteilung von Nierenlipiden in Kontroll- und Cisplatin-behandelten Gruppen haben jedoch hauptsächlich qualitative Aspekte berücksichtigt. Die Verwendung von Ionenbildern für einen zuverlässigen Vergleich zwischen Proben auf relativer quantitativer Basis wurde durch den variablen Einfluss von experimentellen und instrumentellen Bedingungen begrenzt. Darüber hinaus führen aus den Proben stammende Matrixeffekte, einschließlich der Mikroumgebung der Gewebeoberfläche, zu einer inhomogenen Matrix-Analyt-Kristallbildung. Folglich konnte eine nichtlineare Variabilität bei der Extraktion, Desorption und Ionisierung von Analyten im Gewebe gefunden werden.

Dementsprechend bestand die Herausforderung, ein Verfahren zur Normalisierung von Lipidsignalen in Nierengeweben zu entwickeln. Die Arbeitsstrategie wurde mit dem Ziel entwickelt, einen relativen quantitativen Vergleich der Lipidintensität in MALDI-

Bildgebungs-Messungen verschiedener Nierenproben zu ermöglichen. Es verwendete eine Mischung aus der MALDI-Matrix und zwei Lipid-Metall-internen Standards. Um eine homogene und reproduzierbare Abscheidung zu gewährleisten, wurde die Mischung automatisch mittels eines handelsüblichen Tintenstrahldruckers aufgebracht, wobei teure Matrixabscheidungsvorrichtungen vermieden wurden. Der interne Lipidstandard wurde verwendet, um die Signalintensität von Gewebslipiden zu normalisieren, während der interne Metallstandard die Konsistenz der Matrix und die Anwendung interner Standards bestätigte. Letzteres wird durch Bestimmung des Gesamtmetallgehalts unter Verwendung von Massenspektrometrie mit induktiv gekoppeltem Plasma (ICP-MS) überwacht. Die Normalisierung der Lipidsignale zeigte eine ausgezeichnete Bildkorrektur in Bezug auf die Variabilität der Laserenergieablagerung, die bei MALDI-Gewebebildgebungsmessungen beobachtet wurde. Die Anwendung der Methode zur Normalisierung der Ionenintensitäten von Nierenlipiden in Kontroll- und Cisplatin-behandelten Ratten ermöglichte den Vergleich von Lipidbildern in beiden Gruppen auf relativer quantitativer Basis.

Die Ergebnisse schließen die ICP-MS-kontrollierte Anwendung von Matrix- und internen Standards als entscheidend ab, wenn ein relativer quantitativer Vergleich von MALDI-MSI-Daten beabsichtigt ist. Sie sehen auch die Verwendung von multimolekularen internen Standards, die auf einen breiteren Bereich von Lipidklassen erweitert werden, als großes Potenzial für die MALDI-Bildgebung von Gewebslipiden vor, was eine verbesserte pixelbasierte Normalisierung verschiedener Lipidspezies gleichzeitig ermöglicht.

Contents

1 Introduction 1

1.1 Mass Spectrometry Imaging - MSI 1

1.2 Desorption and ionization techniques in MSI 5

1.2.1 Secondary Ion Mass Spectrometry - SIMS 5

1.2.2 Desorption Electrospray Ionization - DESI 6

1.2.3 Matrix-Assisted Laser Desorption Ionization - MALDI 7

Matrix selection and application 10

Lasers 13

Desorption and ionization 14

Mass analysis 17

MSI software 19

MSI data processing 20

Biological applications of MALDI MSI 23

1.2.4 Laser Ablation Inductively Coupled Plasma - LA-ICP 26

1.3 Multimodal imaging 27

1.4 Lipids and lipidomics 29

1.4.1 Lipids 29

Glycerophospholipids (GPLs) 30

1.4.2 Lipidomics 31

Mass spectrometry-based lipidomics approaches 33

1.4.3 Bioinformatics tools in lipidomics 35

2 Aims and scope 37

3 Results and discussion 39

3.1 Lipid imaging by MALDI LTQ Orbitrap mass spectrometry in kidney sections under cisplatin treatment 39

3.1.1 Overview 39

3.1.2 Histopathological assessment of cisplatin-induced renal damage 40

3.1.3 Evaluation of the matrix of choice 41

3.1.4 Assessment of reproducibility....45
3.1.5 Assignment of lipids....46
3.1.6 The role of high resolution MS (HRMS) and MS/MS imaging....47
3.1.7 Lipid imaging for screening of cisplatin-induced effects....51
3.1.8 Significance of cisplatin-induced alterations of tissue lipids....59
3.1.9 Conclusion and outlook....60

3.2 Dual internal standards with metals and molecules for MALDI imaging of kidney lipids....61

3.2.1 Overview....61
3.2.2 Optimization of printing conditions and customized ink....63
3.2.3 Reproducibility under optimized printing parameters and uniformity of internal standard on-tissue distribution....68
3.2.4 Proof of concept....69
Instrumental drifts....69
Methodological drifts....72
3.2.5 Application for intratissue or intrameasurement correction....76
Effect of the internal standard adduct type and chemical class....76
Structure and condition of the tissue....80
3.2.6 Application for intersample or intermeasurement correction....81
3.2.7 Conclusion and outlook....86

4 Materials and methods....88

4.1 Lipid imaging by MALDI LTQ Orbitrap mass spectrometry in kidney sections under cisplatin treatment....89

4.1.1 Chemicals and reagents....89
4.1.2 Animal treatment and tissue preparation....89
4.1.3 Histological hematoxylin and eosin staining....90
4.1.4 MALDI matrices....90
4.1.5 Matrix application....91
4.1.6 Instrumentation....92
4.1.7 Molecular identification and nomenclature of tissue lipids....93

4.2 Dual internal standards with metals and molecules for MALDI imaging of kidney lipids 93

4.2.1 Chemicals 93

4.2.2 Animals treatment and tissue preparation 94

4.2.3 Matrix- internal standards mixture preparation 94

4.2.4 Inkjet printing of matrix-internal standards mixture 95

4.2.5 MALDI MSI measurements 96

4.2.6 Direct injection and laser ablation ICP-MS analysis 96

Direct infusion ICP-MS 96

LA-ICP-MS 97

5 Abbreviations 99

6 References 101

1 Introduction

1.1 Mass Spectrometry Imaging - MSI

Mass Spectrometry Imaging (MSI) is an innovative development of mass spectrometry which emerged as a promising technique in many areas, including biomedical sciences, material sciences and forensics, owing to its high chemical specificity and relative ease of application[1-3]. MSI techniques were introduced into the biological sciences at the end of the 20th century[4], since then it has witnessed numerous methodological and technological developments and positioned itself in the focus of mainstream mass spectrometry (MS).

MSI could be defined as a label-free molecular imaging technique, which allows *in situ* analysis of molecules in complex biological samples. It provides high-resolution images of biomolecules directly from tissue sections utilizing two important features. The first is the chemical specificity of mass spectrometry, which allows determining the mass of biomolecules (m/z) without prior labelling commonly required for other imaging techniques, such as fluorescence, radioimmunoassays, among others. Secondly, the spatial arrangement of biomolecules in the measured sample could be indicated, allowing visualization of molecular distribution. Hence, MSI made possible the direct identification and localization of a wide range of molecules, including pharmaceuticals, metabolites, lipids, proteins, and peptides on the surfaces of various types of complex samples, in a scale range extending from subcellular dimensions to whole biological systems.

In principle, the imaging process in biological research is carried out by rastering a mass spectrometric microprobe across the sample surface in a predefined pattern. Each spot at which the probe is fired, biomolecules are desorbed and ionized from the surface and a mass spectrum is created, which is stored along with its relative position[5]. Once acquisition is complete, imaging software is employed to create MS images, in which individual ions can be extracted and displayed as a function of intensity versus relative position, where changes in color represent changes in intensity. The general principle of a typical MSI experiment is illustrated in Figure 1.

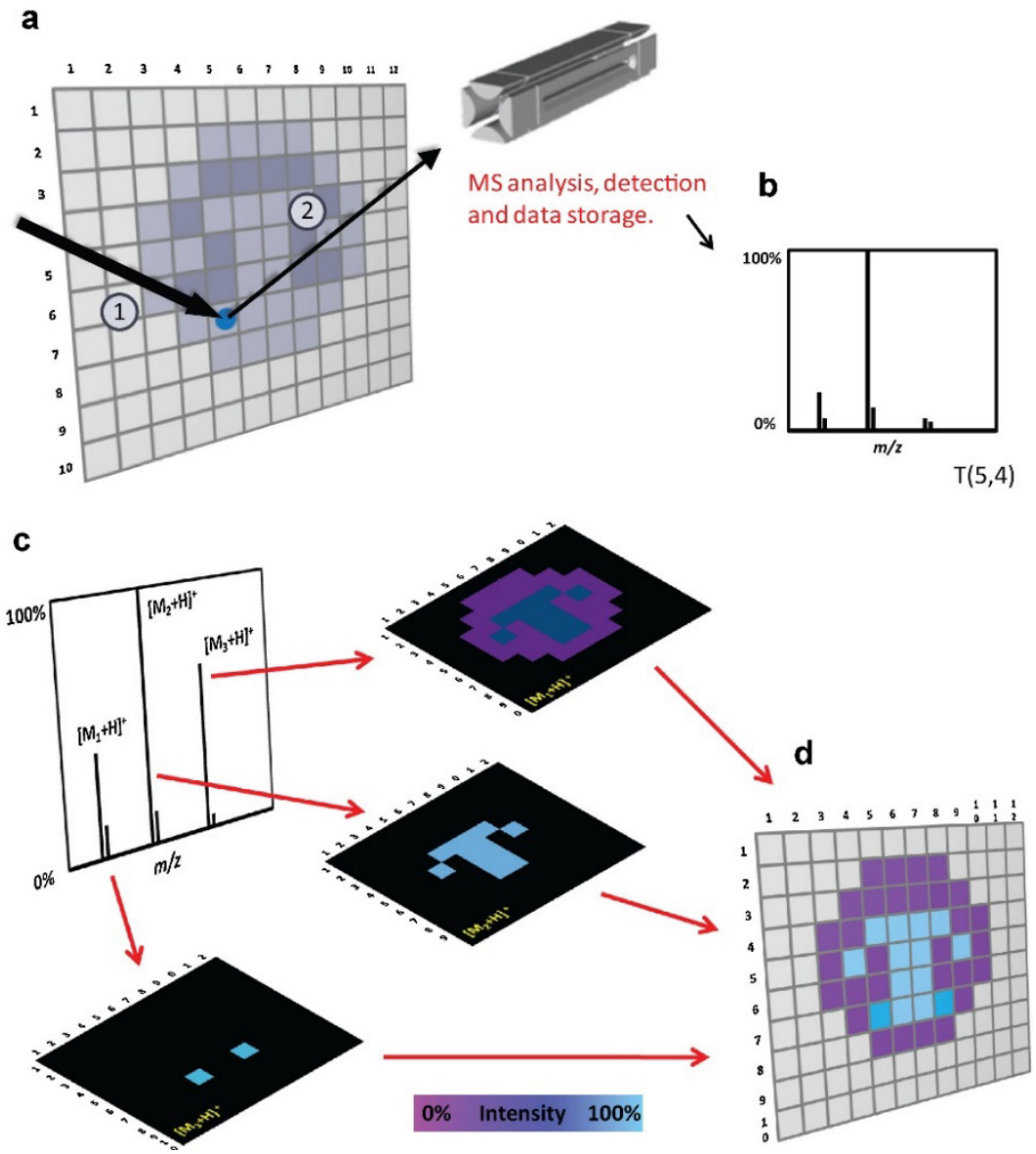

Figure 1. General principle of MSI methods. (a) In a typical MSI experiment, the total area is theoretically subdivided into pixels that are individually inspected (1 and 2 represent the steps desorption and ionization process). (b) For each pixel a single mass spectrum or the average of several mass spectra is collected and stored together with its spatial coordinates. (c) After the entire surface is scanned, an average mass spectrum can be created. The distribution of specific ions can be visualized by the creation of chemical images where the color scale (false color) represents the normalized intensity of particular ions. Each pixel from the image is associated with the original mass spectrum/spectra acquired at the specific point. (d) The aim of imaging is to display the distribution of chemicals across a surface. (Adapted from Wu et al.[1])

A number of desorption and ionization techniques have been introduced in MSI studies of biological samples. The most established ones are matrix assisted laser desorption ionization (MALDI), desorption electrospray ionization (DESI), and secondary ion mass spectrometry (SIMS). Other emerging techniques in MSI exist, which are mostly derivatives or modifications of the major methods listed above, such as nano-DESI, laser ablation electrospray ionization (LAESI), and liquid extraction surface analysis (LESA)[6, 7]. Also, laser ablation inductively coupled plasma MS (LA-ICP-MS) is one of the desorption and ionization techniques that is gaining popularity for MSI. This technique is capable of quantitative imaging of elemental distributions generated from surfaces[3].

Irrespective of the imaging modality, MSI could be generally described as a three-step process which involves sample preparation, data acquisition, and data analysis[1, 3]. All three components should be controlled and optimized to obtain meaningful MSI data. In the following, the three components of MSI are briefly described.

Sample preparation aims mainly at maintaining the integrity and the spatial arrangement of the molecular species within the biological sample. Collection and treatment procedures need to be sufficiently fast to prevent tissue degradation. It is worth to state that sample preparation varies largely depending on the ionization technique. DESI and SIMS require minimal sample preparation, whereas MALDI implies application of the matrix, as will be discussed later with respect to each ionization method. MSI studies reported the use of various types of biological samples, including single cells[8-11] bacterial colonies[12, 13], tissues from different plants[14-17] or animal organs[18, 19] and rodent whole body sections[20-23]. Samples might be fresh, snap-frozen[24], alcohol preserved[25], or formalin-fixed paraffin-embedded (FFPE)[26].

Data acquisition involves the stages of desorption/ionization, mass analysis and ion detection (Figure 1a, b). Desorption and ionization of molecules from the sample surface could be achieved using a laser beam in case of MALDI, a primary ion beam in case of SIMS, or a charged droplet flux in case of DESI (Figure 2).

In MSI, data acquisition is either performed in the microprobe mode or the microscope mode. The microprobe mode is by far more frequently used. In this approach, the surface of the sample is theoretically divided into small areas (pixels). All pixels are

scanned individually in sequence by the desorption/ionization probe, which is adjusted to provide the desired spatial resolution. The data collected from each pixel is represented in a mass spectrum or an average of two or more mass spectra acquired from the specific spot[3]. The alternative microscope mode makes use of astigmatic projection of ions generated at the sample surface to a position-sensitive (two-dimensional) detector, which allows the simultaneous imaging of a larger area. This method allows higher speed of analysis, but the specific ion optics required and the restriction to perform imaging under vacuum conditions limits its application[1].

The ionized molecules are subsequently directed into the mass analyzer where they are separated and detected according to their m/z ratio. Several types of mass analyzers can be interfaced with these desorption and ionization sources including Time Of Flight (TOF), Fourier Transform Ion Cyclotron Resonance (FTICR), linear triple quadrupole, quadrupole ion-trap, or Orbitrap[3].

Data collected from MSI yield high resolution molecular profiles across the tissue. Datasets can contain hundreds to thousands of peaks with data files of up to a few gigabytes[27], which requires complex visualization software. MSI software has been developed to control data processing in order to generate ion images, minimize manual investigation, and provide standardized protocols for routine analysis[3, 28]. FlexImaging and ImageQuest are examples of commercial MSI software, while Biomap, Image J, MSiReader are freely available sources.

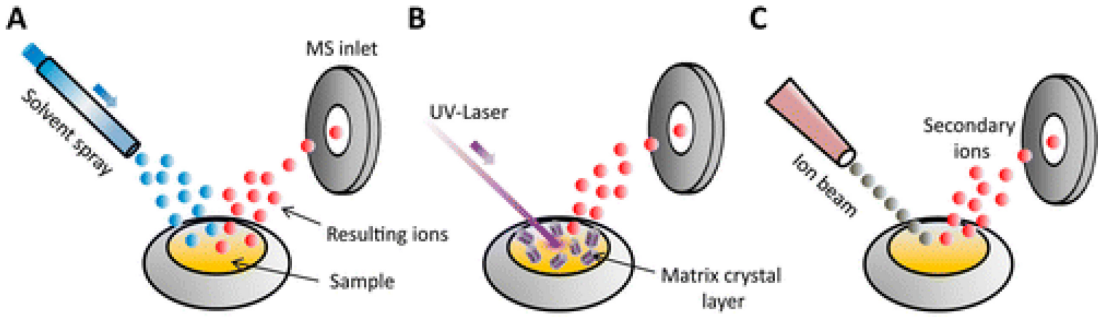

Figure 2. Working principle of different ionization sources in MSI. (A) Desorption electrospray ionization (DESI), (B) matrix-assisted laser desorption/ionization (MALDI), and (C) secondary ion mass spectrometry (SIMS). (Adapted from Addie et al.[7])

1.2 Desorption and ionization techniques in MSI

A recent survey conducted within MSI practitioners showed that MALDI is by far the most utilized technique, while DESI and SIMS are significantly less popular[29]. This section presents an overview on the three molecular MSI methods mentioned above. A brief overview of SIMS and DESI is followed by a detailed discussion of MALDI which is the MSI technique used in this work. In addition, a short description of the elemental MSI method, laser-ablation-inductively coupled plasma (LA-ICP), is given.

1.2.1 Secondary Ion Mass Spectrometry - SIMS

SIMS is a desorption and ionization technique used for MSI which utilizes a primary ion beam (e.g. metal ions) to produce secondary ions from the surface of the sample. The surface of the sample under high vacuum is bombarded with a high energy primary ion beam (typically 5-25 keV)[30]. This primary ion beam can be focused as sharply as 50 nm or less, depending on the primary ion beam current and the charge state of the primary ions[3]. A collisional cascade within ≈ 10 nm of the surface is initiated. The energy transfer to the molecules deposited on the surface causes their extensive fragmentation, since the energy of primary ions is substantially high compared with bond energies of the surface molecules.

When moving away from the primary collision site, less fragmentation occurs and a small fraction of intact molecules is subsequently ejected from the first layers of the surface if the surface binding energy is overcome. Most molecules are emitted as neutrals and only approximately 1% of them are charged, which are called the secondary ions[30]. Both negative and positive secondary ions can be generated depending on the electron configuration of the surface molecules. Primary ions could be either monoatomic (Ar^+, Ga^+, In^+, Au^+, Bi^+) or polyatomic (C_{60}^+, Bi_3^+, Au_n^+)[31, 32]. The latter are considered softer allowing desorption of secondary ions from the sample surface without extensive fragmentation (softer). Consequently, polyatomic ion beams are more suitable for the analysis of intact biomolecules from tissue surfaces and their applications extend to larger molecular weight species[2, 33].

The sample preparation protocol for the SIMS imaging experiment requires only mounting of the tissue section on conductive surface (e.g. indium tin oxide (ITO)-coated glass slide), without further washing steps.

The sample must be stable under high vacuum conditions, which ensures that both the primary and secondary ions travel from their origin to their final destination without undergoing collisions[3]. Due to its excellent spatial resolution capabilities, SIMS applications extended to imaging studies of small biomolecules in unicellular organisms[33], single cells[34], embryos[35], and different organs such as kidney[36] and brain[37]. Limitations of SIMS include the lack of sensitivity of the mass range over 1000 m/z, due to in-source fragmentation of complex molecules. This also results in complex mass spectra which might be difficult to interpret. In addition, commercially available SIMS instruments have limited capability of molecules identification because they have neither the capacity to perform MS/MS fragmentation, nor they provide sufficient mass resolution required for high-resolution imaging[30, 38, 39].

1.2.2 Desorption Electrospray Ionization - DESI

The relatively new ionization method developed by R.G. Cooks in 2004[40], DESI, belongs to the ambient ionization methods, in which ionization occurs at atmospheric pressure with the samples being analyzed in their native state[41].

DESI is a combination of two MS ionization methods: electrospray ionization (ESI) and desorption ionization (DI). It uses energetic charged electrospray solvent droplets to desorb the molecules from the sample surface.

As the charged droplets strike the sample surface, they extract surface-bound analytes that are then desorbed from the surface within scattered secondary droplets. Upon solvent evaporation, these droplets lead to the formation of intact analyte ions that are transported from the surface into the MS inlet[42]. The ionization of biomolecules in DESI takes place in a manner similar to ESI, hence, the soft ionization yields analyte ions with minimal fragmentation which could be multiply charged. The analysis is usually limited to a mass range of 2000 Da and a lateral resolution of about 50 µm[43].

Advantages of DESI include ambient analysis conditions and the possibility to perform tandem mass spectrometry (MS/MS) and accurate mass measurements, which allows the identification of analytes. In addition, DESI – like SIMS – requires minimal sample preparation, which could be problematic leading to analyte delocalization or chemical modification of endogenous compounds[1]. On the other hand, a limitation of DESI is the physical damage encountered by biological samples on a microscopic scale during

DESI imaging, when a conventional solvent system such as MeOH:H_2O is used. Depletion of tissue samples was necessary to obtain sustainable abundant signals and high quality images of biomolecules in tissues[44]. Nevertheless, recently developed solvent systems such as ACN:DMF and EtOH:DMF (1:1) have shown to provide abundant signal and high quality DESI images for lipids while preserving tissue morphology and protein content of biological tissues. These non-aqueous ‘‘morphologically friendly” solvent systems are non-destructive allowing analysis in sequence using immunohistochemistry and MALDI imaging to be performed on the same tissue section after DESI-MS imaging[45]. Recent DESI applications include the profiling of lipids for characterization of tumorigenesis[46], the analysis of colorectal adenocarcinoma tissue[47], and the study of endogenous and drug metabolites[48].

1.2.3 Matrix-Assisted Laser Desorption Ionization - MALDI

Biomolecular imaging using MALDI was first described in 1994 by Spengler et al.[49] and later in more details in 1997 by Caprioli et al.[4], nowadays it is the most widely used MSI method[38]. It is a soft ionization technique that is capable of producing intact higher molecular weight ions using a pulsed laser beam combined with energy absorbing matrix molecules.

An outline of the technique goes typically as follows (Figure 3); a matrix solution is applied to cover the sample surface, which is commonly a thin tissue section. The matrix, which is a low molecular weight organic compound possessing suitable chromophores to absorb the energy of UV laser beam, is usually applied in high excess relative to the concentration of surface analytes. On-tissue application of the matrix solution results in *in-situ* extraction of biomolecules from the sample surface. Subsequently, evaporation of the solvent causes crystallization of the matrix molecules and incorporation of analyte biomolecules into the formed crystals. As the laser beam irradiates the sample surface, the matrix crystals absorb the majority of the laser energy, leading to explosive desorption of the matrix crystals, incorporating the analyte into the gas phase without its degradation. The matrix facilitates the ionization of analyte molecules in the gas phase as well. For each location where the laser hits the sample surface, mass signals of the desorbed ions are acquired in a mass spectrum. A data set consisting of an ordered array of mass spectra is created, where each spectrum represents the local molecular composition at known x,y coordinates. The intensities of

the molecular masses (m/z values) of specific compounds in each spectrum can be extracted to produce images showing the localization of the molecules within the tissue[39].

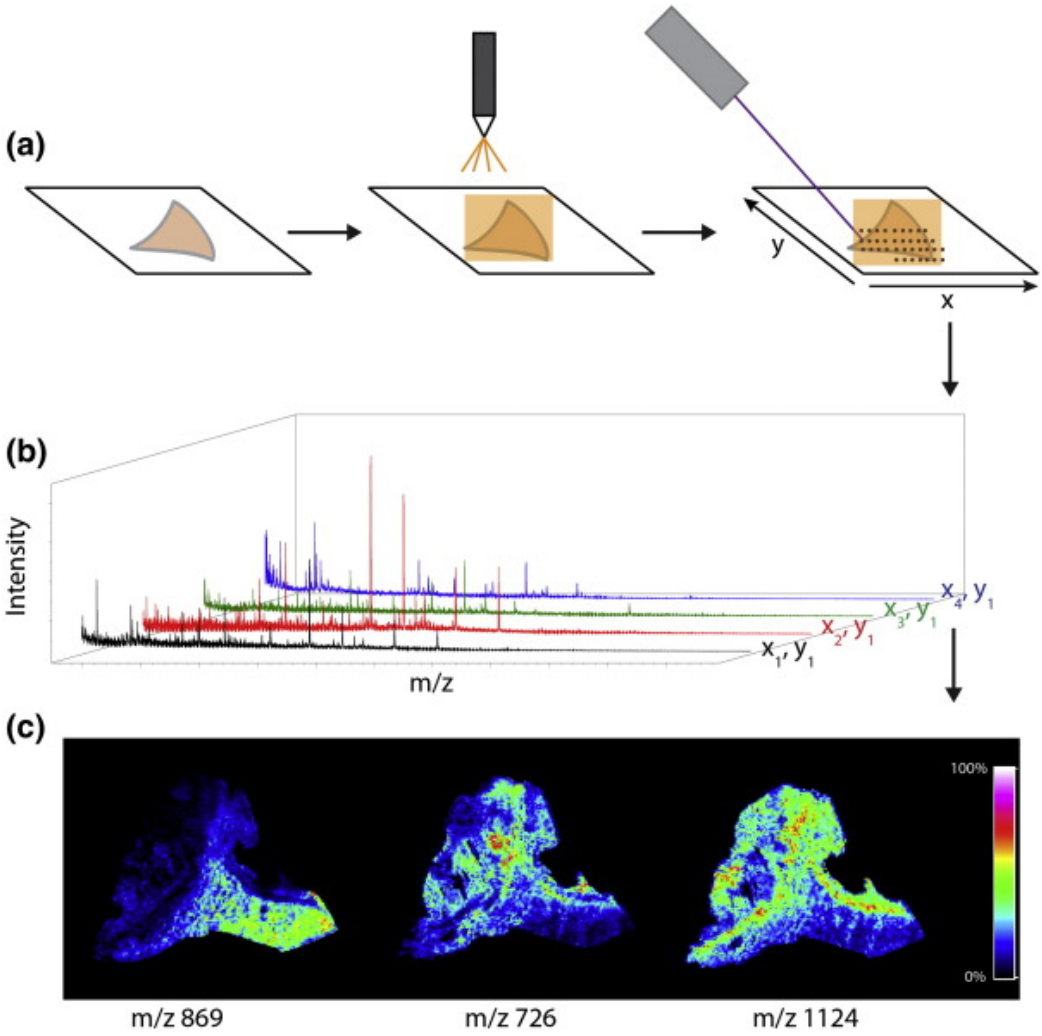

Figure 3. Overview of the MALDI IMS workflow on a section of a human kidney biopsy. (a) Fresh frozen tissue is cut and mounted on a glass slide. Matrix is applied by a robotic sprayer or is sublimated, and the section is irradiated by the laser in a raster array. (b) Mass spectra are acquired for each x,y coordinate. (c) Selected ions may be mapped on the tissue surface to create ion images. (Adapted from Gessel et al. [50])

This section overviews the MALDI MSI pipeline, including sample preparation, matrix selection and application, desorption and ionization processes, lasers, mass analyzers, and data processing. Finally, applications of MALDI for biomolecular imaging are discussed.

Sample preparation

Sample preparation pipeline encompasses all handling of the samples starting with collection until analysis. Developing sample preparation protocols aims mainly at maintaining the spatial integrity of biomolecules in the sample. Variation in sample preparation results in variation in ion generation, hence careful optimization is necessary to maintain sensitivity, accuracy and reproducibility of the analysis. Sample preparation includes collection (cutting, mounting, storage), processing (washing, digestion, derivatization), and finally matrix application. The work in this thesis exclusively uses tissue sections of animal origin. Hence, the most common procedures for sample preparation with respect to animal tissues are discussed.

Collection

Fresh frozen tissues are ideally suited for MALDI MSI studies[50]. It is important to minimize the time between harvesting the sample and its preservation to reduce sample degradation by endogenous enzymes. Commonly, a cryogen like liquid nitrogen allows snap freezing of the biological samples for stabilization. A snap-frozen tissue can be stored at temperatures below -70 °C for a minimum of one year without detrimental effects on the quality of MALDI MSI results[51]. Another possibility to preserve samples is fixation (e.g. formalin-fixed tissues), which is ubiquitously used for clinical studies and a huge amount of archived fixed samples already exists. However, it is not optimal for tissue preservation in MALDI imaging studies, because there is no control of molecules diffusion during fixation, in addition to the problematic mass spectrometric analysis of the cross-linked proteins[52]. Methods useful for the analysis of formalin-fixed samples have been described to leverage this vast source of information[53].

After biological samples are collected, they are cut through using a cryostat microtome into thin sections (3-20 μm) with the aim of obtaining a flat and even surface, for optimum imaging results[54]. It is required to optimize the cutting temperature and the tissue thickness individually for the different tissue types[50]. Sometimes it is required to embed fragile or small tissues in an embedding medium to support their sectioning. Classically, optimal cutting temperature compound (OCT) is the medium of choice for histopathological studies. However, it is not suitable for MALDI MSI since it ionizes

and causes up to 50% signal suppression due its high abundance[55]. Alternative embedding media like gelatin and carboxymethylcellulose (CMC) showed to interfere less with the analysis. Subsequently, tissues are mounted on the sample holder, which could be a glass slide, or a conductive surface in case of MALDI-TOF instruments (e.g. ITO glass slides), and stored at temperatures below -70 °C until analysis.

Processing

Before application of the matrix, optional processing of the samples can include some pretreatment steps. The processing protocol is tailored and validated according to the target analytes and could significantly improve the results of the analysis. This includes drying, washing, on-tissue digestion, and derivatization.

After the removal of tissue sections from the freezer for analysis, they are dried to lessen instability by several methods, e.g. vacuum desiccation[56] or air under a stream of nitrogen[57]. Tissue washing should be carefully optimized because it directly affects composition and localization of the analytes within the sample. It is usually considered to remove ionization-suppressing small molecules and lipids during the analysis of proteins and peptides[58]. In some cases, on-tissue enzymatic digestion is needed to overcome the low sensitivity of the imaging analysis of intact proteins. This is particularly useful for formalin-fixed paraffin-embedded (FFPE) tissues, to liberate peptides from the cross-linked proteins[59]. Enzyme are either spray-coated in the same manner as the matrix, or applied using an automatic spotting instrument[60]. Also, different strategies for on-tissue chemical derivatization were introduced to imaging studies, to improve detection of low molecular weight drugs within tissues, where poor ionization efficiency, isobaric endogenous compounds, or ion suppression complicate the analysis[61]. Derivatization is relatively a new approach and of limited application due to variations in reactions yields and side reactions.

Matrix selection and application

Matrix application plays an important role in successful MALDI MSI analysis. Lateral resolution and detectability of the analytes are strongly decided by the choice of matrix and its method of application. Generally, the matrix coat applied to the sample surface should be very homogenous providing crystal structure size that matches the diameter of the laser beam to guarantee high quality ion images. The basic strategy is to apply

the matrix in a quickly evaporating solvent to extract the analyte, ensure proper crystallization, and minimize analyte diffusion[54].

Selection of matrix and solvent

The matrix solution commonly includes three components, the matrix compound, the solvent, and triflouroacetic acid, which is added in many cases to promote ionization. The MALDI matrix is typically a low molecular weight organic acid with strong absorbance at the wavelength of the laser used. Many matrices proved useful for different compound classes[39, 54], however, the three most commonly used matrices for MALDI MSI are 2,5-dihydroxybenzoic acid (DHB), α-cyano-4-hydroxycinnamic acid (α-CHCA), and 3,5-dimethoxy-4-hydroxycinnamic acid (SA, sinapic acid)[59], as shown in Table 1. While SA is most suitable for the analysis of proteins, DHB and α-CHCA are more suited for peptides, lipids and lower molecular weight analytes. Ideally, several matrices with different solvent composition should be experimented in both positive and negative ion modes to specify which matrix is the best for a certain analyte. The choice of solvent can cause significant differences in the properties of crystallization of matrices on the surface tissue sections[62]. Different combinations of water and organic solvents like, methanol, acetonitrile, acetone, and isopropanol are commonly used. A 50% organic solvent solution is a proper starting point for testing and optimization[55].

Other nontraditional matrices include ionic liquid matrices[63] (e.g. α-CHCA acid with 2-amino-4-methyl-5-nitropyridine), inorganic metal matrices (e.g. gold nanoparticle[64], colloidal graphite[65]), in addition to matrix-free approaches[66]. These methods have their strengths and weaknesses, however, they are less common due to limitations regarding sensitivity and applicability to a wide range of target compounds[59].

Table 1. Chemical name, structures, and application of common matrices used in MSI analysis[67].

Compound	Structure	Application
DHB (2,5-Dihydroxybenzoic acid)	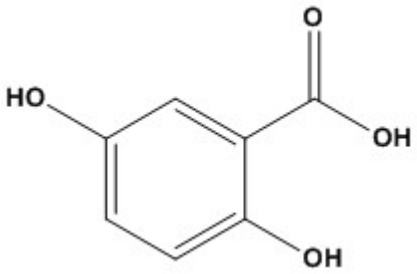	Peptides Lipids Oligonucleotides Carbohydrates
α-CHCA (α-Cyano-4-hydroxycinnamic acid)	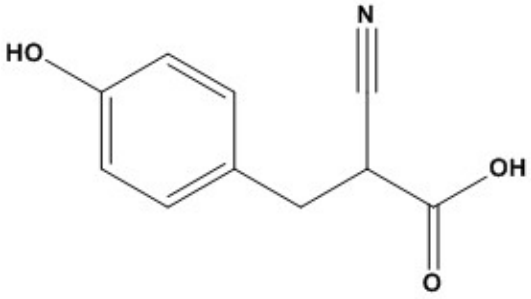	Peptides Pharmaceuticals Lipids Oligonucleotides
Sinapic acid, SA (3,5-Dimethoxy-4-hydroxycinnamic acid)	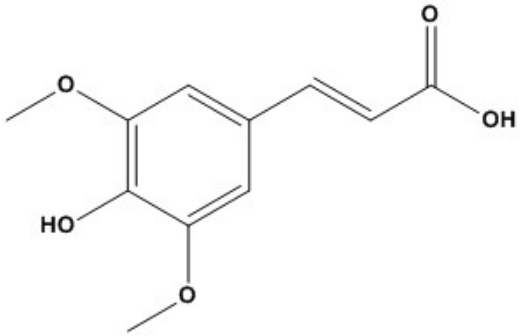	Proteins Peptides

Methods of matrix application

Matrix coating can be either discrete, which is more common to profiling applications, or continuous. Discrete matrix application has the advantage of limited analyte diffusion and is usually performed using automated piezoelectric spotters dispensing picoliter volumes of the matrix solution[54]. Continuous matrix application is the mode used for MALDI imaging.

It can be performed by a number of methods like, spray-coating, electrospray deposition, or solvent-free dry matrix application (e.g. sublimation, sieving)[68].

Manual spray-coating using a pneumatic airbrush sprayer is cost-effective, nevertheless, it is difficult to standardize across multiple samples and laboratories because it is subjective and depends on the skills of the analyst. Automatic spraying of the matrix is the method of choice for the majority of MALDI MSI community because it overcomes the lack of reproducibility associated with manual spraying. A number of commercially available robotic sprayers having almost the same working principle is available on the market[59]. The matrix solution is sprayed as fine aerosol and allowed to deposit on the tissue surface. The coat is allowed to dry and several iterations are normally needed to obtain enough amount of matrix for the analysis.

Other less common methods for matrix application in MALDI MSI include sublimation, which produces uniform very small matrix crystals making it suitable for high resolution imaging[59]. Also, the use of commercial desktop inkjet printers provided a low-cost method utilizing the same principle of automated chemical spotters[69]. Automatic spotters cover the samples surface with a spaced array of small matrix droplets (picoliter volumes) providing both automated uniform matrix coating and sufficient permeation into the tissue[68].

Lasers

MALDI MSI studies reported the use of ultraviolet (UV) and infrared (IR) lasers. UV-MALDI is the most widely used mode. It commonly utilizes nitrogen (N_2) gas lasers because they are simple, small-sized, and relatively low in cost. Their emission wavelength ($\lambda = 337$ nm) is close to the absorption maximum of many commonly used matrices such as DHB, α-CHCA, and SA. Disadvantages of N_2 lasers include limited pulse repetition frequency (< 100 Hz). Also, their relatively short lifetime (total number of emissions $\leq 10^8$ which normally correlates to ≤ 2 years) limits their application in high-throughput analysis[70]. For such type of applications, frequency-tripled Nd:YAG solid state lasers ($\lambda = 355$ nm) having longer time spans are used. The Nd:YAG lasers also provide more sensitive MALDI MSI analysis due to achievable repetition rates of up to 1000 Hz[71].

IR-MALDI is relatively less common. It utilizes liquid matrices providing better spectral reproducibility in comparison to UV-MALDI, which mostly uses solid state matrices with relatively high degree of heterogeneity depending on analyte-matrix co-

crystallization[72]. Examples for IR lasers employed in MALDI MSI studies include pulsed erbium solid-state lasers (Er:YAG, λ = 2.94 μm and Er:YSGG, λ = 2.79 μm).

Desorption and ionization

The desorption and ionization processes in MALDI are extremely complex involving a large number of intertwined physical and chemical events and have been the focus of many research groups[73, 74]. A comprehensive discussion of these events is beyond the scope of the thesis. Hence, only a brief overview follows in the next paragraphs.

Desorption

Desorption of the matrix and analyte occurs when a sufficient energy density is achieved through short pulse durations (ns) of the laser. Energy deposition is affected by a number of parameters including sample properties, matrix absorption, sample surface characteristics, and most importantly, the laser fluence (J cm^{-2}) [74]. Generally, a rapid phase transition of the bulk matrix-analyte material from solid to gas occurs leading to disintegration of the top layers. The disintegration event may be characterized as ‘‘desorption’’ or ‘‘ablation,’’ depending on the laser fluence. In the desorption regime, the solid to gas transition is smooth at the top surface of the sample, and the emitted material contains little or no condensed particles, droplets or clusters. At higher ablative fluences, the sample is sufficiently overheated that subsurface nucleation occurs, leading to ‘‘phase explosion’’ which is turbulent and frothy. This ejects condensed material consisting of particles and clusters. According to literature, MALDI is often performed in the ablation regime[68, 73, 75, 76].

Ionization

Much research has focused on the specific mechanisms of the MALDI ionization processes and numerous theories and models have been proposed. A consensus that supports the idea of several processes occurring and not just one single event, has been reached.

These competing processes are evidenced by the presence of a variety of ionized species in the mass spectrum that may be protonated, deprotonated, cationized, or radicals[77-82]. It is generally accepted that ion formation follows a two-step model. Primary ionization is the first step, it refers to ions produced from the neutral molecules of the

sample surface and it mostly involves a contribution of the matrix. Ion-molecule reactions in the desorption/ablation plume follow, giving rise to secondary ions which reach the detector (secondary ionization)[83].

Whereas, various models for generation of primary ions are still somewhat divergent, mechanisms for secondary ionization have been widely accepted, as they are believed to follow basic condensed phase 'plume' kinetic and thermodynamic rules. Several mechanisms and models were proposed to explain the primary ionization, among which "the cluster ionization mechanism" also known as "the lucky survivor model"[77-79], and "the photoexcitation/ pooling mechanism" known as "the coupled physical and chemical dynamics model" (CPCD)[80-82] are the most widely accepted. The key points for both models are briefly discussed.

Primary ionizaion

The lucky survivor model

Also known as "the cluster ionization mechanism", this model proposes that the analyte ions are largely preformed in the solid matrix and considers matrix mainly as an ablation vehicle and does not contribute preformed ions. The evidence for the preformed ions in the solid matrix was observed during the preparation of MALDI samples of pH sensor dyes from solutions of different pH[84]. The solid samples retained the color of the original solution, indicating that the dye molecules had the same ionized state as in solution.

The disintegration of the solid matrix upon laser irradiation leads to the formation aggregates having an excess of positive or negative charge. Once in the expanding plume, the charged clusters dissociate and undergo extensive but incomplete neutralization in the plume by counterions leaving some ions at the end. The neutralization happens by losing neutral matrix molecules to release the analyte ions or by ejection of the ions.

For this reason, the model is called "the lucky survivors"[78], indicating that they are the ones which survived the neutralization process, and justifying the presence of the singly charged species.

The Coupled Physical and Chemical Dynamics model (CPCD)

This model is also known as ‘’the photoexcitation/ pooling mechanism”, and on the contrary to the cluster model, almost all primary ions are derived from the matrix. It is based on the initial photoexcitation of the matrix with consequent migration of the excitation energy within the matrix crystals. This is followed by the concentration of this energy by two sequential pooling events resulting eventually in ionization[85]. The combination of migration and pooling events is necessary because direct photoionization by two- or multi-photon absorption of matrix or matrix-analyte complexes, is less likely. This is because the ionization potentials (IP) of nearly all MALDI matrices lie above the 2-photon energy of the typical UV-MALDI lasers, even in condensed clusters where the IP is expected to drop[81]. However, this amount of energy can be concentrated on one molecule by two sequential pooling events. The model assumes that the excitation energy (known as excitons[86]) is mobile in the crystals with stacked aromatic π-electron systems of matrices. Pooling happens through redistribution of excitation energy of two neighboring molecules resulting eventually in de-excitation of one of the two molecules to the ground state and ionization of the other one. The excited states interact either in S1-S1 or S1-Sn pooling, the latter being responsible for ionization[83].

Secondary ionization

Secondary ionization starts as soon as primary ions exist, hence it could occur concurrently to primary ionization when the material is still dense allowing extensive ion-molecule reactions. It includes charge transfer between matrix and analyte and between analytes, and it occurs in the expanding plume and takes much longer in comparison to primary ionization. Changes in the density allow the collisions and interactions of the primary ions with the neutral molecules to give new ions[67, 81].

The charge transfer is assumed to be reversible and could occur through the following main reactions:

- Proton transfer: $mH^+ + A \leftrightarrow m + AH^+$, and $(m\text{-}H)^- + A \rightarrow m + (A\text{-}H)^-$
- Electron transfer: $m^+ + A \leftrightarrow m + A^+$, and $m^- + A \rightarrow m + A^-$
- Cation transfer: e.g. $mNa^+ + A \leftrightarrow m + ANa^+$

Where, m = matrix, A = analyte.

Mass analysis

After desorption and ionization, the analytes enter the mass spectrometer where they are separated based on their mass-to-charge ratio (m/z). MALDI ion source has been coupled to a variety of mass spectrometers for imaging applications including, time-of-flight (TOF), quadrupole ion trap, Fourier transform-Orbitrap, and Fourier transform-ion cyclotron resonance (FT-ICR) mass spectrometers.

The versatility of the of the MALDI ion source for MSI applications allowed many companies and research groups to focus on instrument and software developments, which resulted in the availability of several MALDI mass spectrometers with variable MSI capabilities on the market. The specific MSI application determines the choice of the instrument, for example, the requirements necessary for protein imaging differ largely when compared to small molecules. The important qualities that determine the choice of a MALDI MSI instrument include spatial resolution, mass range, mass resolving power, mass accuracy, sensitivity, tandem MS capabilities, throughput, and data storage[50, 59].

Classically, MALDI ion source has been coupled to TOF mass analyzers, this was largely due to the nature of the ion source, producing pulsed ion packets, which were suitably measured and analyzed using a TOF analyzer. In TOF mass analyzers, ions are accelerated to a very narrow range of kinetic energies, then separated according to their m/z in a flight tube. Although MALDI-TOF instruments offer excellent throughput, they suffer limited mass resolving power and mass accuracy essential for direct mass identification of analytes in biomolecular imaging studies. MALDI-FT-ICR and MALDI-FT-Orbitrap are on the other hand high performance alternatives, which offer high mass resolving power and high mass accuracy.

These methods have shown to resolve and identify ions at a single nominal mass that are commonly present in MALDI imaging mass spectra[87].

This work includes imaging measurements that has been mainly done using a hybrid linear quadrupole ion trap-Orbitrap instrument; MALDI LTQ Orbitrap XL^{TM} (Thermo Scientific). The instrument can operate as a standalone version of either the linear quadrupole ion trap or the orbitrap, or as a hybrid device of both. The working principle of the linear ion trap and the orbitrap follows in the next paragraphs.

Linear quadrupole ion trap

The geometry of the linear ion trap could be seen in Figure 4. It consists of four electrode rods cut into three axial segments. The central section where ions are stored is longer in comparison to front and back sections, which are of equal but shorter length. A combination of radiofrequency (RF) and direct current (DC) voltages are applied to opposite pairs of rods to trap the ions. The linear ion trap is versatile and can operate to store, isolate, dissociate the ions and then send them to the Orbitrap for further analysis (axial ion ejection). Alternatively, it can also operate as an independent mass analyzer sending the ions directly to the detector (radial ion ejection to the electron multiplier detector). It is a low resolution device that when combined to other mass analyzers offers improved space-charge capacity, increased sensitivity due to higher ion storage capacity, and more efficient ion injection[67].

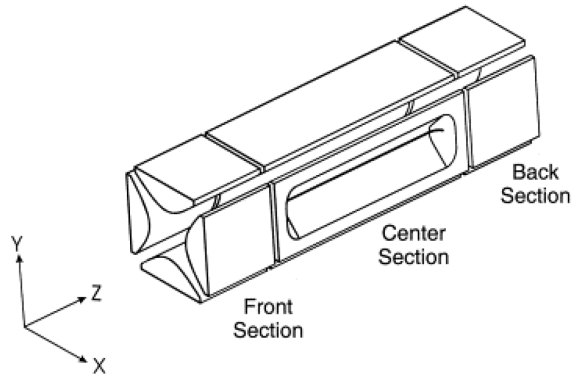

Figure 4. Basic design of the two-dimensional linear ion trap (adapted from Schwartz et al.[88])

Orbitrap

The Orbitrap consists of a central spindle-shaped electrode surrounded by a pair of bell-shaped outer electrodes, together they form a barrel-like shape (Figure 5). It employs an electric field to trap the ions orbitally. The orbital motion of the ion is related to the ion kinetic energy and is used for radial trapping and not for mass analysis. In the axial direction, ions oscillate harmonically from one end of the barrel assembly to the other while they continue to orbit around the central spindle electrode. The frequency of the back-and-forth axial oscillations determines the m/z ratio[89]. Two split halves of the outer electrode of the Orbitrap detect the image current produced by the oscillating ions.

By Fast Fourier Transformation (FFT) of the image current, the instrument obtains the frequencies of these axial oscillations and therefore the mass-to-charge ratios of the ions. Orbitrap is a high performance device that allows direct and accurate identification of biomolecules due to high mass resolving power [89].

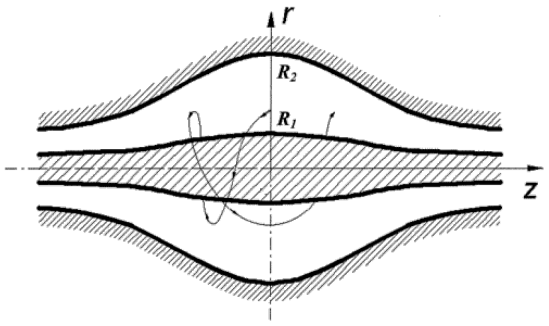

Figure 5. Orbitrap mass spectrometer. Curved arrows show the stable ion trajectories. R1 and R2 represent the electrodes radii (adapted from Makarov et al.[90])

MSI software

One of the principal goals of data analysis in MSI experiments is to determine trends in the spatial distributions of biomolecules, which can be related back to the underlying biology. MALDI MSI data sets can be many tens to hundreds of gigabytes depending on the specimen size, image resolution, and spectral resolution. This developed the need for software programs to process the highly complex MSI datasets. Generally, MSI software tools can be classified into two main categories which control either data acquisition or processing (visualization and analysis in order to generate ion images).

Data acquisition software

This type of software is designed to register the target location or region of interest defined by the user. It defines the target location by allowing the user to draw a shape around the area of interest using an optical image of the sample, and setting the spatial resolution within this area. Afterwards, automated acquisition is initiated to collect mass spectra at each position in the raster pattern. Image acquisition software could be separate or integrated in the standard instrument control software[59].

Image analysis software

After image acquisition, proper data processing and analysis of datasets is crucial for accurate interpretation of the results. The MSI dataset has a specific data format that

depends on the measuring instrument. Most mass spectrometers have a proprietary data format, which can be exported to the image processing software provided by the vendor such as, FlexImaging (Bruker), Tissue-View (ABSciex), and ImageQuest (Thermo).

On the other hand, a number of open source software for visualization and processing of MSI data has been described. For example, MSiReader, an open source program to view and perform data analysis of MSI data has been described[91]. It has been rapidly taken up by users and provides a Matlab interface allowing it to be adapted to individual needs. Also, OpenMSI, a Web-based open source software, provides a high-throughput solution for image data processing. Large imaging data sets can be stored and processed on a central high performance server, while users visualize the resulting images on local computers[92].

In this respect, common data formats have proven to be useful allowing data exchange between different instrumental platforms and between different image evaluation and processing software tools. Two of the most common open-source formats for MSI data are Analyze 7.5 and imzML[59]. Data analysis of MSI measurements in this work has mainly used the common data format imzML.

imzML. The initiative for developing imzML was to ensure flexible and fast handling of the MSI data, provide complete description of the MSI experiment, and minimize the data file size. It was developed to follow the standards proposed by the Human Proteome Organization- Proteomics Standards Initiative for storing mass spectrometry data. It is consistent with the existing mzML format and consists of two separate files. The binary file (*.ibd) stores spectral data, and the (*.imzML) file stores all associated metadata. Both file types are required to fully describe the dataset[93, 94].

The imzML format has been adopted by a growing number of instrument vendors and continues to be used by developers of open-source MSI image processing software.

MSI data processing

Spectral preprocessing

The data analysis process can be generally divided into two separate processes, data preprocessing, and analysis. MALDI MSI data show experimental variance within the raw dataset. For this reason, preprocessing of the data is useful to reduce such variance before the analysis of the data in order to obtain confident conclusions and improve

subsequent processing. Spectral preprocessing could involve baseline correction (denoising or removal of background), realignment, normalization of intensity, and peak picking.

Baseline correction

The intensity value recorded for each element in the profile spectrum is commonly associated with a certain amount of noise or background. The amount of noise is instrument-dependent and arises from experimental fluctuations. Possible sources may arise from transient detector gain variations or statistical fluctuations in ion motions. A number of algorithms have been reported for estimating background and many commercial data analysis software packages include baseline correction modules[95]. It is worth to mention that baseline artifact is much reduced from mass analyzers that include an orthogonal mass separation stage, such as hybrid instruments[96].

Normalization

In general, it is important to normalize ion intensities to minimize differences in peak intensity between spectra, i.e. scaling each spectrum to some factor for better intercomparison of intensities between different spectra[97].

These differences in intensity values could arise from variation in instrument performance, as well as differences in sample preparation, inherent sample variability, and experimental error. Normalization has been routinely applied in many areas of mass spectrometry, especially for quantitative analysis where ion intensity is normalized against the intensity of an internal standard that has similar ionization characteristics as the analytes of interest.

For MALDI MSI, several normalization methods have been described to address the variability in signal intensity[69, 95, 98-105]. This includes the often used normalization to Total Ion Current (TIC). It is recommended that visual examination of exemplary m/z-images after TIC normalization should be considered[97], since for some MSI software, TIC normalization makes the assumption that the same number of ions will be produced from each spatial location[100, 106], which could introduce artifacts and limits the reliability of the method[95, 98]. Also, normalization to matrix related peaks[99] was used for correction of uneven matrix thickness and crystallization. However, this method assumes that endogenous biomolecules respond

evenly to changing matrix conditions, limiting the success of this approach as well[3]. Other methods implement normalization algorithms based on noise levels, and median signal intensity of the spectrum[98, 100]. On the other hand, the most promising approaches for MSI signal normalization seem to be those applying internal standards, enabling pixel-by-pixel correction of raw intensities[42].

Calibration and realignment

Systematic shifts that affect the whole spectrum (e.g. due to instrument fluctuations) can be compensated for with recalibration or online lock mass calibration using known ions within each spectra (e.g. matrix peaks)[107]. However, variability in the centroid m/z detected for an individual peak (mass shifts within the mass accuracy range) throughout the course of a number of replicate measurements (or between the different spectra) can cause problems for quantitative comparisons, even with a properly calibrated instrument.

Moreover, irregularities within the flatness or thickness of tissue sections boost this mass measurement variability. In such case, calibrating each spectrum to known peaks that are common to the dataset and can be recognized within the spectra (i.e. internal calibrants or landmarks), can effectively realign the spectra to ensure that comparison considers the intensity of the same ions across a number of samples. It is also important that these common peaks span the entire mass range of interest to prevent extrapolation outside of the chosen alignment points[95].

Peak picking

Peak picking is the selection of m/z values which correspond to high and relevant peaks with the aim to reduce the number of m/z values by neglecting those values corresponding to noise signals or to non-specific baseline signals[97]. Various peak picking methods for MALDI mass spectra are implemented in mass spectrometry imaging software packages. Nevertheless, this process has showed to be difficult to perform in a blind automated manner due to the presence of unresolved peaks. Hence, it is recommended to carefully visualize the results in order to validate the labeled peaks manually[59].

Data analysis

A list of m/z values and their corresponding intensity or peak areas extracted from each spectrum in the data set, is usually the output of the preprocessing steps previously described. Depending on the biological task under investigation, this data can be subject to a number of data-mining methods with the aim of information extraction.

A simple approach is to use the resulting list of m/z values to identify specific molecules of interest in the dataset. Then, the localization of the specific molecules (drugs, metabolites, etc.) is compared in disease-state tissue with physiological one to search for disease biomarkers. In this approach, it is beneficial to examine the resulting ion images and the histological staining images of both tissues types to link distinct molecular distributions to histological features[6].

Other data mining approaches include a set of statistical methods that allow spectral classification of the data and results in a collection of ion images and/or spectra, which show important features within the dataset.

A well-known example is principal component analysis (PCA). It is an unsupervised method that groups together peaks whose intensities are correlated in certain areas of the tissue. The output of the analysis is a set of principle components that are rank-ordered according to the amount of variance that they describe in the data.

Software developers have developed MSI software packages to facilitate the analysis of MSI data. Commercial software packages, such as Multimaging (Imabiotech, France) or SCiLS (Bruker Daltonics, Germany) can handle large-sized, multi-sample data sets and include many statistical tools for biomarker discovery[108]. Open-source software is available as well, such as MSiReader[91] or Biomap[109], but is less focused on the simultaneous analysis of several samples. Also, studies reported different in-house developed data mining approaches for MALDI MSI datasets[110, 111].

Biological applications of MALDI MSI

MALDI is currently a dominant technique in biomolecular MSI, owing to its versatility and its widespread commercial availability[7]. Several biomolecule classes including proteins, peptides, lipids, drugs, and carbohydrates have been investigated in diverse biological tissues[39].

In the following, a number of examples with a focus on MSI of lipids, will shed light on some areas where MALDI MSI studies of different molecule classes contributed to the understanding of biological processes.

MALDI profiling studies of proteins were reported in various cancer tissues showing protein content specific to each tumor type such as those of the brain[112] or lung[113]. Also, proteomic changes detected by MALDI profiling studies in mouse tumors, proved useful to correlate the variation in protein profiles to the disease progression, which is important for evaluation of treatment efficiency and prognosis. For neurodegenerative diseases, brain distribution of proteins led to the identification of a biomarker protein of Parkinson's disease in a mouse model[114]. Also, molecular physiology of the eye was the subject of MALDI MSI studies, which reported the modifications and distributions of crystalline proteins in the lens and correlated this to clinical conditions like formation of cataracts[115].

Peptides were also attractive targets for MALDI MSI investigations because their peaks are generally more intense and resolved than proteins[89]. The specific distribution of amyloid peptides in brain tissue of a mouse model of Alzheimer's disease was investigated[116]. Also, investigations of various neuropeptides were the focus of a number of MALDI MSI studies[117-119].

Application of MALDI to the imaging of pharmaceutical compounds has been of great interest to study the distribution of drugs in tissue specimens. Examples include the imaging of MRI contrast agents in fresh and fixed tissues. The distribution of the contrast agent, a Gd-containing compound, was further validated with MRI and inductively coupled plasma atomic emission spectroscopy[120]. Also, the controlled release of drugs and their distribution into the adjacent tissue by implanted medical devices (drug eluting coronary stents) was studied by MALDI MSI[121]. The distribution of tiotropium, a bronchodilator for the management of chronic obstructive pulmonary disease, that is administered via inhaled delivery, was imaged in lung tissue to better understand the distribution in lung tissue of rats[102].

MALDI MSI of lipids

Many applications of MALDI MSI focus on lipid analysis because of their diverse roles as structural components of cell membranes, their function in the surfactant cycle, and

their involvement as second messengers in signaling cascades of tissues and cells[68]. A few examples are presented in this section.

Alterations in lipid distribution due to changes of physiological or pathological conditions could be detected in rodent brains by MALDI MS. For example, age-related changes in the distribution and amount of phosphatidylcholine (PC) species in rat brain have been investigated[122]. Also, a study of rat brain demonstrated the localization changes of brain lipids after traumatic brain injury[123]. In a different study, investigation of PC and sphingomyelin (SM) species could distinguish brain compartments[124]. Furthermore, cholesterol localization showed lower abundance in the cell nuclei of the granular layer as compared to white matter structures in a study of rodent cerebellum[125]. Profiling of phospholipids and lysophospholipids in rat brain of experimentally infarcted rats, showed a conversion of phosphatidylcholine to lysophosphatidylcholine, suggesting a role of lysophosphatidylcholine in the progression of brain injury during ischemic stroke[126].

Other lipid studies of MALDI MSI included other tissues of mice as well. Visualization and identification of phospholipids in the mouse retina by MALDI MSI showed a three-zone distribution of PC species[127]. A mouse model of glycosphingolipid storage disease was used to study the changes of sulfatide lipids in kidney tissue[128]. Visualization of different lipids species (SM, lyso-PC, PC) in mouse tongue was also reported[129].

In addition, tissue sections from different human organs were studied by MALDI MSI for numerous purposes. A few examples include a study of the distribution of lipids in human brain cortex, which allowed to distinguish grey and white matter effectively[130]. Also, the role and distribution of lipids in tumor tissue has gained growing attention, although, applications of MALDI MSI to cancer research has mostly focused on proteins and peptides. Lipid changes observed in myxoid liposarcomas could be related to pathways known to be affected during tumor progression which helped identify tumor type and grade[131]. A study of ovarian cancers showed differential distribution and higher levels of sulfatides[132]. A different study of human lenses reported on the age-related profiles of lipids, showing an accumulation of dihydroxysphingomyelin, DHSM (d18:0/16:0) and dihydroxyceramide, DHCer (d18:0/16:0) in the barrier and nucleus regions, respectively[133].

3D MALDI

Constructing a 3D view of the distribution of biomolecules in the tissue has gained growing interest in MSI techniques. MALDI MSI is basically 2D imaging method, however, obtaining a 3D view is possible by analyzing serial sections of the sample and merging the individual 2D images into one 3D representation using a special software, such as, Image J[3, 108]. Care should be taken that the distance between the analyzed serial sections is appropriate for the tissue structure to be reconstructed, and also to process the sections under identical conditions[6]. The details of serial sectioning approach to create 3D MALDI images of different biomolecules was described for a variety of different samples[134-136]. This includes 3D imaging of protein and peptide distribution in rat midbrain[137], and a reconstructed 3D view of mouse brain using myelin basic protein[138].

A recent study presented a different approach using an autofocusing AP MALDI MSI system for studying 3D sample surfaces with topographic aspect. The developed system keeps the MALDI laser focus, fluence and ablation spot size constant over sample height variations by adjusting the sample stage position according to the sample height profile for each measurement spot[139].

1.2.4 Laser Ablation Inductively Coupled Plasma - LA-ICP

LA-ICP-MS allows the distribution analysis of metals on the surfaces of tissue sections without pretreatment, such as matrix application. A focused laser beam is used to ablate sample material which is transported by a carrier gas (Ar or He) into the ICP source. In the ICP operated at 7000−8000 K, the sample material is atomized and ionized, and its elemental components are analyzed[140, 141]. It is the method of choice for the imaging of elements in thin cross sections of biological tissues and is currently considered as the most sensitive technique for elemental bioimaging[142]. Spatial resolution range of 4 to 100 μm and limits of detection in the range of 0.001 – 1 μg g^{-1}, could be achieved. The merits of LA-ICP-MS are high throughput, high sensitivity, and high accuracy. In addition, minor matrix effects allow quantification of the analytical data[140].

The numerous applications of LA-ICP-MS as a bioimaging tool include the investigation of Parkinson´s disease, stroke and aging in brain tissues, metal uptake,

cancer studies, etc. In addition, LA-ICP-MSI was used to scan 1D and 2D gels and blotting membranes to analyze metals in protein bands or protein spots[140-142].

1.3 Multimodal imaging

Combining information obtained from different MSI methods and other imaging techniques allows to explore additional information, such as structural information classically obtained from histological staining or Magnetic Resonance Imaging (MRI) and molecular information from MSI. Figure 6 illustrates a number of possibilities to combine data from various imaging techniques to MSI results. Such combination approaches are very powerful and increase the conclusiveness, validity, and informative value of MSI data[38].

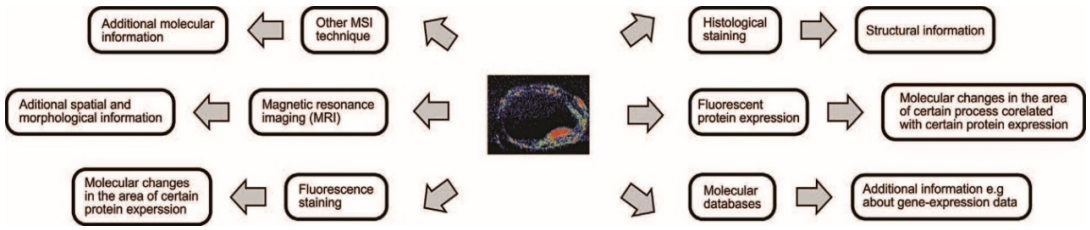

Figure 6. Combining of MSI data and different imaging techniques (adapted from Bodzon-Kulakowska et al. [6]).

A classical approach of combining data from MS-based approaches to other analytical methods is to correlate the molecular data to structural information obtained from histological staining like H&E. This requires coregistration of the resulting ion images and microscopic images of H&E staining. For this, a tissue section consequent to that measured by MSI could be used for staining. For unambiguous correlation between the data, the histological staining could be performed on the same tissue section measured by MSI. In case of MALDI imaging, this requires matrix removal by rinsing the tissue section briefly with ethanol, or ethanol and acetone[137].

Combining results from different MSI approaches is also considered as beneficial since they differ in their analytical capabilities. An example was presented in a study where the same tissue section was first analyzed by DESI for lipid profile using a ‘‘morphologically friendly’’ solvent system which does not destroy the sample (e.g. a combination of DMF with different solvents). MALDI analysis followed to obtain

information about the peptide constituents. Finally, the tissue could be stained with H&E for structural features[45].

Another example presented a combination of MALDI and SIMS imaging to study the distribution of electrolytes, lipids and peptides in a mouse model of rheumatoid arthritis. The localization of different lipids and tryptic peptides was revealed by MALDI, whereas SIMS measurements indicated the localization of potassium, calcium, cholesterol and several other lipids in various areas of the knee joint[143]. Moreover, combination of the quantitative elemental mapping by LA-ICP-MS and the molecular imaging of lipids by MALDI allowed correlate different sets of analytes from the same sample and develop comprehensive data analysis[140].

In a different study, an interesting approach developed a coregistration technique using fiducial markers (cresyl violet, Ponceau S, and bromophenol blue), which possess a combination of optical and molecular properties. This allowed accurate coregistration of fluorescent protein expression images with MSI images and reconstruction of 3D images of molecules distribution from a breast tumor model[134].

Another approach of multimodal imaging involved combining MS-based imaging methods to MRI. MRI enables to view the 3D anatomic structure of an organ of interest with significant resolution. Combining molecular results from MSI with detailed anatomical information from MRI was reported in a number of studies. Combining MRI and MALDI data showed altered abundance of different proteins in an imaging study of the inflammatory response to *S. aureus* infection in mice[135]. An important application of merging results from MRI and MS-based imaging modalities was reported for neurosurgery, where accurate removal of tumor tissue without affecting healthy tissue is necessary. The MRI image, recorded before the surgery in combination with a special cranial navigation tool (www.brainlab.com) and a special stereotactic neuronavigation pointer were used to precisely indicate the place from which the tissue is collected. This was followed by DESI analysis of obtained tissue sections, which enabled the classification of tumor subtype, grade, and cancerous cell concentration[144].

1.4 Lipids and lipidomics

1.4.1 Lipids

Lipids have essential roles in living cells including being main constituents of cellular membranes (membrane lipids), acting as precursors for lipid second messengers during signal transduction (bioactive lipids), facilitating transmembrane protein functions, in addition to providing fuel supplements for many biological processes (energy lipids). Also, more evidence nowadays shows that lipids are associated with many human diseases (e.g. diabetes, obesity, atheroscelerosis, stroke, cancer, psychiatric disorders, neurodegenerative diseases, and infectious diseases)[145]. Therefore, the research on lipids has gained a lot of attention and became an emerging field of basic and translational research.

The majority of lipid molecules could be defined as amphiphilic molecules composed of a hydrophobic and a hydrophilic components. They originate entirely or in part by carbanion-based condensations of ketoacyl thioesters and/or by carbocation-based condensations of isoprene units. Fatty acyls, glycerolipids, glycerophospholipids, and sphingolipids are derived by carbanion-based condensations, while sterols and prenol lipids originate from carbocation-based condensations[146, 147].

Chemists have classified lipids in a number of different ways. A simple classification distinguishes lipids simply into polar and nonpolar based on the overall hydrophobicity of the lipids. Nonpolar lipids are soluble in nonpolar solvents such as hexane, ethers and esters and include fatty acids and their derivatives (long chain alcohols and waxes), glycerol-derived lipids (mono-, di- and tri-acylglycerols), and steroids. Polar lipids are soluble in relatively polar solvents such as alcohols and include lipids containing polar head group such as glycerophospholipids. Biochemists classified lipids according to their function into membrane lipids, bioactive lipids, and energy lipids as mentioned earlier.

The widely accepted classification of the LIPID MAPS consortium divides lipids into eight main categories: fatty acyls, glycerolipids, glycerophospholipids, sphingolipids, saccharolipids, and polyketides (derived from condensation of ketoacyl subunits); sterol lipids and prenol lipids (derived from condensation of isoprene subunits)[147].

The work in this dissertation focuses on the lipid category known as glycerophospholipids (GPLs).

Glycerophospholipids (GPLs)

GLPs are principal components of cellular membranes. They are involved in numerous physiological processes, including membrane trafficking and cell signaling. Polyunsaturated fatty acids (PUFAs) are hydrolyzed from membrane GPLs and are further metabolized into numerous biologically active molecule[145].

The backbone of GPLs is a glycerol molecule substituted at the sn-3 carbon by a phosphate functional group, known as the polar head group, which defines the subgroup or class of the lipid (Figure 7). The main head group classes are phosphatidylcholine, phosphatidylethanolamines, phosphatidylserines, phosphatidylinositols, phosphatidylglycerol, and phosphatidic acid. The glycerol backbone is esterified with long-chain fatty acids (FAs), at the sn-1 and sn-2 positions[145, 148].

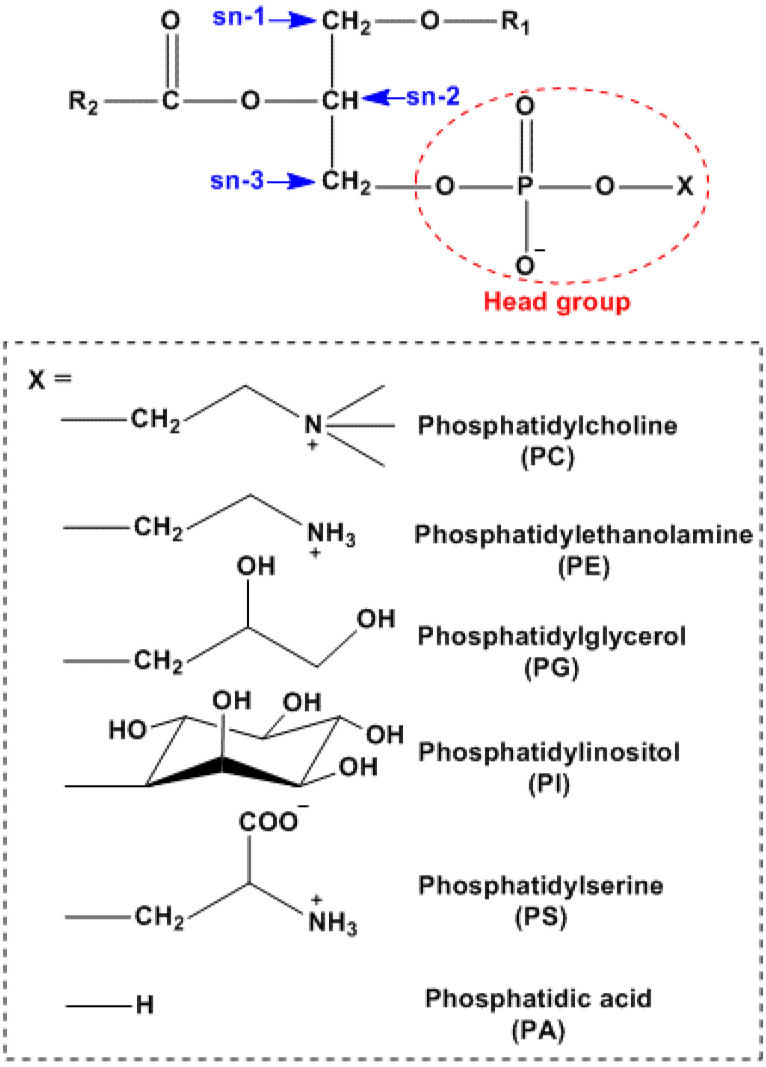

Figure 7. Structure of glycerophospholipids (GPLs). GPLs consist of a glycerol backbone, a polar head group, and two fatty acid tails (R1 and R2).

1.4.2 Lipidomics

The biological system can be broken down to essentially four basic components, (i) genome, (ii) transcriptome, (iii) proteome, and (iv) metabolome which includes the lipidome (Figure 8). The degree of complexity increases from the genome (made up of essentially four nucleotides) and transcriptome, to the proteome (made up of 20 amino acids), to the metabolome (shows variability at the atomic level and includes nucleotides, amino acids and small peptides, sugars, and lipids)[148]. The lipidome could be defined as the entire collection of chemically distinct lipid species in a cell, an organ, or a biological system.

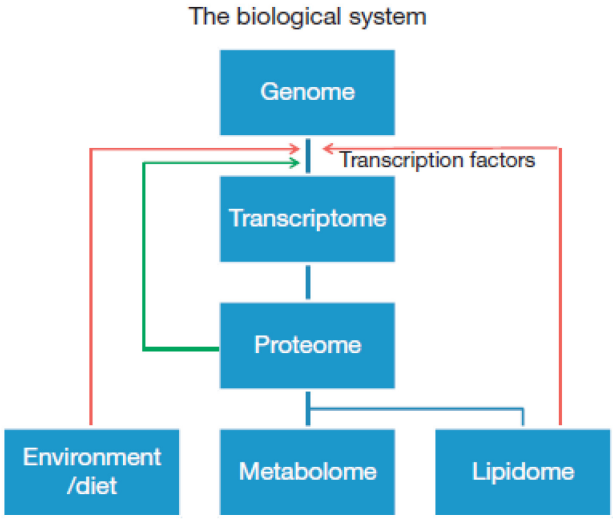

Figure 8. Schematic representation of the interrelation between the genome, transcriptome, proteome, metabolome, and lipidome. (adapted from Griffiths et al. [148])

Hence, lipidomics could be referred to as an analytical chemistry-based research field styding lipidomes in a large scale and at the levels of intact molecular species, in analogy to other "-omics" disciplines[145]. Research in lipidomics has largely focused on the following areas:

- Identification of novel lipid classes and molecular species.
- Development of quantitative methods for the analysis of lipids in different biological systems.
- Network analysis to clarify metabolic adaptation in health and disease tissue.
- Biomarker analysis to facilitate diagnosis of disease states.
- Tissue mapping of altered lipids present in complex organs.
- Bioinformatics approaches for the automated high-throughput processing and molecular modeling of lipidomics data.

Many analytical methods have been developed for the analysis of lipids, including thin-layer chromatography (TLC)[149], gas chromatography(GC)[150], liquid chromatography (LC), enzyme-linked immunosorbent assays (ELISA)[151], nuclear magnetic resonance (NMR)[152], and mass spectrometry (MS)[153]. Among them, MS-based methods achieve the highest sensitivity and specificity, throughput, and

accuracy[154]. The following section presents an overview of popular MS-based methods for lipid analysis.

Mass spectrometry-based lipidomics approaches

MS-based techniques can be different in their analytical spectrum (e.g., 'targeted analysis' vs. 'global analysis'). They also differ with respect to the absence or presence of extraction protocols and/or liquid chromatography (LC) prior to the mass spectrometric analysis[155]. In principle, lipids can be analyzed directly from the biological materials (tissue section or cell samples) by MS imaging[156]. Alternatively, biological samples are extracted with organic solvents and lipid solutions are analyzed either by shotgun lipidomics[157] or by chromatography-based lipidomics, particularly LC-based lipidomics[158].

Biological lipid extracts are typically complex, including the diversity in lipid classes/subclasses/molecular species and the vast dynamic range in the endogenous contents of individual species. Therefore, reduction of the complexity of lipid extracts is essential for reliable and accurate identification and quantification of individual species in the complex extract. This is particularly important for shotgun approaches because they apply no chromatography for separation or enrichment prior to MS analysis, unlike LC-based lipidomics which achieves this utilizing separation science in addition to enriching the low abundance species[153].

Shotgun lipidomics is a direct infusion-based approach that analyzes lipids without pre-chromatographic separation prior to mass spectrometry. Electrospray ionization (ESI) and matrix-assisted laser desorption ionization (MALDI) are the most widely used ion sources in direct infusion MS analysis.

A unique feature of shotgun lipidomics is the high-throughput analysis of lipids under constant concentration conditions. Particularly during direct infusion ESI-MS analysis, this feature provides many advantages for quantitative applications. Constant interactions between the lipid species are maintained which results in constant ion suppression between the different species and hence constant contribution of an individual lipid species to the ion current in an ESI source[145]. This also allows virtually unlimited time to improve signal/noise ratio and to perform detailed MS/MS

mapping under constant composition of solvents and analytes, in contrary to time constraints present during chromatographic elution[155].

In the practice of shotgun lipidomics, the sample complexity could be reduced either during sample preparation or during MS analysis. Reducing complexity during sample preparation can be done through physical approaches (e.g., liquid/liquid partitioning or solid phase extraction to separate polar vs. nonpolar lipids)[159] or chemical approaches (e.g., base hydrolysis to enrich low abundance sphingolipids from complex lipid extracts containing high abundance phospholipids and/or glycerolipids)[160]. Another possibility is to use derivatization methods to chemically tag specific functional groups of lipids in the extracts[161]. During MS analysis, complexity can be reduced via intrasource separation or selective ionization. In addition, monitoring head group-related fragments that are characteristic to a specific lipid class by MS/MS, selectively detects molecular species within the class without interference from other coexisting classes[162].

On the other hand, the hyphenated technique of HPLC and ESI-MS has become the most widely used method in chromatography-based lipidomics analysis. Selection of a suitable column, optimization of the separation conditions, and appropriate coupling of the LC elution conditions with the MS are essential factors to achieve the best separation of lipid classes and/or lipid molecular species. The use of various types of columns have been reported for different purposes in lipidomics. This includes normal phase, reversed phase, hydrophilic interaction, ion exchange, affinity, in addition to multidimensional LC[163]. A general approach is to use normal-phase liquid chromatography (NPLC) to separate different classes of lipids based on the polar head groups, while reversed-phase liquid chromatography (RPLC) is often used to separate different molecular species in one class based on the different fatty acyl chains[164].

In contrast to shotgun lipidomics, LC-MS methodology has the characteristic feature of changing lipid concentrations in eluents. Hence, identification and quantification of lipid species have to be done “on-the-fly”, i.e. in a limited time frame[145].

Imaging of lipids by mass spectrometry has been recently one of the most exciting areas of lipidomics research. The most promising advantage of MSI is the potential to perform lipid analysis, avoiding extraction and/or separation steps, and to display the *in situ* information[154]. Almost all types of ionization sources have been successfully

applied for MSI of lipids, such as MALDI[18], DESI[165], SIMS[166], and pressurized liquid extraction surface analysis[167]. A discussion of different MSI methods with a focus on MALDI MSI was presented in the first section of the introduction chapter (Chapter 1.2).

1.4.3 Bioinformatics tools in lipidomics

The study of lipidomics, especially non-targeted lipid analysis, has generated overwhelming amounts of data, which need bioinformatics technology to aid in data processing for acquiring meaningful biological information[154]. Development of lipid-centered databases and libraries has become an essential part of lipidomics studies. In the following, a few representative examples of widely used lipid-related databases are presented.

Lipid Maps Structure Database (LMSD) is the largest public database in the world specifically for lipids. It is publicly available at www.lipidmaps.org/data/structure. It uses a hierarchical classification and a nomenclature based on a comprehensive classification scheme proposed by Lipid Maps. A unique Lipid Maps ID number assigned to individual lipid structure, reflects its position in the classification hierarchy. It also offers several online tools for viewing and drawing of lipid structures[168].

METLIN is a metabolomics database developed at the Scripps Research Institute. It is a comprehensive repository of metabolite information and tandem MS data and available online at https://metlin.scripps.edu. METLIN includes masses, chemical formulas, and structures for over 15,000 metabolites including numerous lipid species. Annotated metabolites including lipids are linked to outside resources such as the Human Metabolome Database (HMDB), which makes it easier to find further references about the metabolite[169].

HMDB is a comprehensive database of metabolites found in the human body, created by the Human Metabolome Project and is freely available online at http://www.hmdb.ca/. It contains the information on chemistry, clinical data, and molecular biology for more than 6500 metabolites including lipids[170].

METASPACE, a platform for metabolite annotation of high-resolution mass spectrometry imaging (HR MSI) data, has recently been developed. It is a part of the European project METASPACE and is freely available online at

http://metaspace2020.eu/#/about. The framework offers an open-data repository where the metabolite annotations from datasets provided by the community are public and can be browsed or exported by active users. It is the first comprehensive bioinformatics engine that allows FDR-controlled metabolite annotation for HR MSI data. It is based on the following principles: database-driven annotation by screening for metabolites with known sum formulas, an original metabolite-signal match (MSM) score combining spectral and spatial measures, and a novel target–decoy FDR-estimation approach with a decoy set generated via the use of implausible adducts[171].

2 Aims and scope

Cisplatin has been widely used for treatment of solid tumors, usually in combination with other drugs[172]. It induces apoptosis or necrosis of tumor cells mainly by binding to DNA and distorting its functions[173]. A serious clinical side effect of cisplatin treatment is nephrotoxicity, occurring in one third of the patients[174]. Accumulation of cisplatin in the kidney, its main route of excretion, has been reported and the renal damage mainly involves the proximal tubules[175]. This accumulation induces oxidative stress in the kidney and results in increased lipid peroxidation affecting membrane integrity and inducing alteration in the renal lipid profile[176].

The use of MALDI MSI for spatial mapping of the distribution of lipids in tissues has gained increasing interest in recent years[68]. On the one hand, most of the lipid species are particularly suitable for MALDI MSI because they ionize easily and are abundant components of biological systems[177]. They also play essential roles in cell signaling and metabolism and are principal membrane components. On the other hand, MSI allows direct analysis of lipids *in situ*, which helps to distinguish their distribution within tissue substructures, such as kidney[178]. MSI of lipids in kidney tissue allowed to identify alterations during kidney disease[179] and acute renal injury[180].

Considering this, the aim of the first part of this work is to develop a method for mapping the composition of lipids in the kidney tissues of healthy control and cisplatin-treated rats using MALDI MSI. This could help better understand cisplatin-induced alterations in the renal lipid profile and shed light on the underlying pathophysiological processes involved in the nephrotoxic effect of cisplatin therapy.

The choice of the matrix compound and optimizing the deposition of the matrix solution is considered with the aim to enhance the sensitivity. The identification of the lipid ions based on their exact mass is supported by the high mass resolution and accuracy of the orbitrap MS. On-tissue MS/MS approaches including fragment ion imaging are employed to confirm the identification of the lipid species. The distribution of the identified lipids in control and cisplatin-treated tissues is compared to identify cisplatin-induced renal effects.

On the other hand, the variable influence of several experimental and instrumental factors[181] results in non-linear variability in extraction, desorption, and ionization of analytes across the tissue[42]. This limits the use of image intensities of the species of interest obtained during MALDI MSI for intersample comparison[98]. Several methods have been described for signal normalization of MALDI MSI data to tackle the challenges of uncontrollable variability in signal intensity, which hinders its use for relative quantitative applications[69, 95, 98-105]. Among these approaches, the ones which employ the use of internal standards have gained particular importance, enabling pixel-by-pixel correction of raw intensities[42].

The second part of this work aims at developing a novel method for normalization of lipid signals using dual lipid-metal internal standards. The method is developed with the target to allow intersample comparison of lipid intensity in kidney tissues with relative quantification purposes. The use of the inkjet printer as a cost-effective tool to automatically, homogenously, and reproducibly deposit the matrix and internal standards is considered. Total metal content determination using ICP-MS is used to confirm consistency of the matrix deposition in the different experiments. Finally, application of the developed method to normalize ion intensities of kidney lipids in control and cisplatin-treated rats is evaluated.

3 Results and discussion

3.1 Lipid imaging by MALDI LTQ Orbitrap mass spectrometry in kidney sections under cisplatin treatment

3.1.1 Overview

The antitumor agent cisplatin has been successfully employed for the treatment of many solid tumors. It exerts its cytotoxic effect by binding DNA in the nucleus and inducing either apoptosis or necrosis of tumor cells[173]. Other cytotoxic mechanisms of cisplatin possibly involve interactions with non-DNA targets, such as proteins[182] and lipids[183]. Nephrotoxicity is a limiting side effect associated with cisplatin-based therapy, and occurring in about one-third of the patients[174]. Accumulation of cisplatin is relatively higher in the kidney, its main route of excretion, in comparison to other organs. The renal damage involves an acute injury of the renal proximal tubule[174], where accumulation of cisplatin was found[175].

Several studies reported changes in the lipid profile of the kidney as a consequence of cisplatin-induced renal injury, this included increased lipid peroxidation and impaired cell membrane integrity[176]. Also, elevation of non-esterified fatty acids and triglycerides levels in kidney during cisplatin treatment was found[184]. Moreover, membranes of sensitive and resistant cells showed alteration in their phospholipid composition after cisplatin treatment[185].

The mapping of tissue lipids by MALDI MSI has gained increasing interest in recent years[68]. On the one hand, most of the lipid species are particularly suitable for MALDI MSI because they ionize easily and are abundant components of biological systems[177]. On the other hand, MSI allows direct analysis of lipids *in situ*, which helps to distinguish their distribution within tissue substructures, such as kidney[178]. Previous works have shown that mass spectrometry imaging of kidney lipids helped distinguish specific lipids within kidney substructures[178, 186] and identify alterations occurring during acute kidney injury[180] and other kidney diseases[179, 187, 188]. Considering this, screening the spatial distribution of kidney lipids could help

understand more about lipid alterations involved in cisplatin-induced nephrotoxicity and shed light on the biochemical and pathophysiological processes involved.

In this section, a method for mapping of lipid composition in positive ion mode using MALDI-LTQ-Orbitrap in rat kidney sections was developed, including optimization of matrix deposition.

The method was applied to examine the lipid profile in kidney sections of control and cisplatin-treated rats. High mass resolution and accuracy of MALDI-LTQ-Orbitrap, on-tissue tandem MS measurements, and fragment ion imaging reinforced the identification of lipid species. Lipids showing modified renal distribution patterns due to cisplatin-induced nephrotoxicity were found. These species could serve as complementary tools for renal damage assessment or as therapeutic targets.

3.1.2 Histopathological assessment of cisplatin-induced renal damage

As mentioned earlier, it is well recognized that the proximal tubule is the major site of renal injury during cisplatin nephrotoxicity[174]. Impaired renal function associated with cisplatin treatment has been related to the activation of complex signaling pathways that lead to injury and death (necrosis and apoptosis) of the renal tubular cells[176, 189]. Morphological assessment of the optical microscope images of H&E-stained kidney sections showed signs of renal damage in kidney section of cisplatin-treated rat (Figure 9c, d) in comparison to control healthy tissue (Figure 9a, b). Signs of toxicity included protein casts, tubular necrosis, and tubular swelling (marked with arrows in Figure 9c, d), which were observed mainly in the cortex, corticomedullary junction, and outer medulla, where the proximal tubule is located.

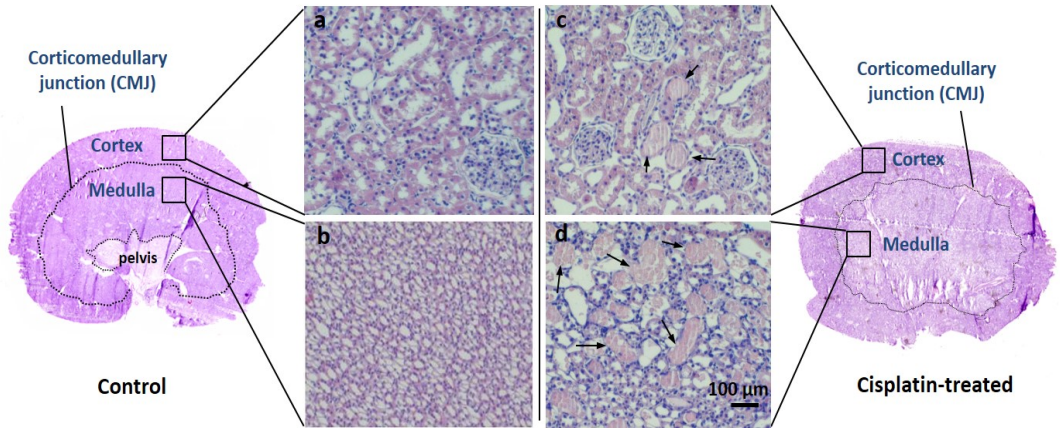

Figure 9. Microscope images for hematoxilin-eosin stained kidney sections showing the morphology of renal cortex and medulla from control (a and b) and cisplatin-treated (c and d) rats. Signs of cisplatin-induced renal damage are marked with arrows, e.g. showing protein casts.

3.1.3 Evaluation of the matrix of choice

The matrix is applied as fine spray in a quickly evaporating solution containing (0.1-1%) TFA for positive ion mode analysis. Extracting the maximum amount of the analyte from the sample while minimizing its delocalization and ensuring homogenous crystallization is the aim of optimization of matrix application[55]. The choice of matrix is normally determined by the mass range over which the experiment is to be performed. For small and medium molecular weight masses either α-cyano-4-hydroxycinnamic acid (α-CHCA) at 10–20 mg mL^{-1} or 2,5-dihydroxybenzoic acid (DHB) at 40–100 mg mL^{-1} is often used[54].

Matrix composition was optimized by monitoring the mass range between 700 - 900 m/z, where most of the signals belonging to tissue lipids could be detected[190]. Figure 10 shows the off- and on-tissue averaged mass spectra generated in the same imaging measurement of a kidney section coated with DHB solution (60 mg mL^{-1} in 70% MeOH, 0.1% TFA). Signals of tissue lipids were evident through comparing the highlighted mass range in both spectra (Figure 10). Signals in the lower mass range (below m/z 700) are common to both spectra and could be attributed to a contribution of DHB matrix ions.

Slight enhancement of the low mass range in the on-tissue spectrum with respect to the off-tissue spectrum was observed and could be explained due to additional contribution

of tissue signals like lysophospholipids (intermediates involved in biosynthesis and metabolism of phospholipids)[191].

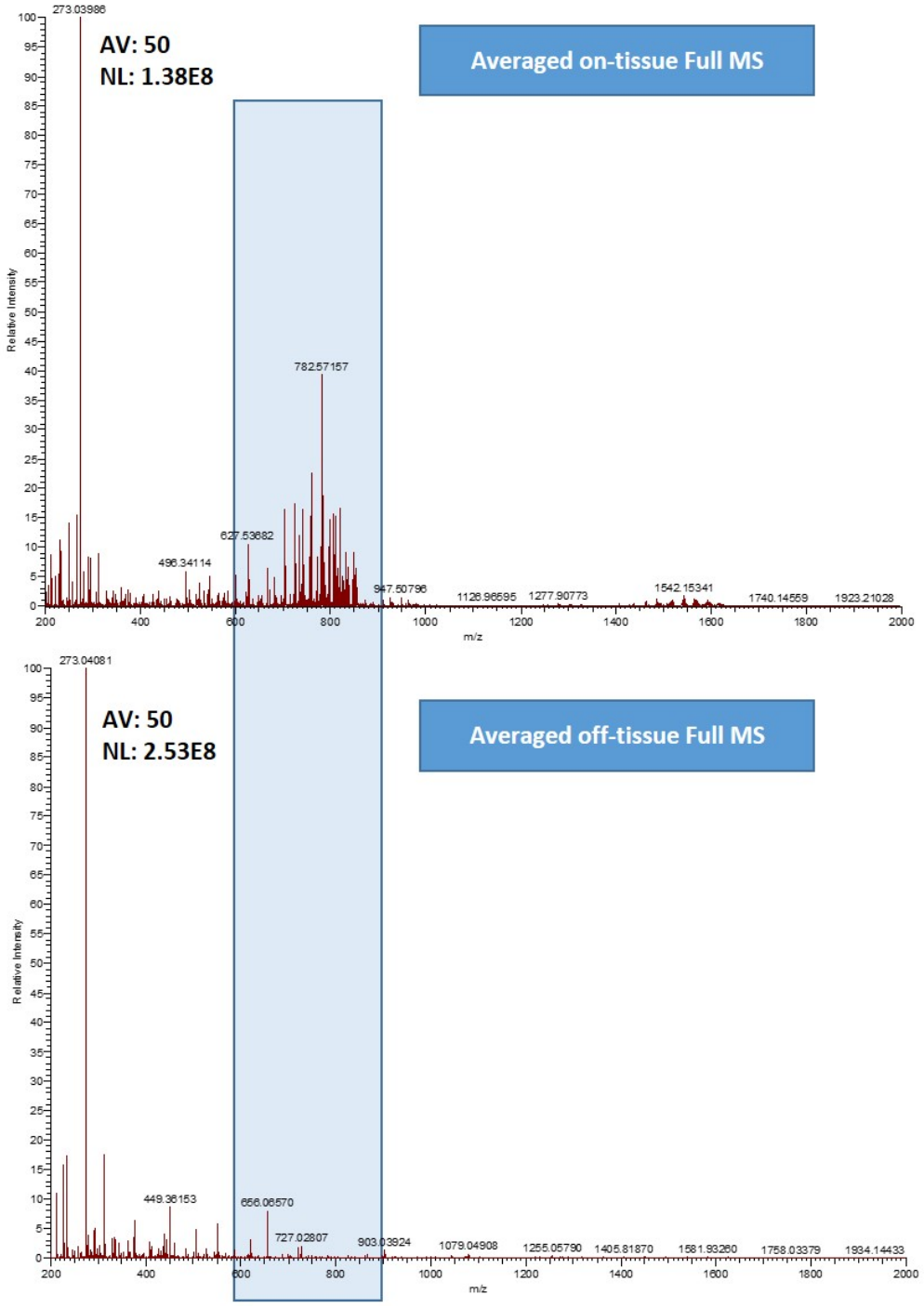

Figure 10. Averaged off- and on-tissue mass spectra showing the signals of tissue lipids in the on-tissue spectrum (mass range 700-900 m/z).

Different concentrations of DHB and α-CHCA were tested to optimize the matrix deposition. The signal intensity and tissue images of lipids were consequently assessed. Control kidney samples were spray-coated with either DHB (20, 40, and 60 mg mL^{-1} in 70% MeOH, 0.1% TFA) or α-CHCA (10 and 20 mg mL^{-1} in 60% ACN, 0.1% TFA). MALDI imaging experiments of the coated tissue sections were performed at 500 µm and TIC-normalized signal intensity of various endogenous lipids was compared for the different matrix compositions. Figure 11 illustrates the mean intensity values of seven tissue lipids, which were calculated from parallel sections from the same rat kidney (n=3). In a single measurement, the intensity value was generated by averaging 20 on-tissue spectra.

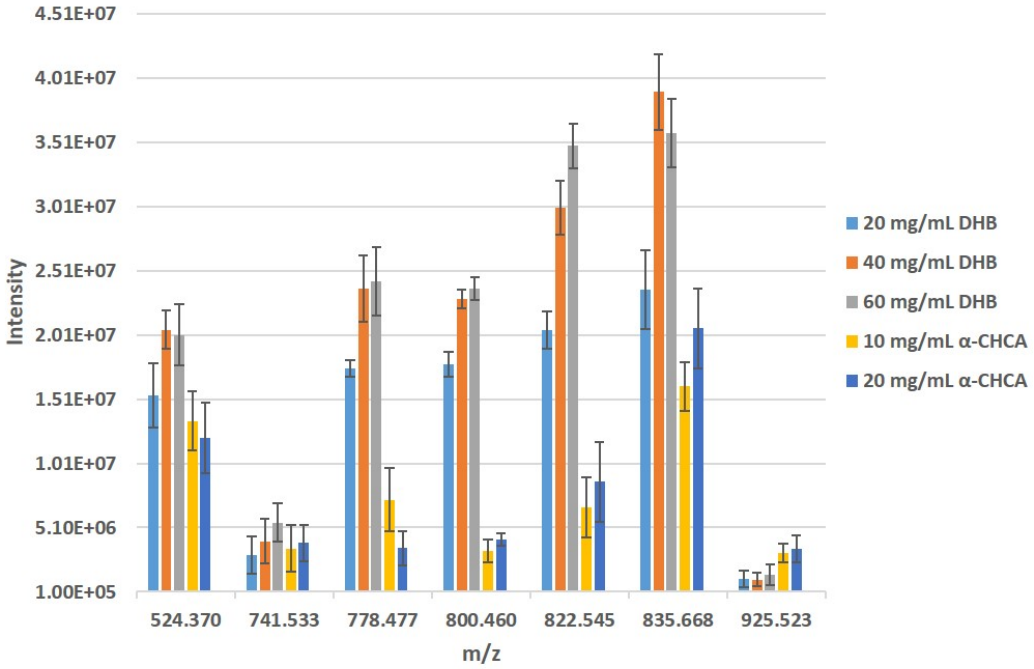

Figure 11. Effect of matrix composition on the signal intensity of tissue lipids. Mean signal intensity of the following tissue lipids: m/z 524.370, m/z 741.533, m/z 778.477, m/z 800.460, m/z 822.545, m/z 835.668 and m/z 925.523, in kidney sections spray-coated with different concentration of either DHB or α-CHCA, is shown.

Most of the lipid species in Figure 11 showed significant signal enhancement with DHB in comparison to α-CHCA. PE(36:4) at m/z 778.476, PE(38:7) at m/z 800.460, and PC(36:3) at m/z 822.545 showed at least a two-fold increase in intensity with different concentrations of DHB (20, 40, 60 mg mL^{-1}). LPC(18:0) at m/z 524.370, SM(d34:1) at m/z 741.533, and SM(d36:2) at m/z 835.668 also showed remarkable enhancement in

intensity at higher concentrations of DHB (60 mg mL^{-1}). Only a few lipids such as PI(38:4) at m/z 925.523, showed higher intensity with α-CHCA.

Figure 12 shows the effect of varying number of deposition/drying cycles on the MALDI images of PE(38:7), PC(36:3), SM (d36:2), and PI(38:4). Several matrix deposition/drying cycle amounts of either DHB (60 mg mL^{-1} in 70% MeOH, 0.1% TFA), or α-CHCA (20 mg mL^{-1} in 60% ACN, 0.1% TFA) within each tissue (Figure 12a and b), were applied. The first tissue (Figure 12a) received 10, 15 and, 20 cycles of DHB (each cycle consisted of 20s of deposition+ 20 s of drying), while the second one (Figure 12b) had 9, 12, and 15 cycles of α-CHCA (each cycle consisted of 40 s of deposition+ 20 s of drying). The use of less concentrated matrix solution required double the number of deposition cycles with no remarkable gain in spectral quality, hence higher concentration of both matrices was preferred to shorten the time needed for matrix application. In addition, quick solvent evaporation should minimize the delocalization of tissue lipids and limit it within the matrix crystals formed.

The ion extracted images of the lipids in both tissues were normalized to identical color-scale bars for each ion species to allow comparison of signal level. In general, the images showed higher signal of the lipids with DHB deposition (Figure 12c, e, g, i) in comparison to α-CHCA (Figure 12d, f, h, j), confirming the previous results in Figure 11. Deposition of 15 cycles of DHB resulted in higher ion intensities, increasing the number of spray cycles did not further enhance ionization. On the other hand, optimum ionization for α-CHCA was obtained at 12 deposition cycles.

Difficulties were encountered to reproducibly obtain a homogenous coat of α-CHCA due to repeated blocking of the airbrush; which resulted in sputtering of the matrix solution, complicated the estimation of the applied amount of matrix and reduced the reproducibility of ion intensities obtained in different measurements.

On the other hand, DHB solution was more feasible to handle and showed consistently higher ion intensities for most of the lipids. Accordingly, application of 15 cycles (20s of deposition+ 20 s of drying) of 60 mg mL^{-1} DHB in 70% MeOH, 0.1% TFA was used for further analysis of the lipids in kidney tissues, and no further optimization of α-CHCA was done.

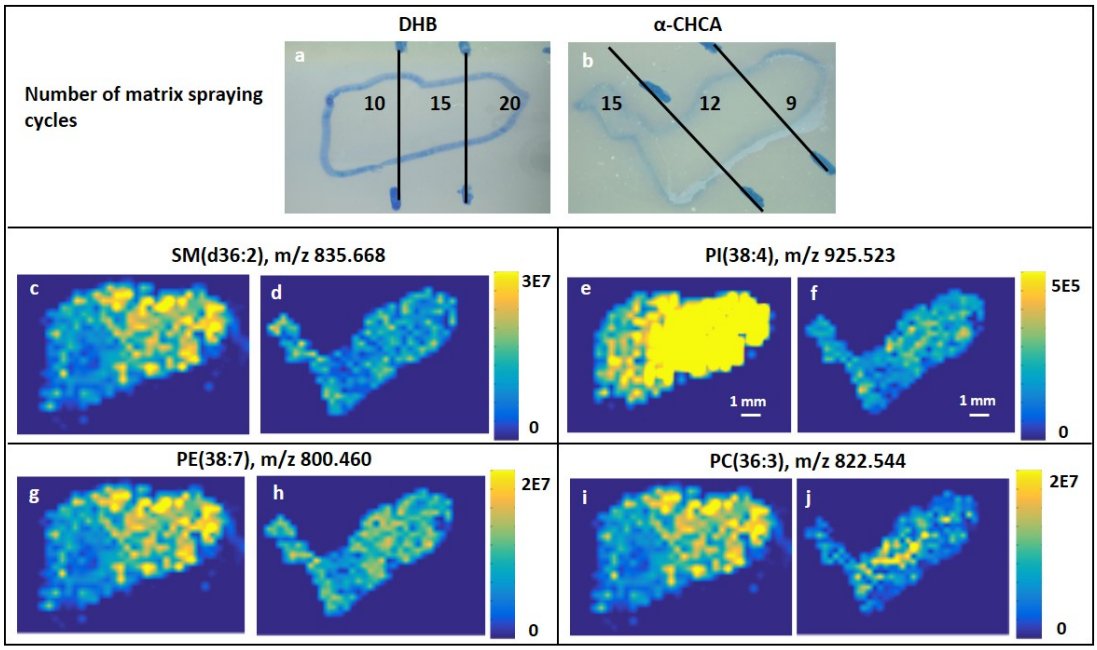

Figure 12. Effect of the number of matrix deposition cycles on the ion extracted MALDI images of tissue lipids for two tissue sections spray-coated either with DHB or α-CHCA. (a & b) The optical images of the two kidney sections showing the number of cycles within each tissue. MALDI images of m/z 835.668 (c & d), m/z 925.523 (e & f), m/z 800.460 (g & h), and m/z 822.544 (i & j) for the two samples.

3.1.4 Assessment of reproducibility

To demonstrate the reproducibility of the method, the distribution and abundance of different tissue lipids in serial tissue sections (n=3) of a vehicle control kidney were assessed. Two tissues (Figure 13 a, d, g and b, e, h) were analyzed in two consecutive days at 100 µm resolution. Whereas the third tissue (Figure 13c, f, i) was stored at -80 °C for two months, in order to check the method reproducibility over time, then it was spray-coated with the matrix and analyzed at lower resolution (185 µm).

Depending on the measurement dimensions, the high mass resolution imaging analysis of a single kidney tissue at 100 µm resolution lasts for 12 h in average. For proper comparison of ion intensities, conventional total ion current (TIC) normalization was used to compensate for drifts in matrix deposition and variable instrumental performance over time[100, 106]. This was particularly relevant to compare the abundance and tissue distribution of tissue lipids in different samples as seen in Figure 13. TIC-normalized images of m/z 524.370 (Figure 13a, b, c), m/z 778.476 (Figure 13d, e, f), and m/z 822.544 (Figure 13g, h, i) showed comparable tissue localization with

clearly defined cortical and medullar distributions. Also, similar relative ion intensities were observed in the three samples, indicating that the method is reproducible and robust over time.

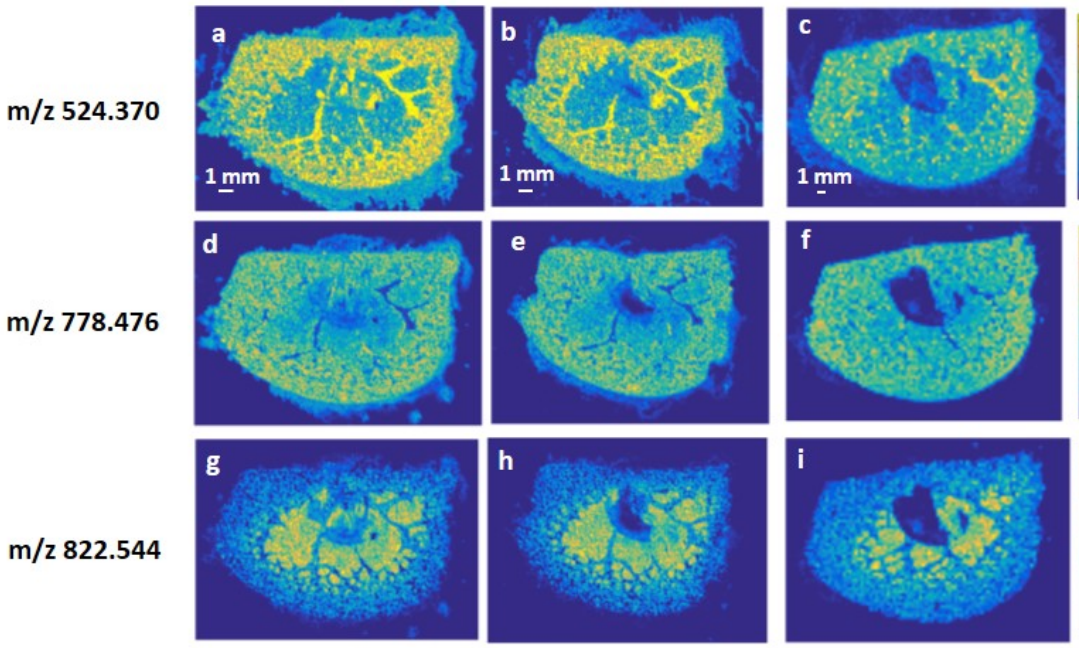

Figure 13. TIC-normalized MALDI images show the reproducibility of distribution and relative intensity of m/z 524.370 (a, b, c), m/z 778.476 (d, e, f), and m/z 822.544 (g, h, i) in 3 parallel sections in the same kidney tissue. Two tissues were measured at 100 µm resolution ((a, d, g), (b, e, h)), and the third at 185 µm (c, f, i).

3.1.5 Assignment of lipids

Lipids are produced during MALDI imaging mainly as highly abundant singly charged ions in the m/z range between 700 to 900[190]. Most lipids have characteristic features which increase the certainty of their identification using high-performance mass spectrometers with sufficient mass resolution. These features include the relatively high mass defect resulting from the contribution of large number of hydrogen atoms present in the acyl chains of the fatty acids. Also, the high number of carbon atoms results in a characteristic isotopic pattern, where a relatively high abundance of the ion at 1 Da higher in mass is observed, due to the abundance of carbon-13 found in nature (1.1 % relative abundance)[156]. The high mass resolution and accuracy provided by LTQ orbitrap instrument allowed the identification of lipids based on the exact mass of the monoisotopic signal of the precursor ion. Mass lists from MALDI measurements of

control and cisplatin-treated samples were used for exact mass search in LIPIDS MAPS (www.lipidmaps.org) with a tolerance window of 5 ppm.

3.1.6 The role of high resolution MS (HRMS) and MS/MS imaging

Identification of lipids in complex biological samples solely based on database search using the m/z value of the monoisotopic peak is often times inconclusive. In many cases, the database search could return several matching hits including: different lipid species having an exact mass value within the specified tolerance window (with different empirical formulas), isobaric species from different classes (with the same empirical formula, such as PC and PE), and isomers from the same lipid class. The high mass accuracy provided by the Orbitrap mass analyzer allowed a narrow tolerance window of 5 ppm, which reduced the search results. Also, ion images of various adducts of the lipid species (H^+, Na^+, and K^+) showed corresponding distribution patterns in the tissue, which reinforced the lipid identity. More importantly, direct on-tissue MS/MS analysis was invaluable to identify and differentiate isobaric species, where daughter ions in the MS2 spectrum allowed recognize characteristic fragmentation patterns of the different lipid subclasses (e.g. NL of 43 for PE species and 59, 183 for PC species).

In this section, some examples demonstrate the usefulness of high mass resolution, on-tissue MS/MS, and fragment ion imaging to improve the certainty of lipids identification.

The high performance of Orbitrap detection allowed complete resolution of precursor ions with close m/z values, thus, their respective tissue localization could be visualized in the MALDI image. The full MS spectrum in Figure 14b shows complete resolution of the precursor ions of $[PS(38:5) + K]^+$ at m/z 848.4827 and $[PC(38:4) + K]^+$ at m/z 848.5561 with a mass difference of 0.0734 Da. The ion extracted images of both species (Figure 14a) show their tissue distribution and the difference in their relative abundance. On-tissue MS/MS analysis showed that the two precursor ions are mixed in the ion trap and the MS2 spectrum showed product ions belonging to both species (Figure 14c). The MS2 spectrum of the isolated precursor ion at m/z 848 at CID 35.00 in Figure 14c shows fragment ions corresponding to the loss of trimethylamine (at m/z 789.482 equivalent to $[M+K-59]^+$) and phosphocholine (at m/z 665.490 equivalent to $[M+K-183]^+$) for $[PC(38:4) + K]^+$ at m/z 848.5561. In addition, the fragment ion at m/z

761.449 equivalent to the loss of serine (NL87) confirmed the assignment of [PS(38:5) + K]$^+$ at m/z 848.4827. It could be observed that the product ions were present at a relative abundance ratio consistent to that of the parent ions.

Another example illustrated the usefulness of fragment ion imaging for lipid mapping (Figure 15). MALDI images of the fragment ions at m/z 789.482 and m/z 665.490 (Figure 15b and c) showed similar tissue localization to that of the precursor ion [PC(38:4) + K]$^+$ at m/z 848.5561(Figure 15a). Whereas, the distribution of the fragment ion at m/z 761.449 (Figure 15e) was analogous to its precursor ion [PS(38:5) + K]$^+$ at m/z 848.4827(Figure 15d). Hence, the same distribution of PC(38:4) and PS(38:5) could be obtained in the MS and the MS/MS images. This suggested fragment ion mapping as a reliable strategy for confirmation of lipid assignment, which could be particularly useful where isobaric interferences might be significant.

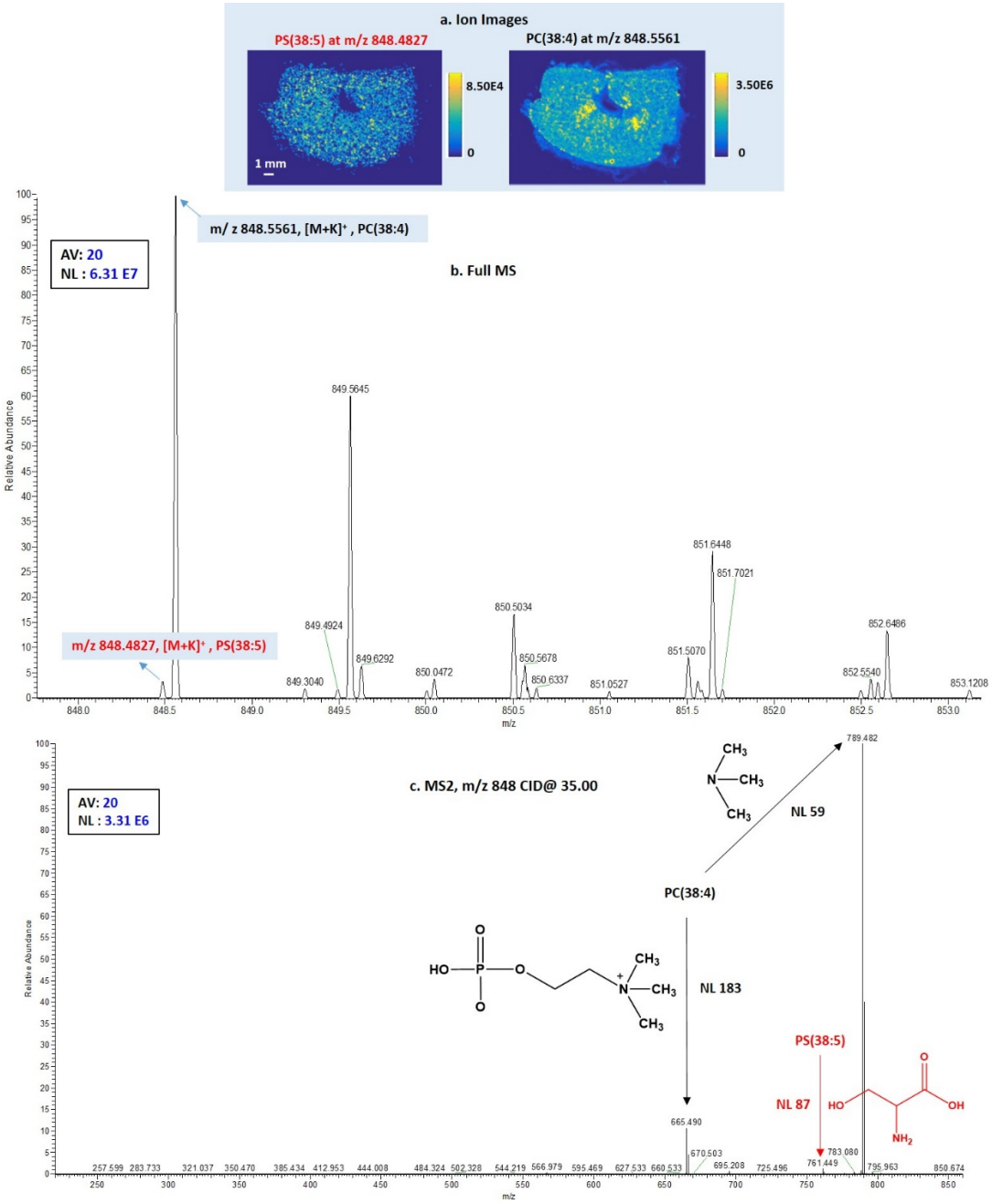

Figure 14. (a) MALDI images of $[PS(38:5) + K]^+$ at m/z 848.4827 and $[PC(38:4) + K]^+$ at m/z 848.5561. (b) MALDI Full MS spectrum showing complete resolution of m/z 848.4827 and m/z 848.5561. (c) MALDI-CID-MS2 spectrum of m/z 848. Assignment of the most relevant fragment ions at m/z 789.482, m/z 665.490, and m/z 761.449 has been indicated.

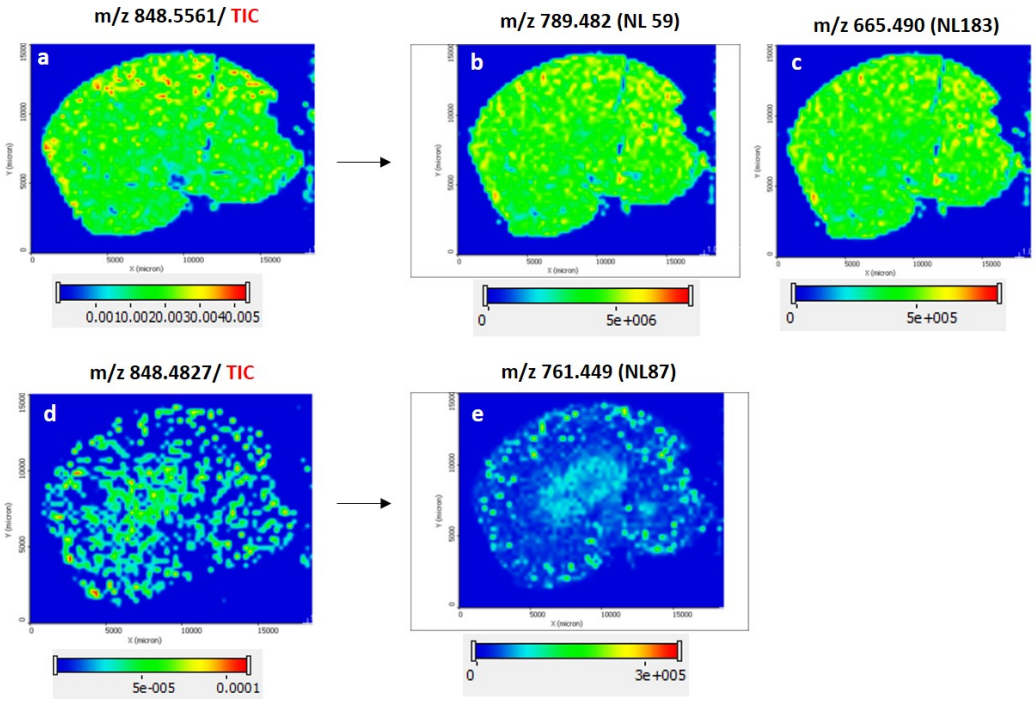

Figure 15. Fragment ion imaging shows similar tissue distribution of precursor and fragment ion. (a and d) TIC-Normalized MALDI images show the renal distribution of m/z 848.5561 and m/z 848.4827. (b and c) MALDI image showing distribution of fragment ions at m/z 789.482 and m/z 665.490 (precursor ion m/z 848.5561). (e) MALDI image showing distribution of fragment ion at m/z 761.449 (precursor ion m/z 848.482).

In other cases, the assignment of several NL in the MS2 spectrum allowed identify isobaric species. The MALDI-CID-MS2 spectrum of the isolated ion at m/z 796 in Figure 16a showed typical NL of trimethylamine (at m/z 737.451 corresponding to $[M+K-59]^+$) and phosphocholine head group (at m/z 613.458 corresponding to $[M+K-183]^+$), which concluded the assignment of $[PC(34:2) + K]^+$ at m/z 796.524. On the other hand, the fragment ion at m/z 753.480, which is equivalent to $[M+K-43]^+$ indicating NL of vinyl amine, confirmed the assignment of $[PE(37:2) + K]^+$ with the same exact mass. The low relative abundance of the daughter ion at m/z 753.480 suggested that PC(34:2) would be the main species represented in the MALDI image (Figure 16b).

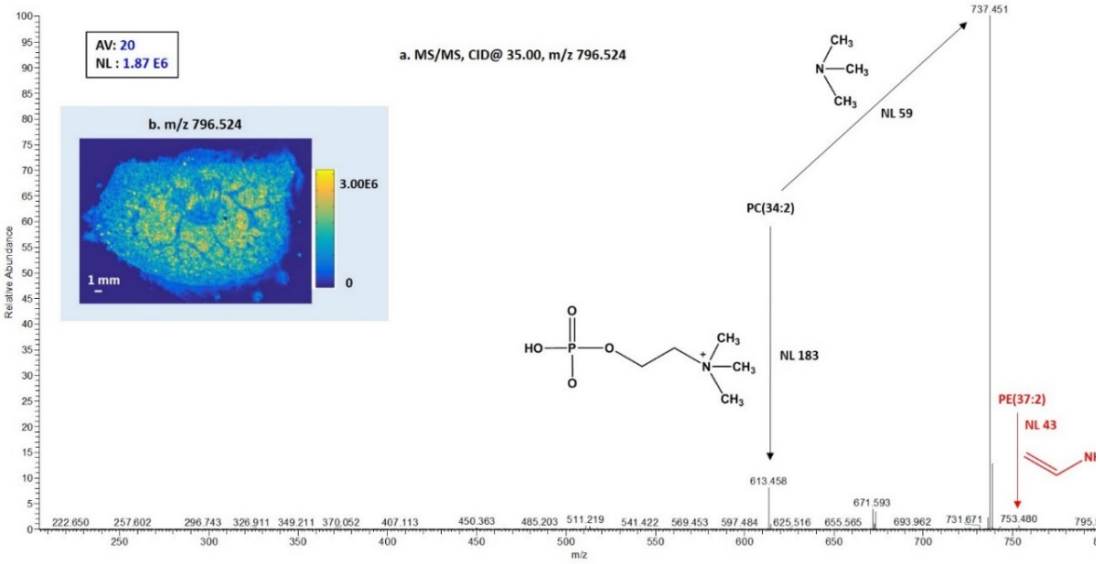

Figure 16. (a) MALDI CID-MS2 spectrum of m/z 796.524 showing the assignment of several NL, which indicated the presence of isobaric species. The transitions m/z 796.524→737.451 and m/z 796.524→613.458 indicate PC(34:2), while the transition m/z 796.524→753.480 indicates PE(37:2). (b) Ion extracted image of m/z 796.524.

The previous findings showed that careful interpretation of on-tissue MS/MS data is essential for unambiguous identification of lipid species. In most of the cases, MS/MS analysis led to the assignment of the lipid family. In other cases, lipids were present at a relatively low abundance, which complicated the isolation of the precursor ion in the ion trap, hence, no useful fragmentation could be obtained and only putative identification was used.

3.1.7 Lipid imaging for screening of cisplatin-induced effects

Comparison of TIC-normalized images of lipid ions detected in positive ion mode analysis in control and cisplatin-treated kidney samples was performed to explore the ones showing difference in tissue distribution, which could be attributed to cisplatin effect. H&E staining images of serial tissue sections were compared alongside with MALDI images for proper comparison and identification of renal structures. This resulted in a total of 20 lipid species (comprising 45 ion adducts), which revealed clear differences in tissue localization under cisplatin treatment with respect to healthy control samples. Table 2 shows a list of the lipids showing differential tissue distribution in control and cisplatin-treated samples in positive ion mode. The listed lipids comprised 12 PC, 2 PE, 2 PI, 1 SM, 1 LPC, 1 PG, and 1 SM. As seen in Table 2,

some of the lipids could be found in multiple ionization states (H^+, Na^+, and K^+ adducts). In addition, some PC species underwent in-source fragmentation (NL of 59 corresponding to trimethylamine), which resulted in the detection of $[(M-59) + Na/K]^+$ adducts.

Table 2. Lipids showing differential renal distribution in control and cisplatin-treated samples. Observed m/z, adduct type, lipid species, empirical formula, calculated m/z, and error in ppm according to LIPID MAPS assignment are shown. * indicates putative assignment for species with no useful fragmentation data.

Observed m/z	**Adduct**	**Assignment, empirical formula**	**Calculated m/z**	**Δm, ppm**
524.3706	$[M+H]^+$	LPC(18:0) C26H54NO7P	524.3711	-0.89
697.4774	$[M+Na-59]^+$	PC(32:0) C40H80NO8P	697.4779	-0.68
713.4526	$[M+K-59]^+$		713.4518	1.10
734.5698	$[M+H]^+$		734.5694	0.50
756.5525	$[M+Na]^+$		756.5514	1.48
772.5267	$[M+K]^+$		772.5253	1.79
770.5101	$[M+K]^+$	PC(32:1) C40H78NO8P	770.5096	0.65
800.5585	$[M+K]^+$	PC(34:0) C42H84NO8P	800.5566	2.37
723.4929	$[M+Na-59]^+$	PC(34:1) C42H82NO8P	723.4935	-0.86
739.4664	$[M+K-59]^+$		739.4675	-1.44
760.5835	$[M+H]^+$		760.5851	-2.08
798.5420	$[M+K]^+$		798.5410	1.30

Observed m/z	Adduct	Assignment, empirical formula	Calculated m/z	Δm, ppm
721.4812	$[M+Na-59]^+$	PC(34:2)	721.4778	4.71
737.4499	$[M+K-59]^+$	C42H80NO8P	737.4518	2.57
758.5722	$[M+H]^+$		758.5694	3.69
780.5533	$[M+Na]^+$		780.5513	2.56
796.5282	$[M+K]^+$		796.5253	3.64
763.4696	$[M+K-59]^+$	PC(36:3)	763.4675	2.80
822.5447	$[M+K]^+$	C44H82NO8P	822.5410	4.54
761.4524	$[M+K-59]^+$		761.4518	0.77
804.5514	$[M+Na]^+$	PC(36:4) C44H80NO8P	804.5514	-1.84
820.5244	$[M+K]^+$		820.5253	-1.12
802.5355	$[M+Na]^+$	PC(36:5)	802.5357	-0.28
818.5074	$[M+K]^+$	C44H78NO8P	818.5097	-2.77
810.5996	$[M+H]^+$		810.6007	-1.40
832.5812	$[M+Na]^+$	PC(38:4) C46H84NO8P	832.5827	-1.78
848.5561	$[M+K]^+$		848.5566	-0.61
856.5814	$[M+Na]^+$	PC(40:6)	856.5827	-1.49
872.5584	$[M+K]^+$	C48H84NO8P	872.5566	2.04

Observed m/z	**Adduct**	**Assignment, empirical formula**	**Calculated m/z**	**Δm, ppm**
870.5407	$[M+K]^+$	PC(40:7) C48H82NO8P	870.5410	-0.30
854.5715 **892.5234**	$[M+H]^+$ $[M+K]^+$	* PC(42:10) C50H80NO8P	854.5695 892.5254	2.34 -2.22
762.5057 **778.4769**	$[M+Na]^+$ $[M+K]^+$	PE(36:4) C41H74NO8P	762.5044 778.4783	1.76 -1.81
784.4879 **800.4603**	$[M+Na]^+$ $[M+K]^+$	PE(38:7) C43H72NO8P	784.4888 800.4627	-1.10 -3.00
762.4540	$[M+Na]^+$	* PI-Cer(t30:1) C36H70NO12P	762.4528	1.57
817.4381	$[M+K]^+$	* PG(37:7) C43H71O10P	817.4416	-4.28
909.5472 **925.5233**	$[M+Na]^+$ $[M+K]^+$	PI (38:4) C47H83O13P	909.5464 925.5203	0.93 3.25
815.6999 **837.6801** **853.6564**	$[M+H]^+$ $[M+Na]^+$ $[M+K]^+$	SM (d42:1) C47H95N2O6P	815.7001 837.6820 853.6559	-0.19 -2.27 0.54
931.5281 **947.5040**	$[M+Na]^+$ $[M+K]^+$	* PI(40:7) C49H81O13P	931.5307 947.5046	2.79 -0.67

Figures 17 and 18 illustrate examples of the remarkable differences in renal localization of some lipids in cisplatin-treated tissues in comparison to control tissue. MALDI images show the tissue distribution of some lipids in control (Figure 17 & 18 n, o, p, q, r) and two cisplatin-treated tissues, which are obtained from two rats (first: Figure 17 & 18 b, c, d, e, f, and second: Figure 17 & 18 h, i, j, k, l). Both cisplatin-treated tissues showed the same trend in lipid distribution change with respect to the control sample, which confirmed the consistency of the results. Also, comparable ion images of the lipids in the cisplatin-treated tissues indicated the reproducibility of the results, showing corresponding localization and normalized relative abundance.

Ion images of lipids showed several patterns of change in control and cisplatin-treated samples. Some lipids showed relatively higher levels in the cortex of control samples, such as PC(38:4), Figure 17r, and PC(32:0), Figure 17p. After cisplatin treatment, the two species showed either higher medullar levels (PC(38:4), Figure 17f, i), or homogenous tissue distribution (PC(32:0), Figure 17d, j).

Other species showed different pattern of change with a trend of displacement towards the cortex after cisplatin treatment (e.g. (PE(36:4), Figure 17b, h), (PG(37:7), Figure 17e, k), (PI(38:4), Figure 18b, h), and (PC(36:5), Figure 18e, k)). In the healthy sample, those species were either homogenously distributed in the tissue ((PE(36:4), Figure 17n), (PG(37:7), Figure 17q), and (PI(38:4), Figure 18n)), or showed higher local abundance in the outer medulla ((PC(36:5), Figure 18q). Also, some lipids were located in the inner medulla and cortex of the healthy sample (e.g. (PC(32:1), Figure 17o), (PC(34:1), Figure 18o), and (LPC(18:0), Figure 18p)), whereas in the cisplatin-treated samples, they were mostly present in the outer medulla and cortex ((PC(32:1), Figure 17c, i), (PC(34:1), Figure 18c, i), and (LPC(18:0), Figure 18d, j)). The observed alterations in lipid renal distribution in cisplatin-treated samples might be a result of cisplatin-induced nephrotoxicity.

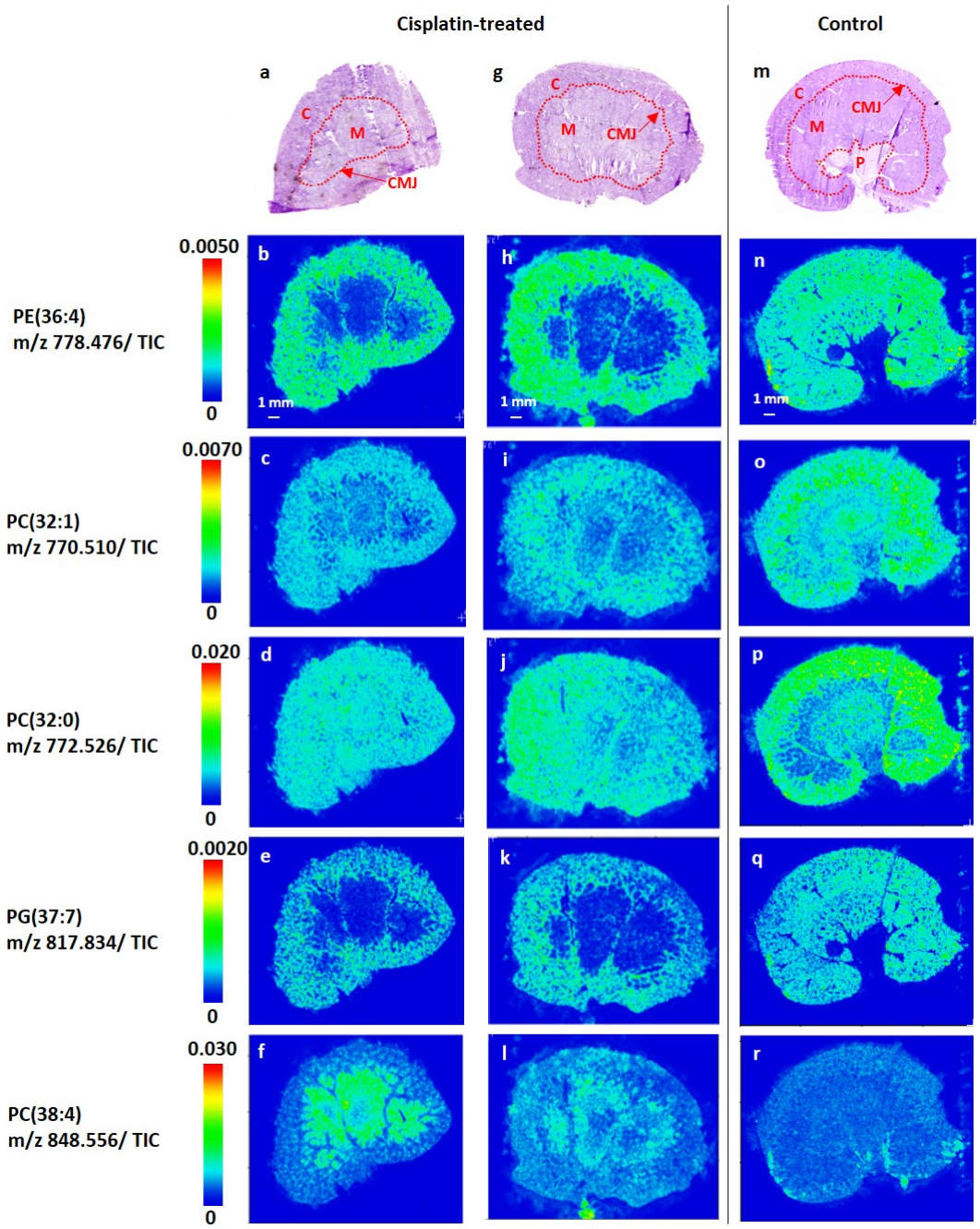

Figure 17. H&E-stained whole kidney sections for two cisplatin-treated samples (a and g) and control (m) showing, C: cortex, CMJ: corticomedullary junction, M: medulla, and P: pelvis. Positive ion mode lipid MALDI images show the renal distributions of PE(36:4) (b, h, n), PC(32:1) (c, i, o), PC(32:0) (d, j, p), PG(37:7) (e, k, q) and PC(38:4) (f, l, r) in the three samples at 100 µm resolution.

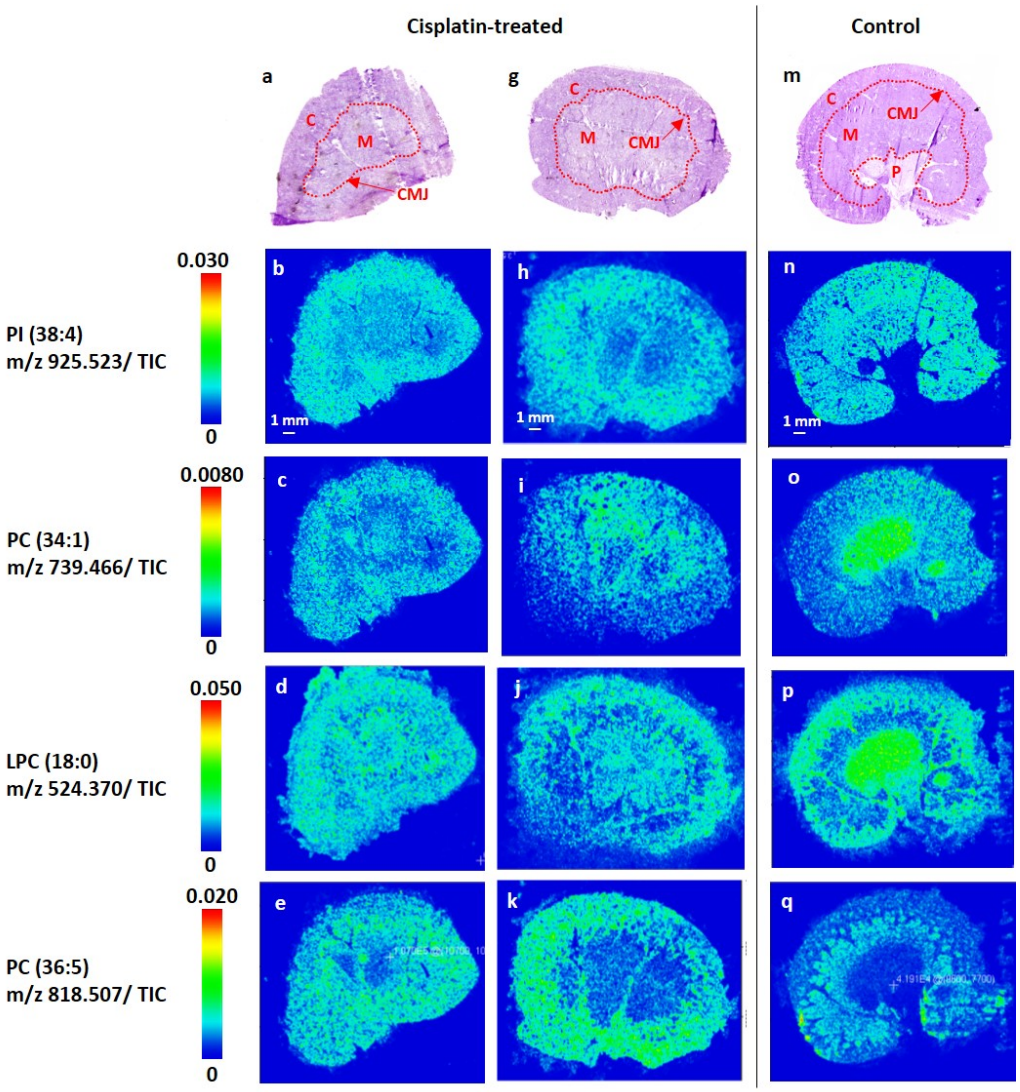

Figure 18. H&E-stained whole kidney sections for two cisplatin-treated samples (a and g) and control (m) showing, C: cortex, CMJ: corticomedullary junction, M: medulla, and P: pelvis. Positive ion mode lipid MALDI images show the renal distributions of PI(38:4) (b, h, n), PC(34:1) (c, i, o), LPC(18:0) (d, j, p), and PC(36:5) (e, k, q) in the three samples at 100 µm resolution.

3.1.8 Significance of cisplatin-induced alterations of tissue lipids

The lipid species with altered renal tissue distribution in Table 2, are glycerophospholipids (GPLs), most of them belonging to the PC lipid subclass, which are principal membrane components[192]. Impaired cell membrane integrity resulting from peroxidation of cellular membrane lipids was reported as a consequence of cisplatin treatment[176]. This suggested the possible dysregulation or release of membrane GPL during cisplatin-induced cell death. In addition, the anatomical differentiation of lipids in cisplatin-treated samples was mainly observed in the cortex and the outer medulla, which agreed well to the histological damage reported in the proximal tubule[174], and also to the local renal accumulation of cisplatin in the cortex and corticomedullary junction[175].

Many of the altered species showed either a homogenous tissue distribution (e.g PC(32:0), Figure 17d, j)), or an increase in relative abundance in the medulla of cisplatin-treated kidney (e.g. (PC(38:4), Figure 17f, i), which could indicate possible migration of the lipids from the dead proximal tubule. On the other hand, some PC species showed different patterns of change with local relative increase of abundance in the cortex after cisplatin treatment (e.g. (PC(36:5), Figure 18e, k), and (PE(36:4), Figure 17b, h)), which could be explained due to the distorted membrane permeability[176]. It is worth to mention that the change pattern of PC(32:0) (Figure 17d, j) with a homogenous distribution and decreased relative abundance in the cortex under cisplatin treatment agreed to the results reporting its total decrease in human embryonic kidney cisplatin-treated cells (HEK293)[193]. Also, PC(36:5) (Figure 18e, k) showed increased relative abundance in the cortex of cisplatin-treated samples, which matched its increase in the same report as well[193]. Additionally, the displacement of LPC(18:0) (Figure 18d, j) towards the outer medulla in the cisplatin treated kidney, could support the study proposing several LPC species as plasma biomarkers of nephrotoxicity during cisplatin treatment[194]. This change suggests further research to investigate if a correlation between the changes in tissue distribution of renal lipids and circulating lipids could exist.

On the other hand, PI species are involved in several cell signaling pathways[195]. Also, they act as precursors for lipid protein kinases, which are involved in mediating the renal tubular injury and play a critical role in the maintenance of renal function in

cisplatin-induced acute renal failure *in vivo*[196]. This could explain the alteration observed for some PI species (e.g. PI(38:4), Figure 18b, h) under cisplatin treatment with a general trend of localizing in the cortex and outer medulla of the treated kidney.

3.1.9 Conclusion and outlook

A simple and robust sample preparation protocol has been developed for imaging of lipids in the kidney sections of healthy control and cisplatin-treated rats using MALDI LTQ Orbitrap MS. Applying the developed method, imaging measurements of control kidney tissues showed reproducible distribution and relative abundances of lipids. The high mass resolution and accuracy of the Orbitrap allowed accurate mass assignment of the lipids. In addition, on-tissue MS/MS measurements and fragment ion imaging further confirmed the assignment of most of the detected lipids. Comparing the distribution of the renal lipids in control and cisplatin-treated samples resulted in 20 lipid species showing clear differences in the examined kidney sections from both groups. The change in tissue distribution of the lipids in the cisplatin group could be explained based on the nephrotoxic effect of cisplatin therapy. This suggests that MALDI imaging could serve as a useful complementary tool for clinical diagnostics, which provides spatial information that contributes to the understanding of lipid signaling pathways and mechanisms involved in proximal tubule cell death associated with cisplatin treatment.

3.2 Dual internal standards with metals and molecules for MALDI imaging of kidney lipids

3.2.1 Overview

Matrix-assisted laser desorption ionization mass spectrometry imaging (MALDI MSI) provides a powerful tool for non-targeted analysis of drug[197, 198], protein[199, 200] lipid[122, 156], and metabolite[99, 201] distribution in biological tissues. In contrast to classic histological techniques, imaging of molecular species can be performed without chemical modification[38]. MALDI MSI has been employed for studying the distribution of endogenous lipids in tissue such as kidney[42, 178, 180, 202]. Comparison of biomolecules distribution in tissue sections is a powerful tool to discern between healthy and disease tissue states[202]. In the previous section of this work (3.1), MALDI MSI was employed to visualize the alterations in the distribution of kidney lipids induced by cisplatin treatment.

A major challenge still is the combination of MSI and quantification. The use of the image intensities for inter-tissue comparisons is difficult due to the variable influence of experimental and instrumental factors[42, 98, 181]. In addition, sample-originated matrix effects, including tissue surface microenvironment, result in inhomogeneous matrix-analyte crystal formation. Subsequently, non-linear variability in extraction, desorption and ionization of analytes across the tissue can be found[42].

Several normalization methods have been described for MALDI MSI to address the variability in signal intensity[69, 95, 98-105]. This includes the often used normalization to total ion current (TIC)[100, 106], with limited reliability[95, 98]. Also, normalization to matrix related peaks[99] was used for correction of uneven matrix thickness and crystallization. However, this method assumes that endogenous biomolecules respond evenly to changing matrix conditions, limiting the success of this approach as well[3]. Other methods implement normalization algorithms based on noise levels, and median signal intensity of the spectrum[98, 100]. However, the most promising approaches for MSI signal normalization seem to be those applying internal standards, enabling pixel-by-pixel correction of raw intensities and allowing reliable relative quantification[42].

Approaches that include the use of different internal standards have been reported for signal normalization of compounds in tissue as well as endogenous tissue components. Spray-deposition of levofloxacin as a reference standard was reported to normalize the distribution of the anti-TB drug, moxifloxacin[103]. Also, an inkjet printer was used to apply a deuterated analogue of acetyl-L-carnitine separately from the spray-coated matrix to study tissue-specific ionization differences[104]. With an ImagePrep station, standard peptides were applied as internal calibrants for normalizing imaging data sets from tryptic peptides[105]. Inkjet printing of non-endogenous lipids as internal standards was also reported to quantify lipids in nerve tissue[69].

In this respect, the optimization of matrix deposition is crucial because it affects the extraction and desorption of the analytes across the tissue surface, which in turn affects the resulting spectral quality and image reliability. Several studies reported the use of commercially available inkjet printers for quantitative applications in mass spectrometry imaging[69, 104, 203-205], because they provide a low cost technique for reproducible and homogenous matrix application.

In this section, a novel method for controlled and reproducible application of matrix and internal standards on kidney sections was developed, allowing normalization of lipid signals and intersample comparison of MALDI MSI data on relative quantitative basis. Two non-endogenous phospholipids, PE(15:0/15:0) and PC(21:0/21:0), were chosen as primary internal standards. An inkjet printer was used for automatic and homogenous application of matrix and internal standards[69, 204]. Samples were prepared simultaneously and matrix application was controlled using a secondary internal standard. For this purpose, a monoisotopic lanthanide salt was spiked to the ink and printed together with matrix and the internal standard lipids onto nitrocellulose (NC) membranes placed close to the tissue sections. Total metal content determination by inductively-coupled plasma mass spectrometry (ICP-MS) was performed to monitor the reproducibility of the matrix deposition.

The dual lipid-metal internal standard normalization method was evaluated by comparing the raw, TIC-normalized, and internal standard-normalized distributions and intensities of kidney lipids. The primary internal standards (non-endogenous phospholipids) were used to normalize lipid signals. With vehicle control tissues, we ensured that no isobaric species were apparent. To control the reproducibility and

homogeneity of matrix and internal standards printing, a spiked lanthanide was used as a secondary internal standard and quantified using ICP-MS, which is regarded here as orthogonal analytical method to MALDI MS.

3.2.2 Optimization of printing conditions and customized ink

Careful adjustment of the solvent composition was necessary to dissolve the internal lipid standards in the matrix solution. First, an attempt to use conventional ink as the dissolving medium was done; however, turbidity occurred because inks are sensitive to increased concentrations of dissolved salts. Also, strong background signals (polymeric pattern signals in the mass range 400-1200 m/z) that overlap with the mass range of lipids were detected (Figure 19-I). To optimize a customized solution, different MeOH:H_2O ratios (20:80, 50:50, and 70:30) were experimented, which resulted eventually, in complete solubility of the internal lipid standards and the most homogenous print coating. Higher MeOH content (70%) and slight heating of the microscope slides for 5 s before printing contributed to faster drying and clearly improved the homogeneity of the printed matrix coating (Figure 19-II and III).

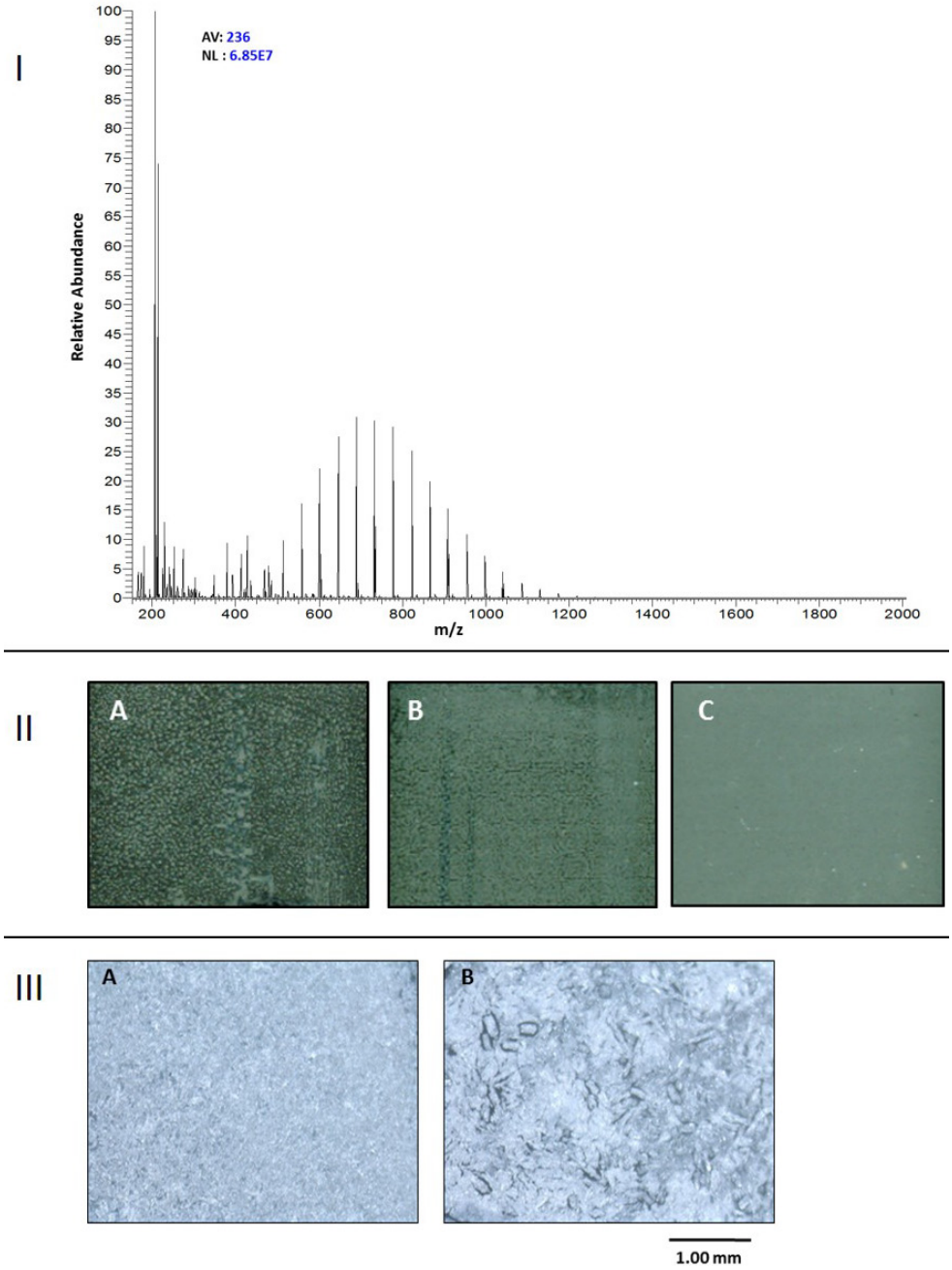

Figure 19. I) Mass spectrum showing background signals when colorless or yellow ink were used to dissolve DHB and the internal standards. II) Effect of increasing organic solvent composition on the homogeneity of the resulting printing output, where A, B, and C have 20%50% 70% MeOH, respectively. III) Digital microscope camera images showing matrix deposition after 5 printing cycles of ink solution (DHB = 120 mg mL^{-1} in 70% MeOH, 0.1% TFA). A) Pre-heating of the glass slide during 5s on a hot plate at 50 ˚C before each printing cycle, and B) at room temperature.

Control MALDI measurements showed that the printer-based method led to a much lower deposition compared to air-brush nebulizers, hence the concentration of DHB in

the matrix solution was higher (120 mg mL^{-1}) than that previously described for airbrush deposition[202] to avoid long deposition times (Figure 20).

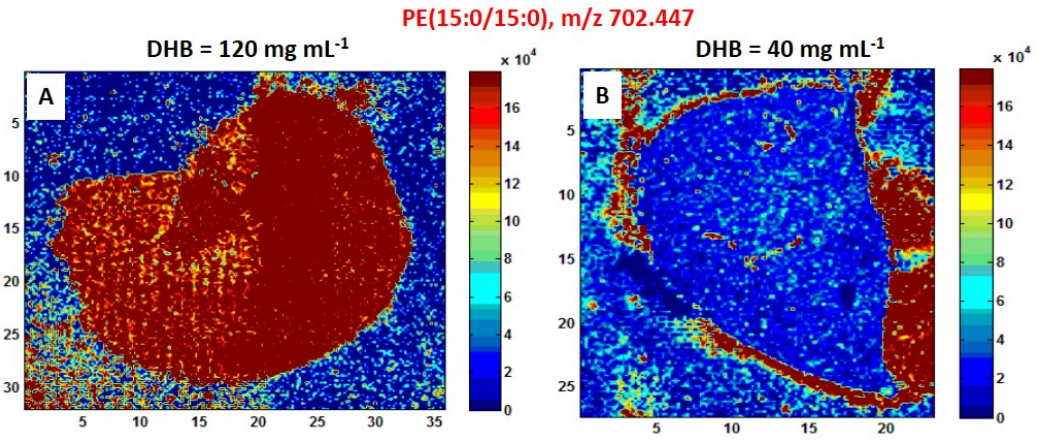

Figure 20. Effect of increasing DHB concentration on the ionization of the internal standard. Extracted ion images of $[M+K]^+$ of PE(15:0/15:0) internal standard at m/z 702.447 obtained for (A): inkjet printer at 120 mg mL^{-1} DHB, and (B): air-brush nebulizer at 40 mg mL^{-1} DHB. Both tissues had 30 deposition passes and the same internal standard concentration.

The effect of the number of printing cycles was monitored to optimize matrix and internal standards signal. A tissue section received 20 printing cycles on the left side and 30 on the right side, showed significant enhancement of the matrix and internal standards signals on the side receiving more printing cycles, while tissue lipids existing at different intensity levels showed adequate ionization (Figure 21).

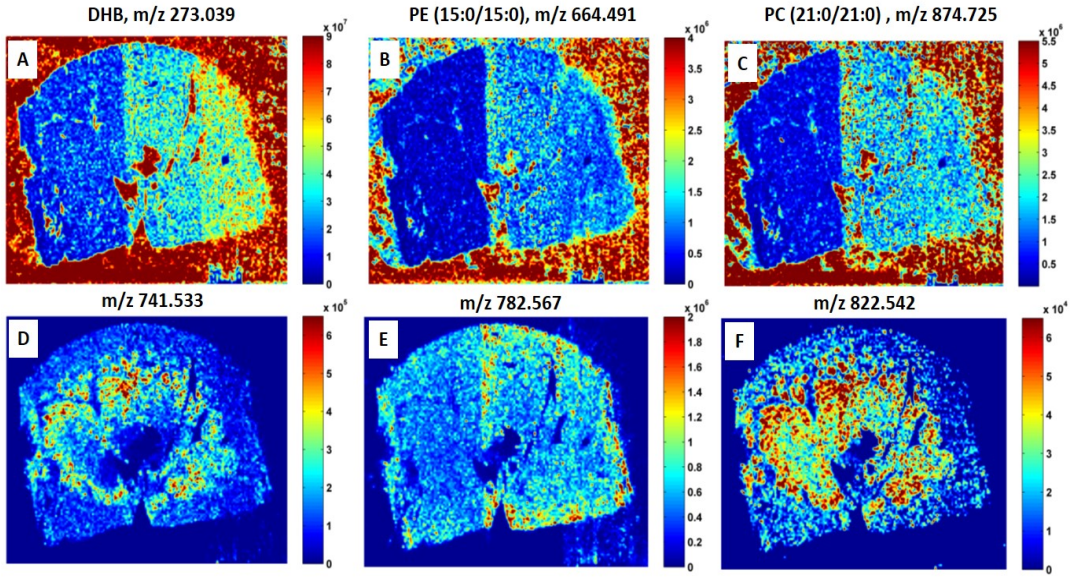

Figure 21. The effect of the number of printing cycles on the extracted ion images of a kidney tissue section with 20 printing cycles on the left side and 30 on the right side. (A) DHB, ($[2M-2H_2O]^+$ at m/z 273.039). (B) $[M+H]^+$ adduct of the PE (15:0/15:0) internal standard at m/z 664.491. (C) $[M+H]^+$ adduct of the PC (21:0/21:0) internal standard at m/z 874.725. (D-F) Tissue lipids at m/z 741.533, 782.567, and 822.542, respectively.

Printing more than 30 cycles did not improve ion abundance. Intensity of matrix and internal standards, PE (15:0/15:0) and PC (21:0/21:0), showed increasing signals only up to 30 printing cycles. On the other hand, tissue lipids showed minimal change and stable ionization (Figure 22). The quality of mass spectra obtained from a kidney tissue upon printing 30 cycles of the optimized solution mixture is given in Figure 23.

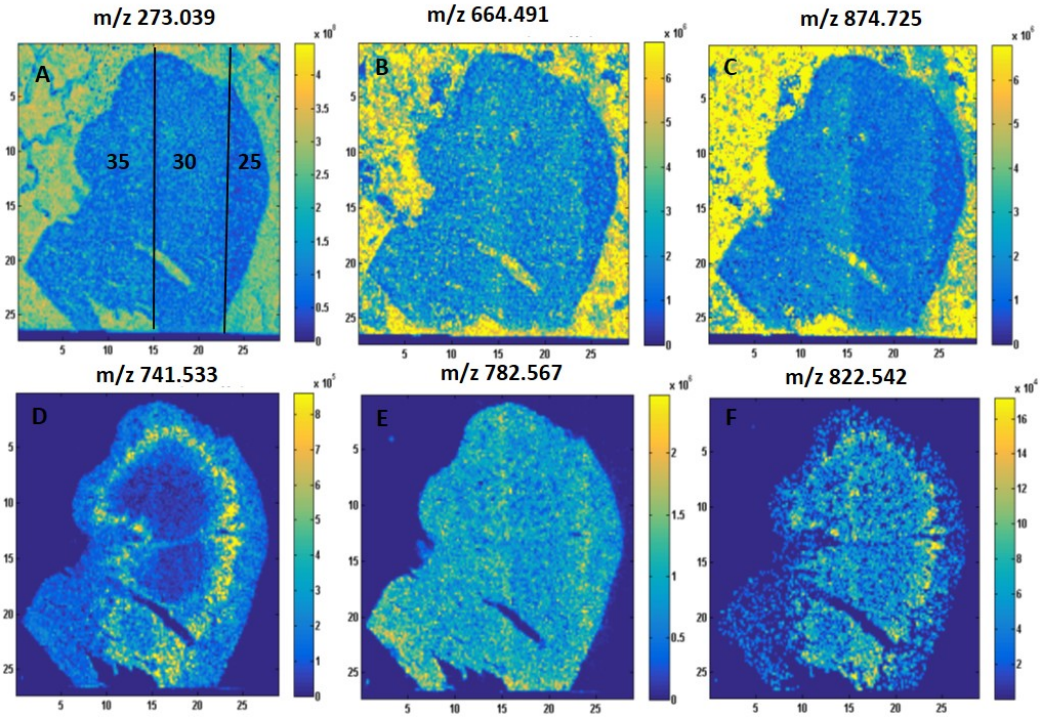

Figure 22. Kidney tissue section with 35 printing cycles on the left, 30 on the middle, and 25 on the right part. No enhancement of matrix and internal standard signal could be observed upon printing more than 30 cycles (A to C). (A) DHB, $[2M-2H_2O]^+$ (m/z 273.039). (B) $[M+H]^+$ adduct of the PE (15:0/15:0) internal standard (m/z 664.487). (C) $[M+H]^+$ adduct of the PC (21:0/21:0) internal standard (m/z 874.725). (D to F) Tissue lipids showing stable ionization at m/z 741.528, m/z 782.565, and m/z 822.542, respectively.

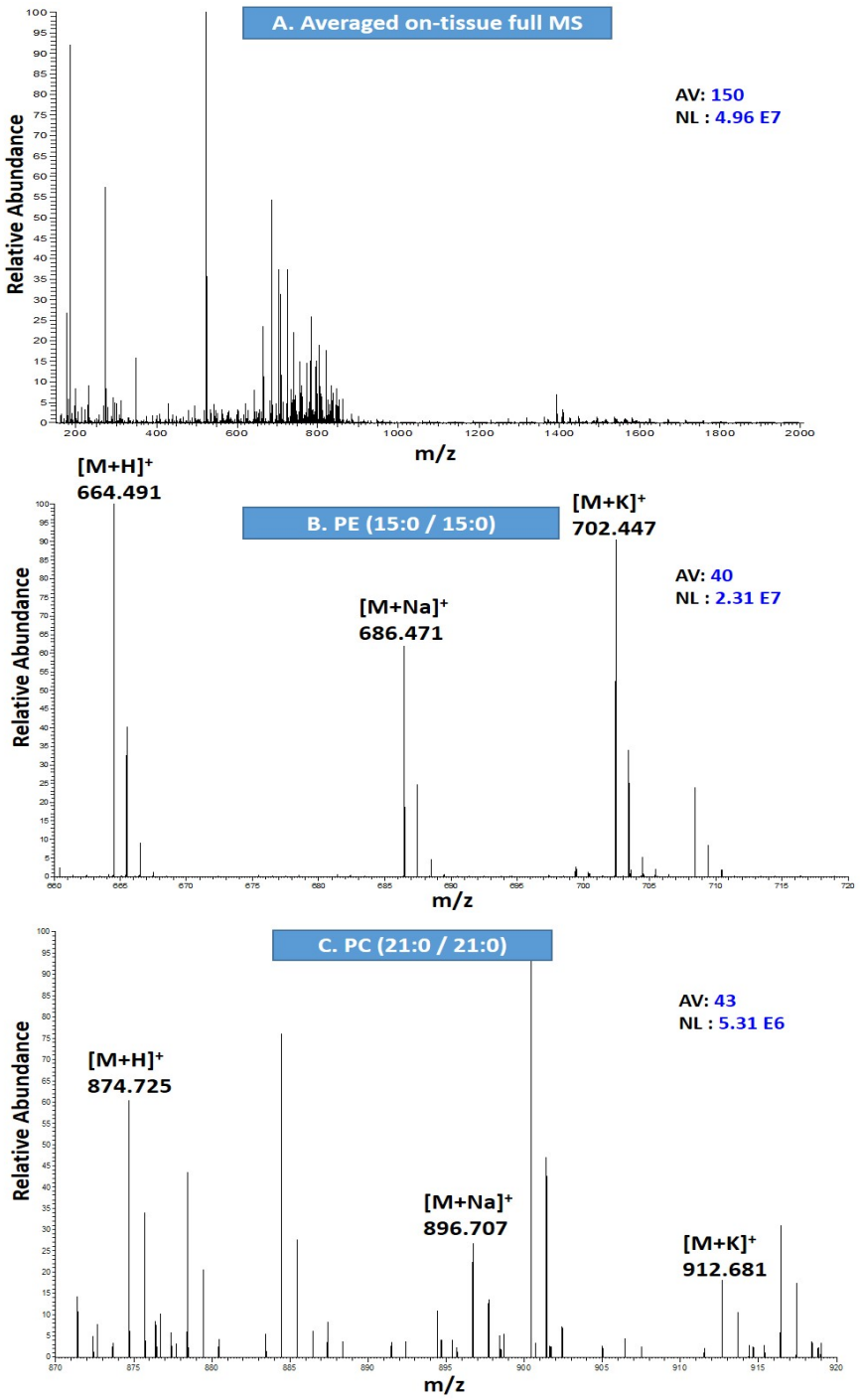

Figure 23. (A) Mass spectrum illustrates the spectral quality of a kidney tissue section printed with 30 cycles of matrix-internal standards mixture, tissue lipids are observed in the m/z range from 700-900. (B) H^+, Na^+ and K^+ adducts of the lipidic internal standard PE (15:0/15:0) at m/z 664.491, m/z 686.470 and m/z 702.447, respectively. (C) H^+ (m/z 874.725), Na^+ (m/z 896.707), and K^+ (m/z 912.680) adducts of the lipidic internal standard PC (21:0/21:0).

3.2.3 Reproducibility under optimized printing parameters and uniformity of internal standard on-tissue distribution

Reproducibility of the optimized printing method was assessed in control tissue replicates, showing comparable signal intensity of the matrix, endogenous lipids and adducts of both internal lipid standards (Figure 24). Ion images of H^+, Na^+, and K^+ adducts demonstrated the uniformity of on-tissue distribution of the printed internal standard lipids (Figure 25). Additionally, evaluation of the mean relative intensity in 3 Regions Of Interest (ROI) -each consisted of 125 pixels- in different locations of the tissue section in Figure 25 showed a RSD value <10% for H^+, Na^+, and K^+ adducts of both internal standards.

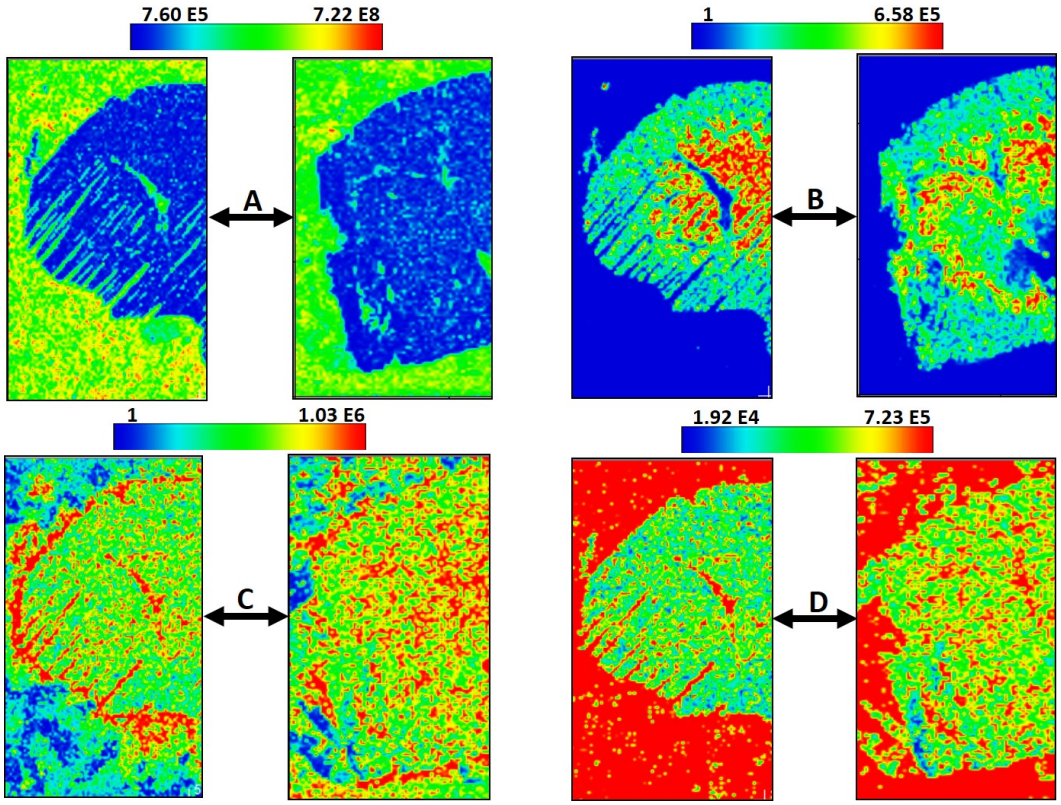

Figure 24. Reproducibility of MALDI images is demonstrated in two kidney tissue sections printed according to the optimized parameters. (A) DHB signal at m/z 273.039. (B) Endogenous lipid at m/z 741.533. (C) $[M+K]^+$ of the PE (15:0/15:0) internal standard at m/z 702.447. (D) $[M+Na]^+$ of the PC (21:0/21:0) internal standard at m/z 896.707.

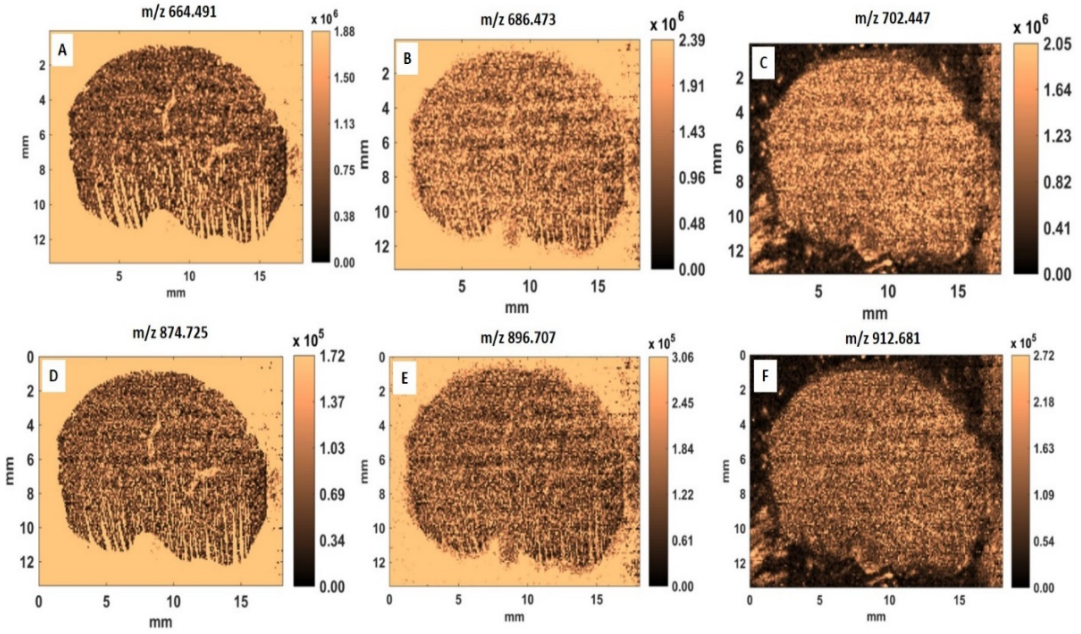

Figure 25. (A-C) Ion extracted images showing on-tissue distribution of H^+, Na^+, and K^+ adducts of IS PE (15:0/15:0) at m/z 664.491, 686.473, and 702.447, respectively. (D-F) Ion images showing on-tissue distribution of H^+, Na^+ and K^+ adducts of IS PC (21:0/21:0) at m/z 874.725, m/z 896.707 and m/z 912.681, respectively.

3.2.4 Proof of concept

Instrumental drifts

To assess the potential of the internal standards to correct for signal variability associated with instrumental drifts, an experiment simulating the effect of varying laser energy was performed. Figure 26 illustrates the extracted ion images, where two halves of a single tissue section printed with the matrix-internal standards mixture were analyzed using different laser energies. For the upper half of the tissue, the laser energy was set to 27 µJ, while for the lower half it was set to 40 µJ, the latter being the optimal experimental condition for ionization. As expected, this resulted in different ionization efficiencies for the endogenous lipids as seen in three lipid ions at m/z 741.533, m/z 782.567, and m/z 822.542, with lower ionization in the upper half (Figure 26A to C). Normalization of the endogenous lipids against signals of H^+ and K^+ adducts of the PC (21:0/21:0) internal standard led to comparable relative intensities in both halves (Figure 26D to I).

This proves that a homogenously applied internal standard corrects for instrumental factors affecting ionization. The results of internal standard normalization are depicted in Figure 26 for three endogenous lipids at varying intensity levels with m/z 782.567 > m/z 741.533 > m/z 822.542 (approximate intensity range of 1 to 2 E^6, 1.5 to 3 E^5, and 4 to 8 E^4, respectively). The normalized relative intensity of lipids showed different levels in the images normalized to H^+ and K^+ adducts of PC (21:0/21:0). This could be explained due to different on-tissue abundance of both internal standard adducts. Nevertheless, correction using relative intensity worked successfully in both cases.

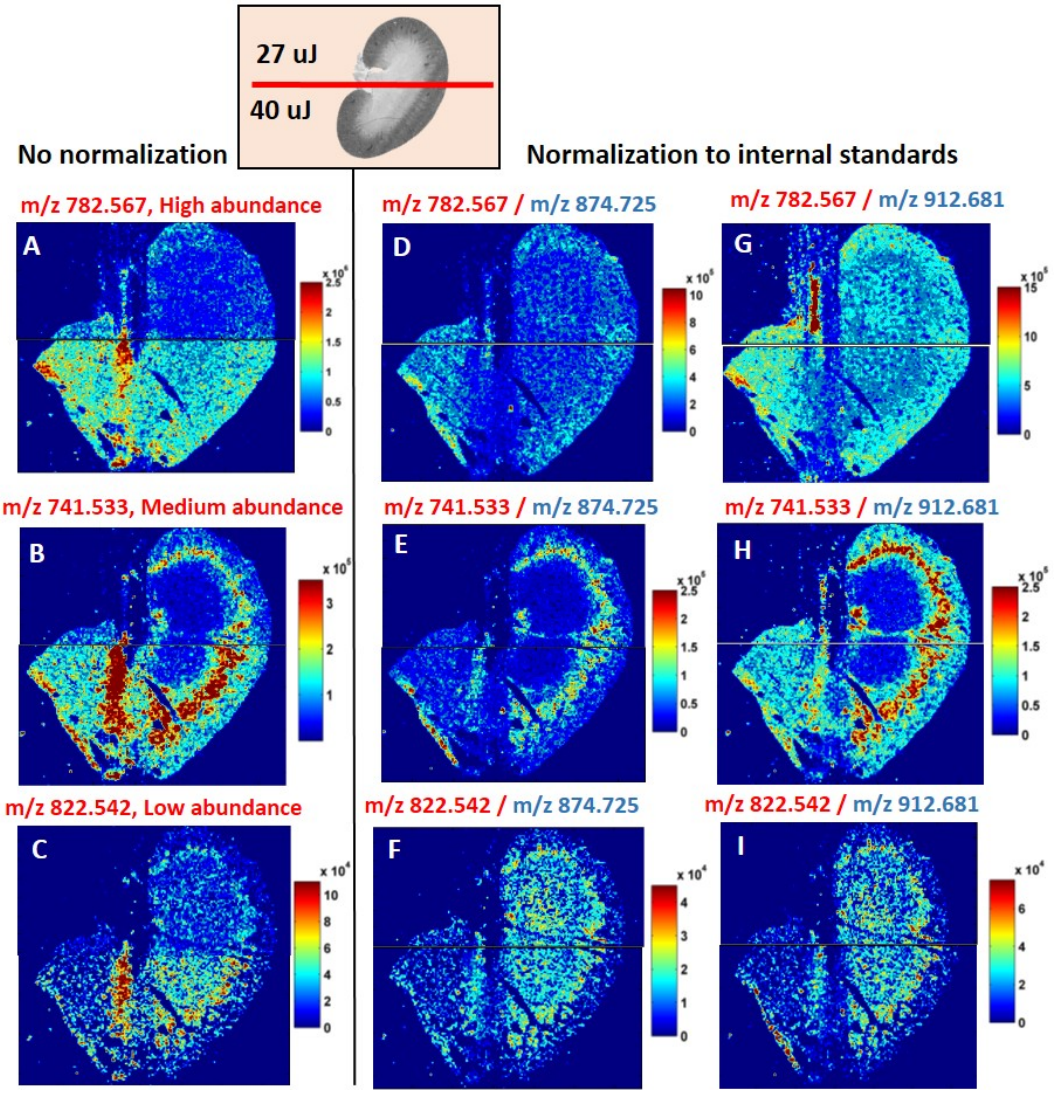

Figure 26. Extracted ion images show the effect of variation of laser energy on ionization. The upper half of the tissue was ablated at 27 µJ, and the lower half at 40 µJ. Tissue lipids (m/z 741.533, 782.567, and 822.542, respectively) are displayed, either unnormalized (A to C), or normalized to H^+ and K^+ adducts of PC (21:0/21:0) internal standard at m/z 874.725 (D to F) and m/z 912.681 (G to I), respectively.

Methodological drifts

The potential of internal standards to correct for signal variability originated from experimental inconsistency between measurements was evaluated. Different matrix-internal standard mixture depositions were used, and the effect on the endogenous lipids ionization profiles was checked, details are shown in Figure 27. A control tissue was printed with matrix-internal standards mixture, the left half receiving 30 cycles of printing, and the right one only 15. Then, each part of the tissue was analyzed separately. MALDI images showed that the endogenous lipids were differently affected by the change in matrix-internal standards amounts, where more abundant lipids (m/z 782.567) became enhanced with more printing passes, while lipids with medium and lower relative abundance (m/z 741.533, 822.542), showed little or no enhancement, with some signal suppression even being observed. Obviously, normalization to the internal standards did not correct for this variation (Figure 27).

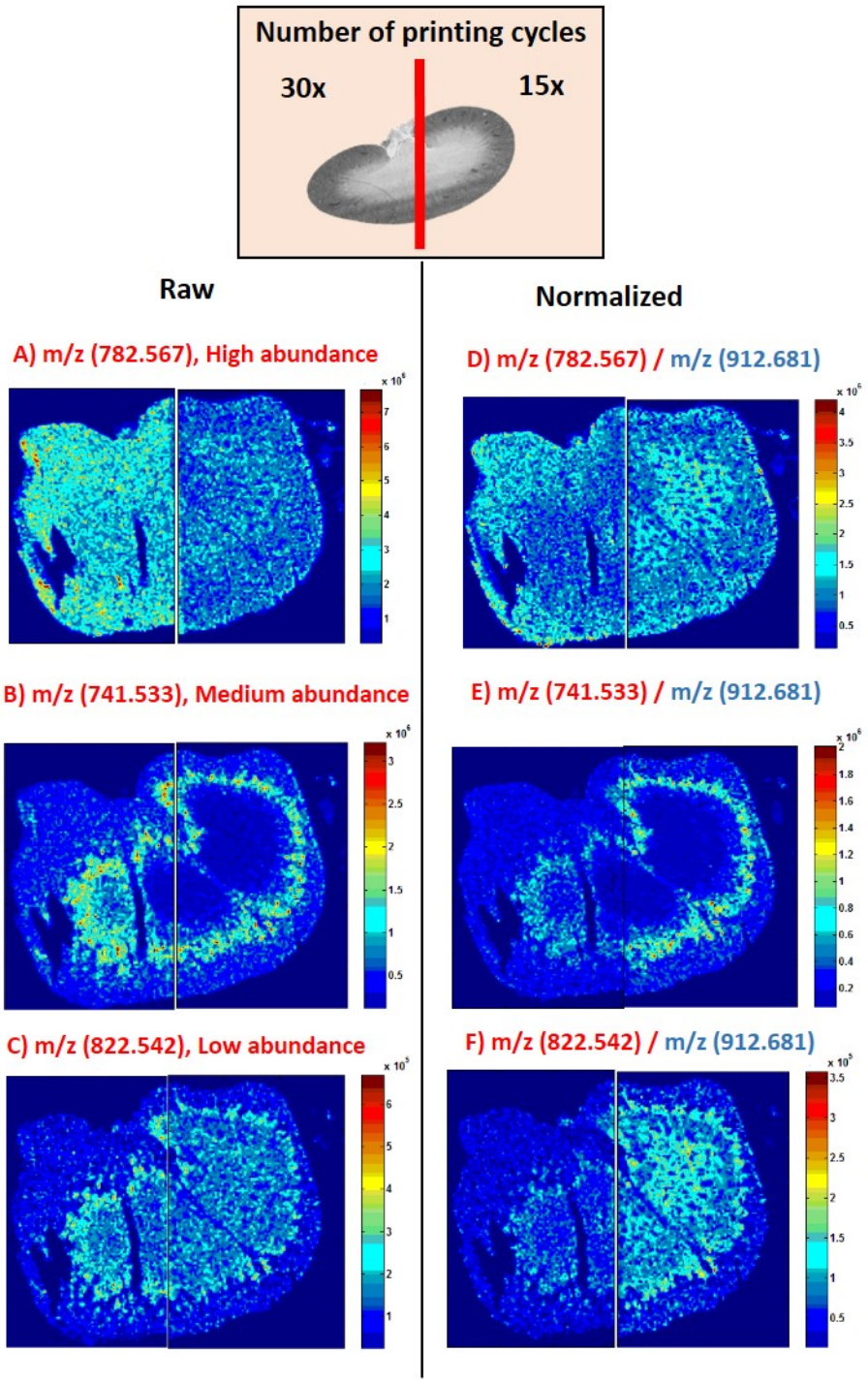

Figure 27. Color codes illustrate the effect of a proportional variation of matrix and internal standards amounts. Endogenous lipids with high, medium and low abundance are shown in panels A, B and C, respectively. Panels D, E and F show the same m/z images corrected by $[M+K]^+$ of PC internal standard, m/z 912.681.

Hence, a secondary internal standard was added to the mixture to control the printing reproducibility. Thulium (^{169}Tm) was spiked to the ink in a final concentration of 1 mg L^{-1}, and a NC membrane was fixed to the glass slide close to the tissue section, to be

printed in one experiment. Afterwards, membranes were collected, mineralized and analyzed by direct injection ICP-MS for absolute quantification of the metal deposited, which correlates to the absolute amount of matrix and internal standards. The amount of Tm in NC membranes in different experiments showed a mean value of 279 pg Tm per mg membrane with a relative standard deviation of 10-15%, as can be seen in Figure 28.

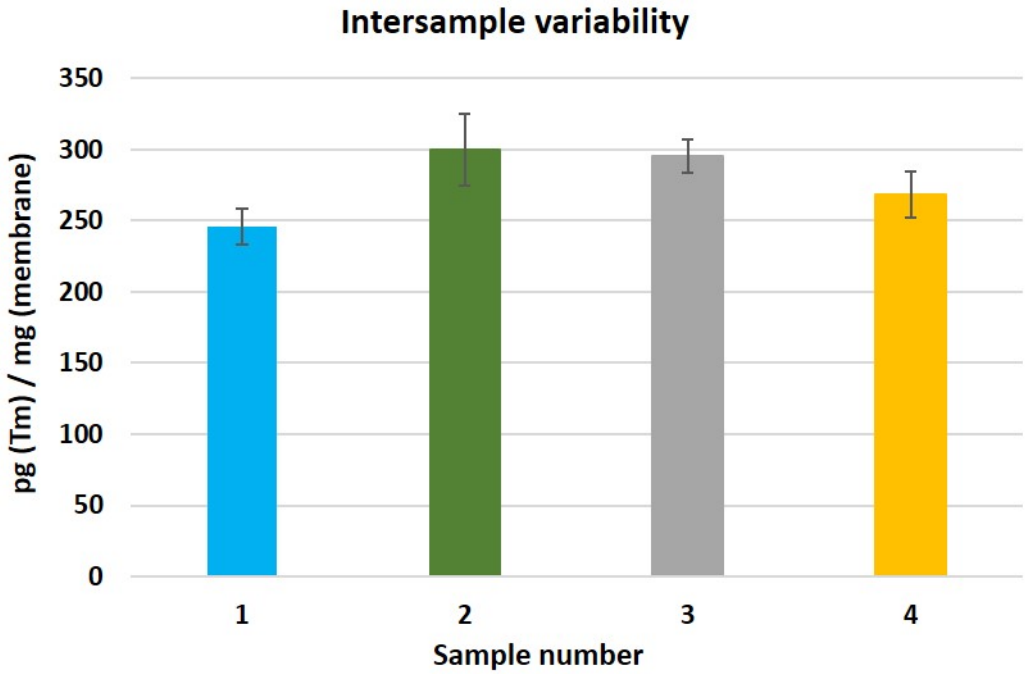

Figure 28. Metal amounts in mineralized membranes printed simultaneously with the tissues. Nitrocellulose membrane from each printing experiment weighed approx. 2-4 mg. Metal content in the different samples showed a mean value of 277 pg (Tm) / mg (membrane) with a RSD value of 11%. Error bars indicate the s.e.m where the mean value in each sample is calculated using 3 replicates.

In addition, LA-ICP-MS of NC membranes demonstrated the good homogeneity of metal distribution (Figure 29), where signal intensity showed RSD value of 2-4% between the different ablated lines within the membrane, which supports the results obtained on-tissue (Figure 25).

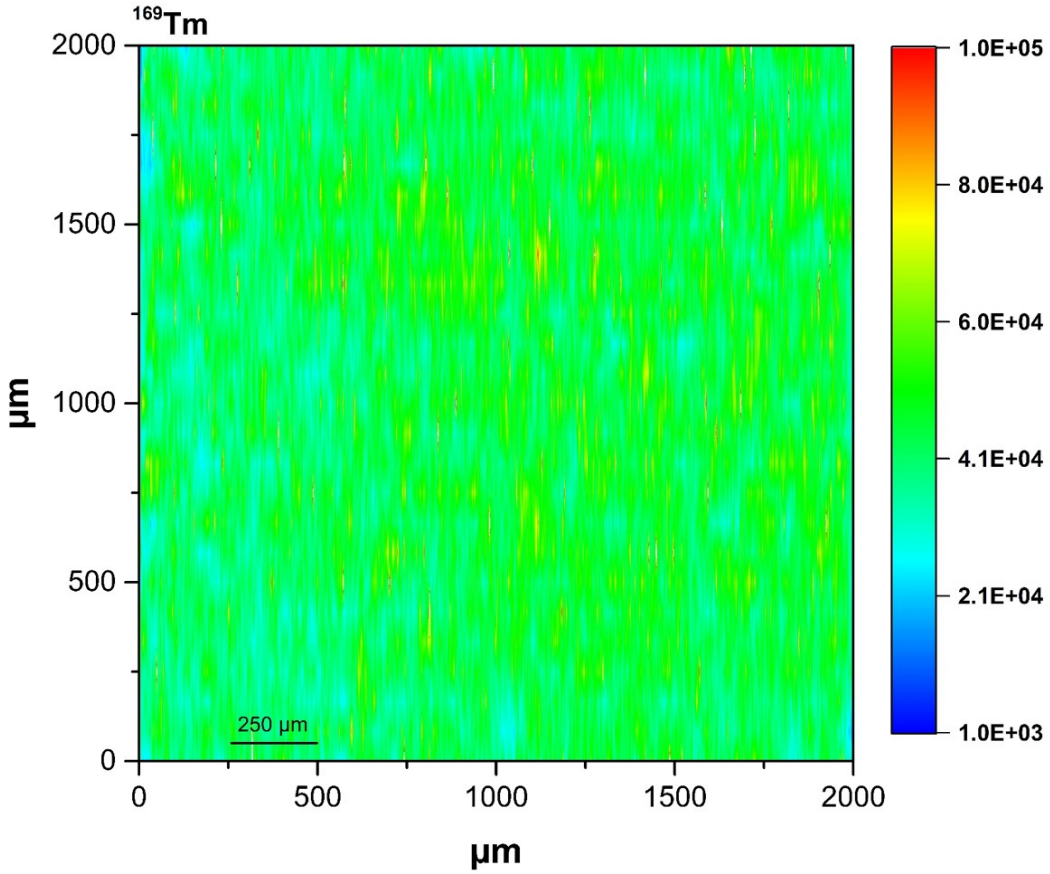

Figure 29. Intensity profile of ^{169}Tm using LA-ICP-MS of a 2 mm^2 area of a NC membrane, which received 30 printing cycles of the optimized matrix/internal standards mixture. RSD value of 2-4% was found between the different ablated lines within the membrane.

3.2.5 Application for intratissue or intrameasurement correction

Effect of the internal standard adduct type and chemical class

Next, the raw intensity of various lipid species was normalized to those of the different internal standards adducts, and the resulting images were compared to their TIC-normalized image. Figure 30 shows normalization of the raw intensities of m/z 760.587 ($[M+H]^+$ (PC (34:1), Δm=2.50 ppm) to the H^+, Na^+, and K^+ adducts of both PE(15:0/15:0) and PC(21:0/21:0) internal standards (Figure 30D to I), and TIC-normalization (Figure 30C). The optical tissue image showed several irregular locations on tissue surface caused by small folds or surface irregularity (arrows in Figure 30A). In general, higher ion abundance in the medulla relative to the cortex was visible in all normalized images. However, normalization to H^+ adducts of both internal standards (Figure 30D and G) preferentially showed higher intensity at locations of the artifacts, even when the overall relative intensity was not the highest, improving the correlation of MALDI image to optical image[206]. The corrections based on Na^+ and K^+ adducts of the internal standards showed the highest overall normalized intensity with less differentiation of the tissue folds (Figure 30E, F, H, I); the same holds true for the raw and the TIC-normalized images (Figure 30B and C). Hence, it would be preferable to normalize the intensity of a certain lipid adduct to an internal standard ion of the same lipid class and adduct type, considering the dependence of adduct formation on the lipid type and the abundance of Na^+/K^+ in the tissue microenvironment.

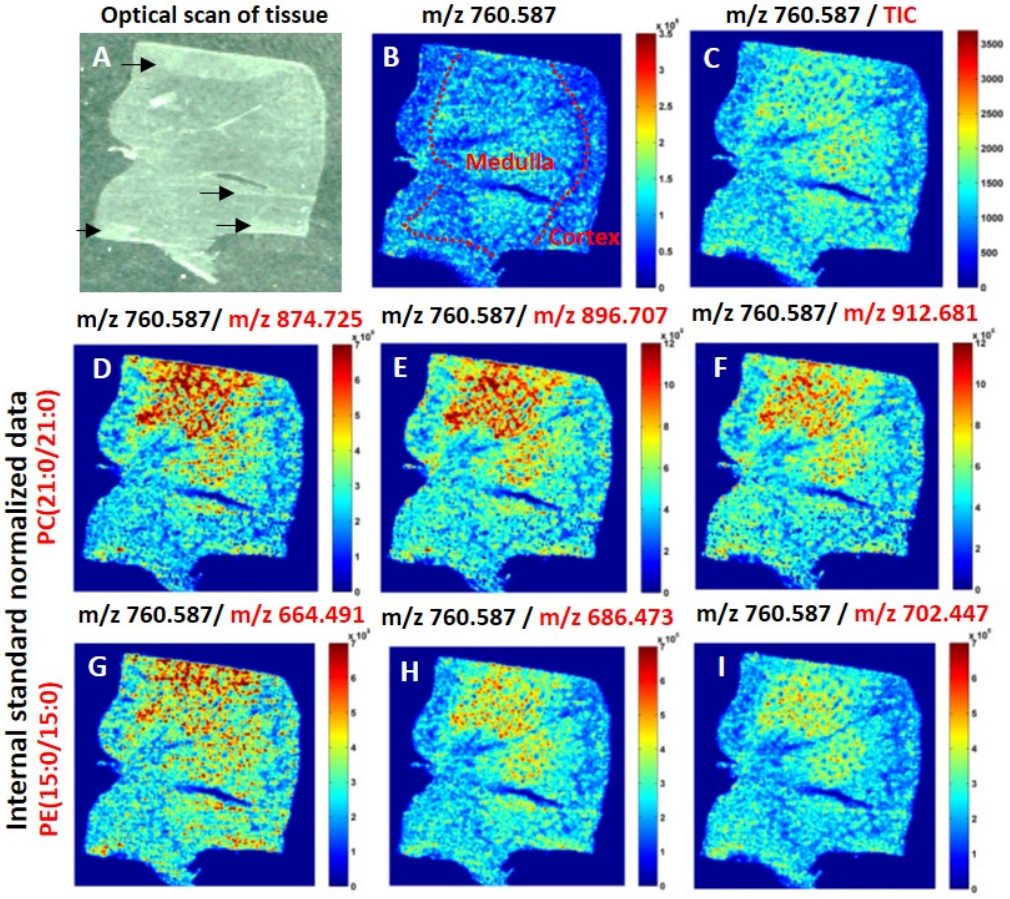

Figure 30. Effect of internal standard adduct type on the normalized images of $[M+H]^+$ of PC(34:1) at m/z 760.587. (A) Optical scan of the measured tissue. (B) Raw MALDI image. (C) TIC-normalized image. (D-F) Images normalized to $[M+H]^+$, $[M+Na]^+$, and $[M+K]^+$ of PE(15:0/15:0) at m/z 664.491, 686.473, and 702.447, respectively. (G-I) Normalized images to $[M+H]^+$, $[M+Na]^+$ and $[M+K]^+$ of PC(21:0/21:0) at m/z 874.725, 896.707 and 912.681, respectively.

Even for lipid classes unequal to the internal standards, the beneficial effect was still visible on comparing the raw, TIC-normalized, and internal standard-normalized ion images of m/z 909.547 (PI(38:4), $[M+Na]^+$, Δm=0.93 ppm) in the same tissue section (Figure 31). Images normalized to the different internal standard adducts showed the same qualitative tendency reflecting accurately tissue irregularities in the optical image, and presented clear improvement in comparison to the raw and TIC-normalized images (Figure 31).

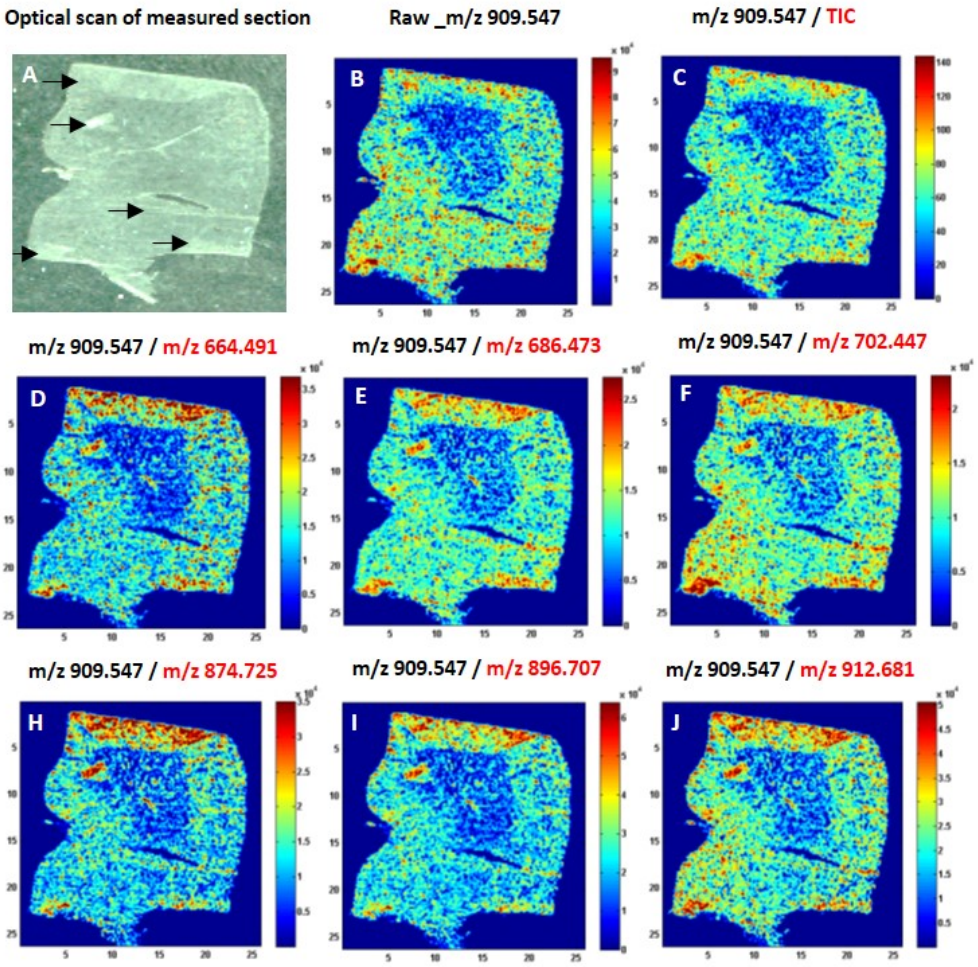

Figure 31. Improved reflection of tissue irregularities observed in internal standard normalized MALDI images for m/z 909.547 (PI(38:4), $[M+Na]^+$). (A) Optical scan of the measured tissue. (B) Raw MALDI image of m/z 909.547. (C) TIC-normalized image. (D to F) Normalized images of m/z 909.547 to $[M+H]^+$, $[M+Na]^+$ and $[M+K]^+$ of PE (15:0/15:0) at m/z 664.491, m/z 686.473, and m/z 702.447, respectively. (G to I) Normalized images of m/z 909.547 to $[M+H]^+$, $[M+Na]^+$ and $[M+K]^+$ of PC(21:0/21:0) at m/z 874.725, m/z 896.707 and m/z 912.681, respectively.

Additionally, the signal stability of different species was analyzed for more appropriate assessment of the internal standard normalization effect. Intensity analysis of $[PE(36:4)+K]^+$ at m/z 778.478 and $[PC(32:1)+Na]^+$ at m/z 754.536 in several locations in the tissue section, including tissue folds and different kidney regions (cortex and medulla), showed a particularly improved signal stability when normalization to an internal standard adduct of similar ion type was used (Figure 32); concluding adduct type as crucial for appropriate normalization.

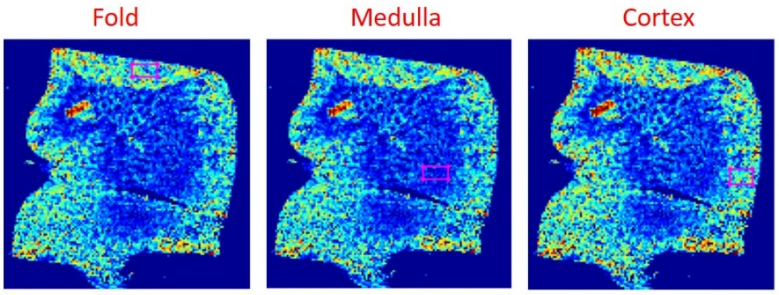

[PE(36:4)+K]+

	778.478	778.478/TIC	778.478/664.491	778.478/686.473	778.478/702.447	778.478/874.725	778.478/896.707	778.478/912.681
Fold								
avg	78951.38	122.81	39887.16	27795.82	22967.90	42253.25	64662.98	55277.57
stdev	21476.53	38.53	12911.01	7129.54	5775.75	13522.21	18286.00	14202.42
rsd	27.20	31.37	32.37	25.65	25.15	32.00	28.28	25.69
Medulla								
avg	41594.96	57.03	13294.88	10811.85	9380.80	12110.12	20591.45	19991.35
stdev	9525.90	14.52	3356.07	2042.76	1606.40	2538.37	3675.16	3455.46
rsd	22.90	25.46	25.24	18.89	17.12	20.96	17.85	17.28
Cortex								
avg	86864.65	131.96	34150.45	25822.16	24469.28	29607.06	53337.28	52443.89
stdev	18544.02	29.69	8884.57	4391.21	3884.72	7630.15	11291.18	9789.22
rsd	21.35	22.50	26.02	17.01	15.88	25.77	21.17	18.67

[PC(32:1)+Na]+

	754.536	754.536/TIC	754.536/664.491	754.536/686.473	754.536/702.447	754.536/874.725	754.536/896.707	754.536/912.681
Fold								
avg	45717.28	92.27	25176.95	19579.69	13582.36	26041.86	38597.79805	32665.08
stdev	11034.78	26.92	7553.80	4089.61	3174.74	7236.63	8409.485431	7509.60
rsd	24.14	29.18	30.00	20.89	23.37	27.79	21.79	22.99
Medulla								
avg	41224.18	52.12	10717.90	10754.05	8474.25	9319.13	19419.51	17340.52
stdev	8819.66	13.42	2936.73	1683.67	1521.63	2201.89	3237.85	3144.14
rsd	21.39	25.75	27.40	15.66	17.96	23.63	16.67	18.13
Cortex								
avg	43038.59	63.75	13740.25	12085.05	12047.11	14476.04	26131.57	26007.62
stdev	10909.54	14.15	3815.47	2589.03	3021.71	3659.00	5769.83	6230.95
rsd	25.35	22.20	27.77	21.42	25.08	25.28	22.08	23.96

Figure 32. Mean relative intensity calculated in different ROIs in the tissue section for m/z 778.478 and m/z 754.536 (marked in magenta: Fold, Medulla and Cortex, each ROI contains approx. 100 pixels). The tables show average, standard deviation and relative standard deviation for non-normalized, TIC-normalized and different internal standards adducts–normalized intensity at m/z 664.491, m/z 686.473, m/z 702.447, m/z 874.725, m/z 896.707 and m/z 912.681, corresponding to $[M+H]^+$, $[M+Na]^+$, $[M+K]^+$ for PE(15:0/15:0) and PC(21:0/21:0), respectively.

Structure and condition of the tissue

The internal standard-normalized MALDI image in the upper panel in Figure 33D demonstrated a clearer lipid distribution within the kidney structures in comparison to the raw image (Figure 33B). Normalization of m/z 758.570 (PC (34:2), $[M+H]^+$, Δm = 0.66 ppm) to H^+ adduct of PC at m/z 874.725 (Figure 33D) reflected the differential distribution in the inner medulla (IM), the inner and outer stripes of the outer medulla (OM), in addition to the cortex; as indicated in the H&E image (Figure 33A). This was also seen in the TIC-normalized image (Figure 33C).

Another tissue section shown in the lower panel in Figure 33 presented three slight folds at its upper-half, which could be seen in the optical image of the tissue (Figure 33E). The raw MALDI images of some lipids reflected this appearance (Figure 33I) while others did not (Figure 33F). In either cases, the internal standard-normalized images showed accurately the details of the surface irregularity (Figure 33H and K).

Raw and TIC-normalized images of m/z 524.371 (LPC(18:0), $[M+H]^+$, Δm = 0.19 ppm) missed the definition of tissue folds (Figure 33F and G). Normalization to the H^+ adduct of the PC(21:0/21:0) internal standard (Figure 33H) showed a superior image quality matching the optical image (Figure 33E). On the other hand, the raw image of m/z 796.526 (PC(34:2), $[M+K]^+$, Δm= 0.75 ppm) reflected the tissue folds (Figure 33I). Normalization to K^+ adduct of PC(21:0/21:0) maintained the actual state of the tissue (Figure 33K), and showed good agreement to the optical, raw and TIC-normalized images (Figure 33E, I, and J, respectively), confirming the actual condition of tissue section.

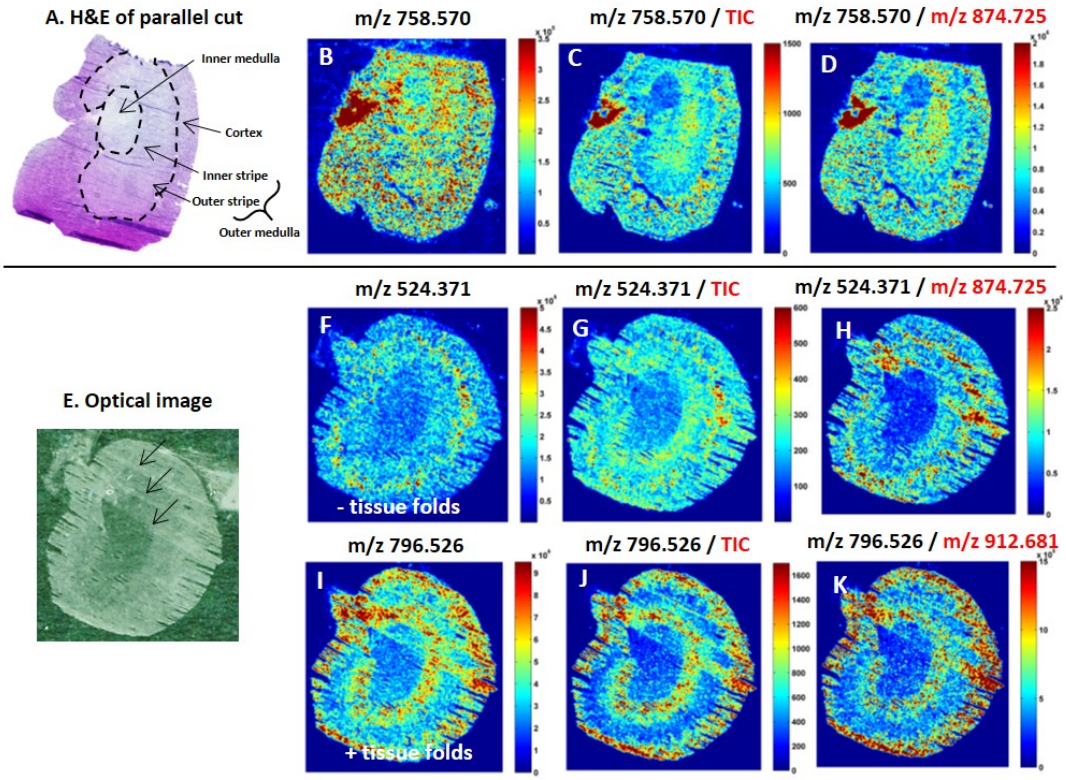

Figure 33. Upper panel: improved identification of renal structures upon correction to internal standard. (A) H&E image of a subsequent tissue cut. (B) Raw ion extracted image of m/z 758.570. (C and D) Normalized images of m/z 758.570 to TIC and $[M+H]^+$ of PC internal standard at m/z 874.725.

Lower panel: E. Optical image of another tissue. Arrows point at the exact position of tissue folds. MALDI images of raw (F and I), TIC-normalized (G and J) and PC(21:0/21:0)-normalized images (H and K) of tissue lipids at m/z 524.371 and m/z 796.526.

3.2.6 Application for intersample or intermeasurement correction

MALDI imaging data of control and cisplatin-treated kidney tissues printed side by side was used to show the role of normalization to internal standards in terms of intersample comparison. In the previous part of this work (chapter 3.1), differences in the distribution of renal lipids demonstrated the nephrotoxic effect caused by cisplatin treatment[202]. In analogy to the previous results, MALDI images of tissue lipids, this time normalized to internal standards, showed differences in lipids distribution between both groups. In addition, differences in abundance caused by variations of instrumental performance could be successfully corrected.

Figure 34 illustrates raw and normalized images of two tissue lipids (m/z 524.371 (LPC(18:0), $[M+H]^+$, Δm= 0.19 ppm) (Figure 34C to H), and m/z 800.461 (PE(38:7), $[M+K]^+$, Δm= 2.25 ppm) (Figure 34I to N)] with significant differences in distribution between control and cisplatin-treated tissues.

The raw image of m/z 524.371 in cisplatin kidney (Figure 34D) showed a homogenous distribution of the lipid in cortex and outer medulla with a higher local abundance at the corticomedullary junction; while control kidney (section taken at a different plane, Figure 34C) showed a less intense outer medulla and about 2-fold higher intensity of the lipid at the renal cortex. Normalization to $[M+H]^+$ of PC(21:0/21:0) at m/z 874.725 brought the lipid abundance in the two tissues closer showing an acceptable correlation and confirmed the distribution already indicated in the non-normalized images (Figure 34G and H). These findings agree well with TIC-normalized images of both tissues (Figure 34E and F), but internal standard-normalization ensures a more proper comparison of tissues with relative quantification purposes.

The non-normalized images of the other species at m/z 800.461 (Figure 34I and J) showed different distribution between control and cisplatin-treated tissue as well, where the lipid in the cisplatin-treated kidney (Figure 34J) was located mostly in the cortex. In the control tissue, a homogenous distribution of the lipid with higher abundance in comparison to the cortex of the cisplatin-treated kidney was seen (Figure 34I). Normalization to the $[M+K]^+$ of PE(15:0/15:0) at m/z 702.447 confirmed the lipid distribution and showed equal abundance level in the cortex and outer medulla of control tissue with respect to the cortex of cisplatin-treated tissue (Figure 34M and N), in analogy to the TIC-normalized images of both tissues (Figure 34K and L).

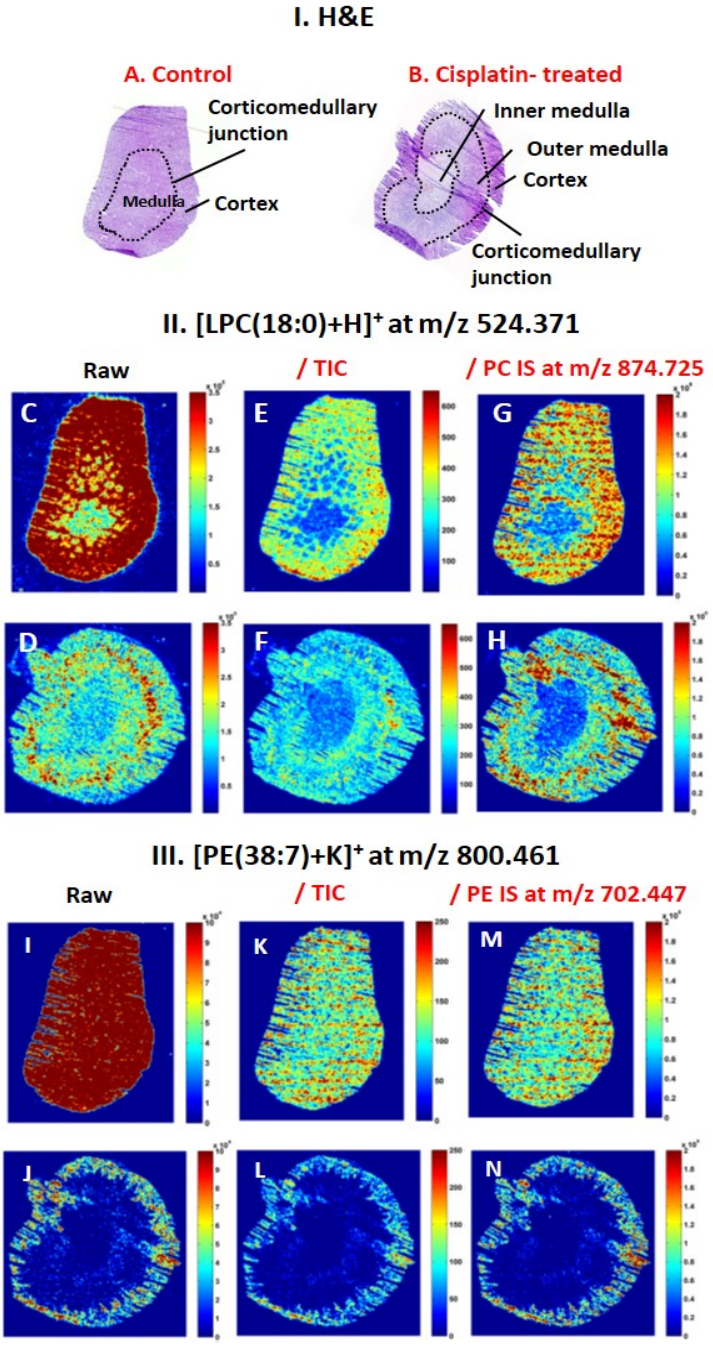

Figure 34. H&E optical images of kidney tissue sections of (A) control and (B) cisplatin-treated samples. Raw (C and D), TIC-normalized (E and F) and IS-normalized (with m/z 874.725) (G and H) MALDI images are shown for LPC(18:0) at m/z 524.371 in control and cisplatin kidney tissues, respectively. Raw (I and J), TIC-normalized (K and L), m/z 702.447 IS-normalized (M and N) MALDI images are displayed for PE(38:7) at m/z 800.461 in control and cisplatin kidney tissues, respectively.

Changes in the mean intensity of m/z 524.371 and m/z 800.461 in different locations of control and cisplatin-treated tissues before and after normalization are demonstrated in Figure 35, showing the clear impact of normalization on intensity fold-change calculation.

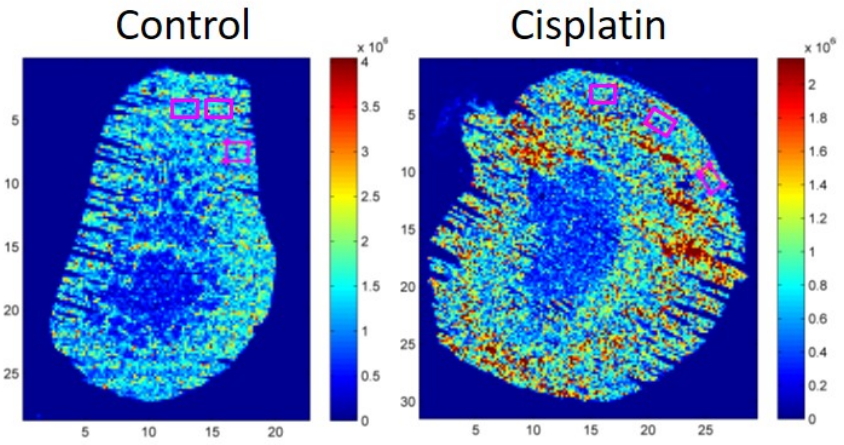

m/z 800.461	non-norm Mean I (%RSD)	m/z 702.447-norm Mean I (%RSD)
Control	176657.88 (4.39)	97035.81 (1.46)
Cisplatin	47384.10 (10.11)	76219.93 (6.41)
Control/Cisplatin	3.83	1.27

m/z 524.371	non-norm Mean I (%RSD)	m/z 874.725-norm Mean I (%RSD)
Control	517846.30 (4.23)	1384623.46 (4.58)
Cisplatin	160335.65 (7.24)	867727.87 (5.64)
Control/Cisplatin	3.23	1.60

Figure 35. Raw and IS-normalized mean intensity and %RSD over 3 ROIs (highlighted in the MALDI images in magenta, each ROI has 75 pixel) in the cortex of control and cisplatin-treated tissues for m/z 524.371 and m/z 800.461.

Intensity profiles of raw and TIC-normalized images of H^+, Na^+ and K^+ adducts of PC(32:1) (($[M+H]^+$ at m/z 732.553, Δm= 1.10 ppm), ($[M+Na]^+$ at m/z 754.536, Δm= 0.40 ppm), and ($[M+K]^+$ at m/z 770.509, Δm= 0.91 ppm)) are presented in Figure 36A to L. Additionally, internal standard-normalized images are shown in Figure 36M to R, where each of the H^+, Na^+, and K^+ adducts of PC(32:1) was normalized to its corresponding adduct of PC(21:0/21:0) at m/z 874.725, m/z 896.707 and m/z 912.681, respectively.

The raw images of the H^+, Na^+, and K^+ adducts of PC(32:1) in control kidney showed a homogenous tissue distribution (Figure 36A, C, E) in contrast to cisplatin-treated tissue (Figure 36B, D, F), where different local intensities (cortex > outer medulla > inner medulla) could be found for the lipid. The difference in distribution in both tissues was confirmed in TIC- and internal standard-normalized images. In addition, the false enhancement of intensity of H^+, Na^+, and K^+ adducts in control kidney (Figure 36A, C, E) in comparison to the same adducts in the cisplatin-treated tissue (Figure 36B, D, F), could be successfully corrected in the TIC- and internal standard-normalized images, similarly to Figure 34.

More importantly, raw and TIC-normalized images of both tissues showed different signal levels of the H^+, Na^+, and K^+ adducts of PC(32:1) (with $[M+Na]^+$> $[M+K]^+$> $[M+H]^+$) [raw: (control: Figure 36C > E > A) , (cisplatin: Figure 36D > F > B), TIC-normalized: (control: Figure 36I > K > G), (cisplatin: Figure 36J > L > H)]. However, internal standard-normalization showed in a unique manner that the lipid images for the three adduct types are almost identical not only for control (Figure 36M, O, Q), but also for cisplatin-treated tissue (Figure 36N, P, R). This suggests that normalization based on the same adduct type offers a more realistic and comparable intensity levels of the lipids in tissues.

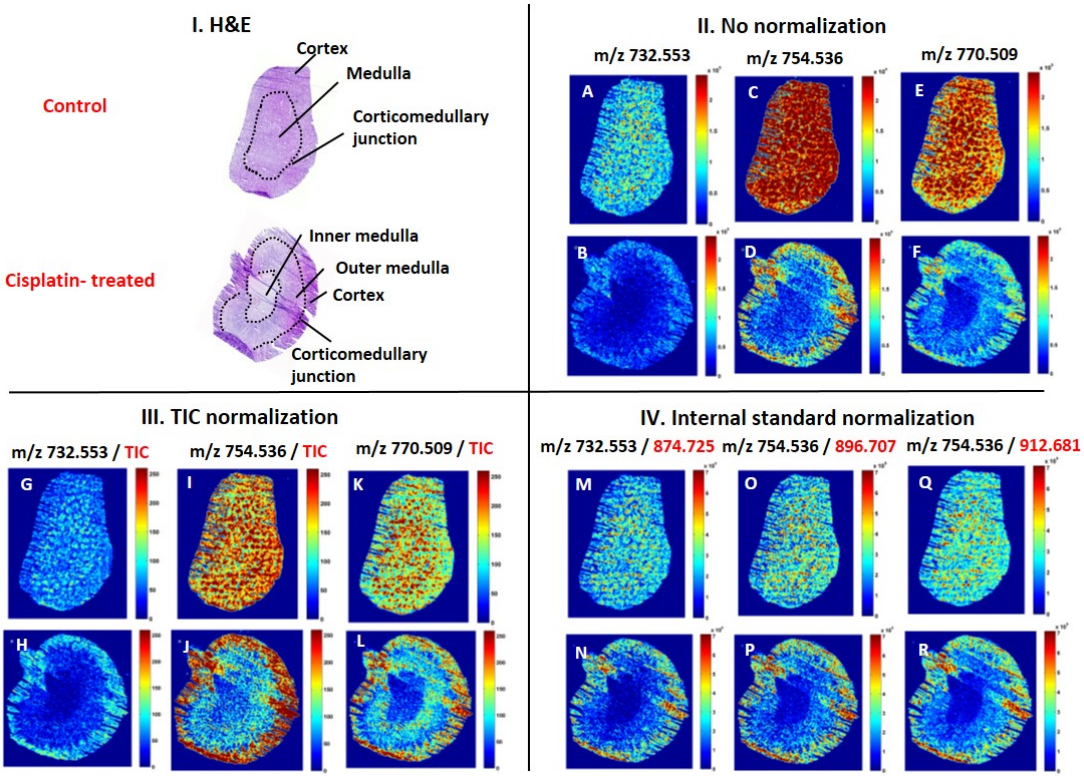

Figure 36. I. H&E optical images of subsequent kidney tissue section of control and cisplatin-treated samples. II. MALDI MSI data showing raw ions intensity (A to F). III. TIC-normalized ions intensity (G to L). IV. Internal standard-normalized ions intensity of H^+, Na^+ and K^+ adducts of PC(32:1) at m/z 732.553, m/z 754.536, m/z 770.509 , respectively (M to R).

3.2.7 Conclusion and outlook

An accurate, robust and reproducible method for controlled automatic printing of matrix and dual internal standards was developed, to normalize MALDI MSI data of kidney lipids. Reproducibility and homogeneity of matrix and internal standards deposition were demonstrated, this being controlled with a secondary internal metal standard spiked to the printing mixture and analyzed by ICP-MS. Normalization to the primary internal lipid standards offered excellent correction results with respect to possible variability of laser energy deposition observed in lengthy MALDI MSI tissue measurements. Optimum results were obtained upon normalizing a specific lipid adduct to internal standard adduct of a similar ion type and chemical class.

The method was successfully applied to normalize ion intensities of kidney lipids in control and cisplatin-treated rats allowing improved correlation of relative lipids abundance in both groups. Our results highlight the importance of controlled

homogenous matrix-internal standards application for reliable relative quantification of endogenous species in imaging studies. For intersample assessment of lipids abundances, comparisons based on normalizing the intensity of the lipid adduct of interest to the intensity of internal standard adduct of the same type are highly recommended. In addition, we recommend considering normalized intensities of different adducts of the same lipid species, where possible, as this draws a realistic view of the species relative abundance. We also foresee the use of multimolecular internal lipid standards extended to a wider range of lipid classes to be of great potential for MALDI imaging of tissue lipids, enabling improved pixel-based normalization of different lipids classes simultaneously.

4 Materials and methods

Table 3. Analytical instruments and equipment

Instrument type	**Model**	**Manufacturer**
MALDI LTQ orbitrap	MALDI LTQ Orbitrap XL™	Thermo Scientific, San José, CA, USA
Sector field ICP-MS	Element XR	Thermo Fisher Scientific, Germany
Nebulizer	MicroMist	Glass Expansion, Melbourne, Australia
Laser ablation system (LA)	UP-213	ESI, Portland, USA
Air brush	Aztek® A4709 Airbrush Set	The Testor Corp., USA
Balance	Sartorius CP225D	Sartorius
Inkjet printer	Pixma iP7250	Canon, Germany
Microscope	inverted IX70 microscope	Olympus, Hamburg, Germany
Digital microscope camera	dnt® USB microscope (5 Mega Pixels, maximum Magnification Ratio ca. 300x)	DigiMicro Profi, Germany
Cryostat	HM525 NX	Thermo Fisher Scientific,

Instrument type	Model	Manufacturer
Non-conductive glass slides	Superfrost Plus	Thermo Fisher Scientific, Braunschweig, Germany
MALDI target sample plate	Sample Plate Kit (P/N 97155-62033)	Thermo Scientific, San José, CA, USA
Scanner	HP Scanjet G4050 - Fotoscanner	HP Development Company, Germany
Nitrocellulose membranes	Protran® BA85	Whatman® , Dassel, Germany

4.1 Lipid imaging by MALDI LTQ Orbitrap mass spectrometry in kidney sections under cisplatin treatment

4.1.1 Chemicals and reagents

Solutions were prepared using ultrapure water (Milli-Q water purification system, Millipore, Bedford, MA). MALDI matrices (2,5-dihydroxybenzoic acid (DHB) and α-cyano-4-hydroxycinnamic acid (α-CHCA)), methanol (MeOH), acetonitrile (ACN) and trifluoroacetic acid (TFA) were purchased from Sigma-Aldrich (Steinheim, Germany). Cisplatin was obtained from Pharmacia Nostrum S.A. (Madrid, Spain) and was dissolved in 0.9% NaCl solution (Braun Medical S.A, Barcelona, Spain) for administration. Purchased chemicals were used without further purification.

4.1.2 Animal treatment and tissue preparation

Animals were treated at the laboratories of the Health Research Institute Gregorio Marañón hospital (Madrid, Spain). Experiments were approved by the hospital committee of ethics on animal experimentation (EAEC). Animals were cared for following applicable legal regulations in the European Directive 2010/63/UE on the protection of animals used for experimentation and other scientific purposes.

As previously described in [202], two groups of 7 week old female Wistar rats (Criffa, Barcelona, Spain), were kept under controlled conditions of light (12-h light/dark cycle), humidity, and temperature with food and water. Daily intraperitoneal injection (i.p.) of control and cisplatin-treated groups was carried out[175, 207]. Cisplatin was dissolved in 0.9% NaCl and administered at 5 mg kg^{-1} body weight in a single dose, while control group received only 0.9% NaCl. Animals were sacrificed after five days of treatment. Kidneys were perfused in ice-cold saline, shock frozen in liquid nitrogen, and stored at -80 °C. Cryosectioning (Thermo Fisher Scientific, HM525 NX) of the frozen kidneys to obtain 10 um sections was carried out. Non-conductive glass slides (Superfrost plus, Thermo Fisher Scientific, Braunschweig, Germany) were used for mounting of tissue sections[208]. The prepared sections were stored at -80 °C. Before matrix was applied, samples were taken out of the freezer to a desiccator where they were allowed to equilibrate to room temperature for 30 minutes, then optical images of the tissues were kept for reference.

4.1.3 Histological hematoxylin and eosin staining

Parallel sagittal sections of rat kidneys (5 µm) were stained with hematoxylin and eosin ((HE, Sigma-Aldrich, St. Louis, MO). Optical images of the stained samples at 20x magnification were for histological examination using an inverted Olympus IX70.

4.1.4 MALDI matrices

For positive ion mode MALDI lipid imaging, different concentrations of α-CHCA and DHB were tested in control vehicle kidney sections (Table 4).

Table 4. Name, concentrations, solvents used, and structures of matrices tested for optimization in MALDI MSI tissue measurements.

Matrix	Concentration (mg $mL^{-1)}$	Solvent	Structure
DHB	20, 40, 60	70% MeOH, 0.1% TFA	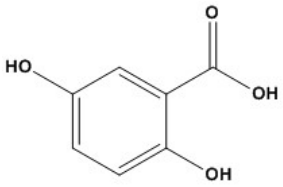
α-CHCA	10, 20	60% ACN, 0.1% TFA	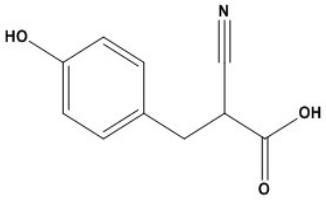

4.1.5 Matrix application

An in-house airbrush was used at a flow rate of 350 µL min^{-1} (measured with iPrOH). The airbrush was held at 20 cm distance to the target slide in a fume hood using a stand clamp. For calibration, the spray controller was adjusted to a spray cone of 1.5 cm diameter at 1.85 bar of the argon gas pressure (Figure 37). The airbrush was used to apply 10–35 cycles of matrix aerosol. Each spray cycle lasts for 20–40 s, followed by drying time for 20 or 40 s for DHB and CHCA, respectively.

During optimization of matrix deposition, tissues were partially covered with paper, as required, for the application of different deposition cycles within each tissue section.

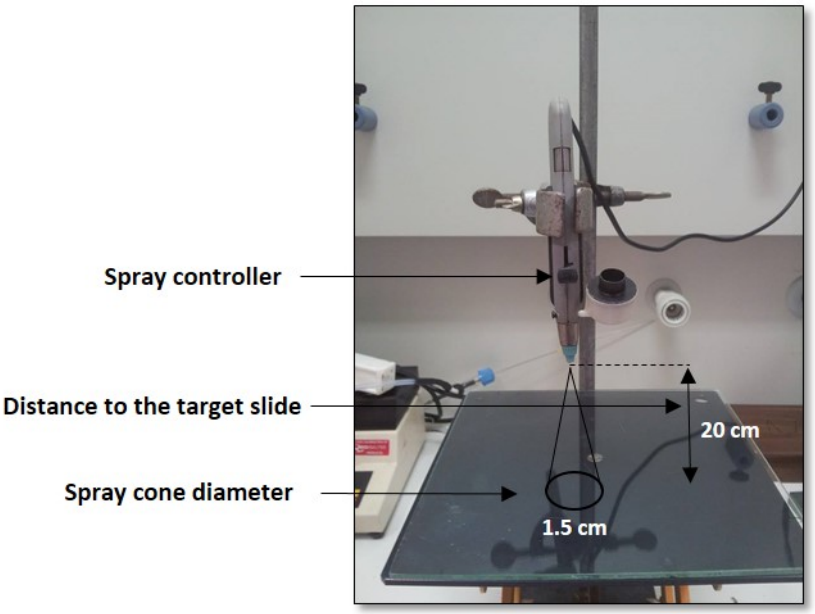

Figure 37. Airbrush used for matrix application showing functional parts used for its calibration.

4.1.6 **Instrumentation**

All MALDI MSI measurements and direct on-tissue MS/MS analysis in this thesis were carried out on a hybrid linear ion trap/orbitrap mass spectrometer fitted with a MALDI ion source that operates at intermediate pressure (MALDI LTQ Orbitrap XL, Thermo Fisher Scientific, Bremen, Germany). Instrument was calibrated using ProteoMass^{TM} MALDI Calibration Kit for LTQ XL^{TM} and LTQ Hybrids (Sigma Aldrich, St. Louis, USA). Automatic gain control of the LTQ XL (AGC) was turned on during the imaging experiments, and the nitrogen laser (337 nm, 3 ns, 60 Hz, (LTB, Berlin, Germany)) was tuned manually to obtain 10-15 laser shots per pixel on tissue (typically adjusted to: 20 µJ for CHCA, 40 µJ for DHB). Tissues were scanned in a horizontal raster mode with a lateral resolution between 100-500 µm in a meandering pattern with a laser spot diameter of 80 × 60 µm. Full-scan mass spectra were collected in positive ion mode averaging 2 microscans per step at m/z 150–2000 Da mass range. The mass resolving power was set to 60 000 on the FT MS analyzer.

On-tissue MS/MS experiments were performed in the ion trap by collision-induced dissociation (CID) at 35% energy to confirm the identification of major lipids based on neutral losses and characteristic fragments of the head group.

Xcalibur and ImageQuest software (Thermo Scientific, Germany) were used to analyze the data and create MALDI MSI images, which were extracted with a 0.005 Da tolerance and normalized against total ion count (TIC).

4.1.7 Molecular identification and nomenclature of tissue lipids

Identification of lipids was done based on accurate mass assignment of the precursor ion using the exact mass search in LipidMaps[209] with a mass window of 5 ppm. Manual interpretation of fragmentation patterns from MS/MS experiments was performed with the aid of LipidMaps tools. According to LipidMaps, lipids were assigned as follows:

Glycerophospholipids [PC, PE, PI, PG, lyso-PC (LPC)], species are followed by X:Y, where X is the total length of the acyl chains and Y represents the total number of double bonds. Sphingolipids (Cer and SM), species are designated by W:Z, where W is the total length of the acyl chain bound to the sphingosine, and Z is the amount of the chain double bonds. “O-” and “P-” designate alkyl ether linkage and (1Z)-alkenyl ether, respectively; while in sphingolipids, “h”, “d” and “t” indicate hydroxy, 1,3-dihydroxy and 1,3,4-trihydroxy, respectively, long chain bases.

4.2 Dual internal standards with metals and molecules for MALDI imaging of kidney lipids

4.2.1 Chemicals

Standard phospholipids, 1,2-dipentadecanoyl-sn-glycero-3-phosphoethanolamine (PE (15:0/15:0)) and 1,2-diheneicosanoyl-sn-glycero-3-phosphocholine (PC(21:0/21:0)) were purchased from Avanti Polar Lipids Inc. Solutions were prepared using ultrapure water (Milli-Q water purification system, Millipore, Bedford, MA). Chloroform ($CHCl_3$), methanol (MeOH) and trifluoroacetic acid (TFA) were purchased from Carl Roth GmbH + Co. KG (Karlsruhe, Germany). MALDI matrix, 2,5-dihydroxybenzoic acid (DHB) was purchased from Sigma-Aldrich (Steinheim, Germany). For ICP-MS analysis, single-element (^{141}Pr (Pr_6O_{11}, in 2%HNO_3) and ^{169}Tm ($TmCl_3$, in 2%HNO_3)) and multi-element standard solution for ICP and nitric acid (ultraquality, 69%) were obtained from Carl Roth, Germany. Purchased chemicals were used without further purification.

4.2.2 Animals treatment and tissue preparation

Control and cisplatin-treated 7 weeks old Wistar rats were obtained from the laboratories of the Instituto de Investigación Sanitaria Gregorio Marañón (IISGM, Madrid, Spain) following the same protocol described previously in this work[175, 202, 207]. Frozen kidney tissues from control and cisplatin-treated groups were cryosectioned (Thermo Fisher Scientific, HM525 NX) to produce 10 µm sections, which were mounted on non-conductive glass slides (Superfrost plus, Thermo Fisher Scientific, Braunschweig, Germany) and stored at -80 °C until further use. Before printing, tissue sections were taken out of the freezer to a desiccator where they were allowed to stand for 30 minutes. Optical scans of the samples were kept for reference (HP Scanjet G4050 - Fotoscanner). In addition, parallel 5 µm saggital sections were stained with hematoxylin and eosin (HE, Sigma-Aldrich, St. Louis, MO) and examined with 20x magnification using an inverted IX70 microscope (Olympus, Hamburg, Germany).

4.2.3 Matrix- internal standards mixture preparation

The printing mixture included DHB as MALDI matrix (120 mg mL^{-1} in 70% MeOH, 0.1% TFA), in addition to two non-endogenous phospholipids as primary lipidic internal standards (Table 5), PC (21:0/21:0) and PE (15:0/15:0) in a final concentration of 300 mg L^{-1}, and a monoisotopic lanthanide, thulium (^{169}Tm) in a final concentration of 1 mg L^{-1} as a secondary internal standard. Freshly prepared matrix-internal standards mixture was used for each printing experiment.

Each of PC (21:0/21:0) and PE (51:0/51:0) was prepared separately in 6000 mg L^{-1} stock solution in Chloroform : Methanol: Water in the ratio (C:M:W → 65:40:8). Stability of the lipidic standards was controlled by MALDI spot measurements to screen for decomposition. Lipids stocks were consumed over a maximum of 1-month interval.

Table 5. Structure, chemical name, molecular formula, and exact mass of PE (15:0/15:0) and PC (21:0/21:0).

PE (15:0/15:0) 1,2-dipentadecanoyl-sn-glycero-3-phosphoethanolamine Molecular formula: $C_{35}H_{70}NO_8P$ Exact mass: 663.484 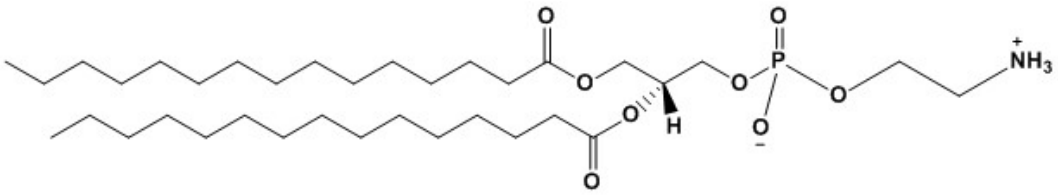
PC (21:0/21:0) 1,2-diheneicosanoyl-sn-glycero-3-phosphocholine Molecular formula: $C_{50}H_{100}NO_8P$ Exact mass: 873.719 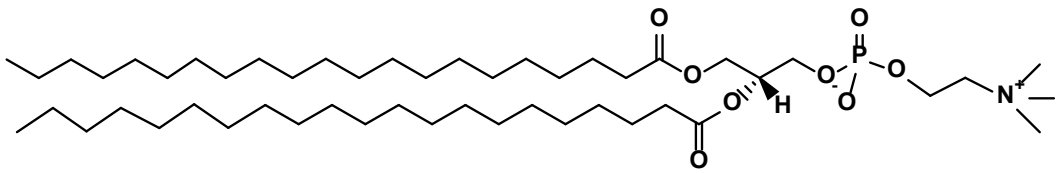

4.2.4 Inkjet printing of matrix-internal standards mixture

The mixture containing the matrix and the internal standards was applied to the tissue sections using a conventional inkjet desktop printer (Pixma iP7250, Canon, Germany). As previously described in [204, 205], the customized ink (matrix-internal standards mixture) was fed to empty cartridges using a syringe. Settings for disk printing were selected and the CD-tray holder was modified to adapt two glass slides, which were passed through the printer for 30 times, each corresponds to a printing cycle. Print quality was set to ‘’high’’.

To equilibrate the printer, 10 sheets of A4 papers were printed. Glass slides were heated briefly for 5 s at 45 C° before each printing cycle, the quality of printing was monitored visually using a digital microscope camera (dnt® DigiMicro Profi, Germany).

4.2.5 MALDI MSI measurements

MALDI LTQ Orbitrap XL™ (Thermo Scientific, Germany) was used for high resolution MSI analysis. Laser energy was manually tuned to obtain 10-15 laser shots per pixel on tissue. Tissues were scanned in a horizontal raster mode with a lateral resolution of 100 µm in a meandering pattern with a laser beam size of 80×60 µm. Full scan positive ion mass spectra were registered averaging 2 microscans per step at m/z 150–2000 Da mass range, and a mass resolution of 60000 was used on the FT MS analyzer. Lipids were assigned using the exact mass search in LipidMaps[209] based on the accurate mass of the precursor ion with a mass tolerance of 5 ppm and some assignments were confirmed by on-tissue MS/MS analysis[202].

For image creation and data analysis, ImageQuest 1.0.1 (Thermo Scientific, Germany), and the open-source MS imaging software, MSiReader[91] were used. With the raw-to-imzML-converter[93], the standard Thermo data file format (.raw) was reformatted into the (.imzML) file format, which is supported by MSiReader software. Images were extracted with a mass window of 5 ppm, and saved as TIFF file. Image normalization was done by dividing the signal of the tissue lipids of interest by that of the internal standards in each point.

4.2.6 Direct injection and laser ablation ICP-MS analysis

Nitrocellulose membranes (NC) (Whatman® Protran® nitrocellulose membranes, Dassel, Germany) of approximately 10x10 mm were fixed to glass slides next to the tissue sections and printed simultaneously. The printed membranes were collected and used for direct infusion ICP-MS as well as LA-ICP-MS.

Direct infusion ICP-MS

The collected NC membranes were weighed and digested in 150 µL 69% HNO3 (HNO3, ultraquality, Carl Roth, Germany) for direct injection ICP-MS analysis. Digested samples were diluted in a ratio of 1:10 in 3.5% HNO_3 including 10 µL Pr (100 µg L^{-1}) as internal standard to a final volume of 500 µL. For external calibration, a solution series from 20 ng L^{-1} to 10 µg L^{-1} using Tm standard solution was prepared. The sector field (Element XR, Thermo Fisher Scientifc, Bremen, Germany) was connected to a Meinhard-type nebulizer with a cyclonic spray chamber (MicroMist, Glass Expansion, Melbourne, Australia) using a nebulizer gas flow rate of 1.0 L min^{-1}

Ar. The instrument was operated at plasma gas flow of 15 L min^{-1}, auxiliary gas flow of 1.00 L min^{-1}, and RF plasma power of 1250 W.

LA-ICP-MS

LA-ICP-MS analysis was performed on a commercial LA system (UP-213, ESI, Portland, USA) coupled to the ICP-MS (Element XR, Thermo Fisher Scientific, Bremen, Germany). The ICP-MS was synchronized using the LA unit in an external trigger mode. The operating conditions are shown in **Error! Reference source not found.**. The ICP-MS operating conditions were tuned daily for maximum intensity and low oxide ratio ((ThO/Th) < 0.7%) using a reference glass slide (SRM 612, NIST, Maryland USA). The printed nitrocellulose membranes were ablated continuously in line scans. Overlapping line scans and high laser shot repetition rates were applied to ensure complete ablation of the membrane sample.

Mass traces of ^{169}Tm were recorded at low resolution (R=300). The analysis of a nitrocellulose membrane (with 2×2 mm average dimensions) required about 20 min. Data was exported to Origin 2016 (OriginLab Corporation, Northampton, MA) where generation of color coded images was performed.

Table 6. Instrumental parameters of the LA-ICP-MS measurements.

ICP-MS		LA system	
RF plasma power	1257 W	Wavelength	213 nm
Plasma gas flow (Ar)	15 L min^{-1}	Helium gas flow	0.8 L min^{-1}
Sample gas flow (Ar)	1.3 L min^{-1}	Laser energy	100% (5.16 J cm^{-2})
Auxiliary gas flow (Ar)	0.99 L min^{-1}	Laser spot size	100 µm
Mass resolution ($m/\Delta m$)	300 (LR)	Scan speed	100 µm s^{-1}
Sample time	2 ms	Repetition rate	20 Hz
Scanning mode	E scan	Line overlapping	20%
Detected isotope	^{169}Tm		

5 Abbreviations

Abbreviation	Full name
ACN	Acetonitrile
AP MALDI	Atmospheric pressure matrix-assisted laser desorption ionization
α-CHCA	α-cyano-4-hydroxycinnamic acid
CID	Collision-induced dissociation
CMC	Carboxymethylcellulose
CPCD	Coupled physical and chemical dynamics model
DC	Direct current
DESI	Desorption electrospray ionization
DHB	2,5-dihydroxybenzoic acid
DHSM	Dihydroxysphingomyelin
DHCer	Dihydroxyceramide
ELISA	Enzyme-linked immunosorbent assays
ESI-MS	Electrospray ionization mass spectrometry
FDR	False discovery rate
FFT	Fast Fourier Transformation
FFPE	Formalin-fixed paraffin-embedded
FTICR	Fourier transform ion cyclotron resonance
GC	Gas chromatography
GPLs	Glycerophospholipids
h	Hour
H&E	Hematoxilin-eosin
HMDB	Human Metabolome Database
HPLC	High-performance liquid chromatography
HRMS	High Resolution MS
ICP-MS	Inductively coupled plasma mass spectrometry
iPrOH	Isopropanol
IP	Ionization potential
i.p.	Intraperitoneal
ITO	Indium tin oxide
LA-ICP	Laser ablation inductively coupled plasma
LC	Liquid chromatography
LMSD	Lipid Maps Structure Database
LTQ	Linear trap quadropole

LAESI	Laser ablation electrospray ionization
LESA	Liquid extraction surface analysis
LMSD	Lipid Maps Structure Database
LPC or lyso-PC	Lysophosphatidylcholines
MALDI MSI	Matrix-assisted laser desorption ionization mass spectrometry imaging
MALDI-TOF	Matrix-assisted laser desorption ionization time of flight
MeOH	Methanol
MSI	Mass spectrometry imaging
MS	Mass spectrometry
MS/MS	Tandem mass spectrometry
MSM	Metabolite-signal match
MRI	Magnetic Resonance Imaging
m/z	Mass-to-charge ratio
NC	Nitrocellulose
NL	Neutral loss
NMR	Nuclear magnetic resonance
NPLC	Normal-phase liquid chromatography
ns	Nanosecond
OCT	Optimal cutting temperature
PC	Phosphatidylcholine
PE	Phosphatidylethanolamine
PI	Phosphatidylinositol
PCA	Principal component analysis
PUFAs	Polyunsaturated fatty acids
RPLC	Reversed-phase liquid chromatography
RF	Radiofrequency
SA	sinapic acid, 3,5-dimethoxy-4-hydroxycinnamic acid
SIMS	Secondary ion mass spectrometry
SM	Sphingomyelin
s	Second
TFA	Trifluoroacetic acid
TLC	Thin-layer chromatography
TOF	Time of flight

6 References

1. Wu, C.P., et al., *Mass spectrometry imaging under ambient conditions.* Mass Spectrometry Reviews, 2013. **32**(3): p. 218-243.

2. McDonnell, L.A. and R.M.A. Heeren, *Imaging mass spectrometry.* Mass Spectrometry Reviews, 2007. **26**(4): p. 606-643.

3. Chughtai, K. and R.M.A. Heeren, *Mass Spectrometric Imaging for Biomedical Tissue Analysis.* Chemical Reviews, 2010. **110**(5): p. 3237-3277.

4. Caprioli, R.M., T.B. Farmer, and J. Gile, Molecular Imaging of Biological Samples: Localization of Peptides and Proteins Using MALDI-TOF MS. Analytical Chemistry, 1997. **69**(23): p. 4751-4760.

5. LANDGRAF, R.R., ANALYSIS OF LIPIDS IN NERVE TISSUE BY MALDI TANDEM MASS SPECTROMETRIC IMAGING.

6. Bodzon-Kulakowska, A. and P. Suder, IMAGING MASS SPECTROMETRY: INSTRUMENTATION, APPLICATIONS, AND COMBINATION WITH OTHER VISUALIZATION TECHNIQUES. Mass Spectrometry Reviews, 2016. **35**(1): p. 147-169.

7. Addie, R.D., et al., Current State and Future Challenges of Mass Spectrometry Imaging for Clinical Research. Analytical Chemistry, 2015. **87**(13): p. 6426-6433.

8. Slaveykova, V.I., et al., *Dynamic NanoSIMS ion imaging of unicellular freshwater algae exposed to copper.* Analytical and Bioanalytical Chemistry, 2009. **393**(2): p. 583-589.

9. Fletcher, J.S., *Cellular imaging with secondary ion mass spectrometry.* Analyst, 2009. **134**(11): p. 2204-2215.

10. Bloom, A.N., H. Tian, and N. Winograd, *C-60-SIMS imaging of nanoparticles within mammalian cells.* Biointerphases, 2016. **11**(2).

11. Bloom, A.N., et al., Label-free visualization of nilotinib-functionalized gold nanoparticles within single mammalian cells by C-60-SIMS imaging. Analytical and Bioanalytical Chemistry, 2017. **409**(12): p. 3067-3076.

12. Debois, D., et al., In situ localisation and quantification of surfactins in a Bacillus subtilis swarming community by imaging mass spectrometry. Proteomics, 2008. **8**(18): p. 3682-3691.

13. Yang, Y.L., et al., *Translating metabolic exchange with imaging mass spectrometry.* Nature Chemical Biology, 2009. **5**(12): p. 885-887.

14. Esquenazi, E., P.C. Dorrestein, and W.H. Gerwick, *Probing marine natural product defenses with DESI-imaging mass spectrometry.* Proceedings of the National Academy of Sciences of the United States of America, 2009. **106**(18): p. 7269-7270.

15. Lane, A.L., et al., Desorption electrospray ionization mass spectrometry reveals surface-mediated antifungal chemical defense of a tropical seaweed. Proceedings of the National Academy of Sciences of the United States of America, 2009. **106**(18): p. 7314-7319.

16. Esquenazi, E., et al., Visualizing the spatial distribution of secondary metabolites produced by marine cyanobacteria and sponges via MALDI-TOF imaging. Molecular Biosystems, 2008. **4**(6): p. 562-570.

17. Cha, S.W., et al., Direct profiling and imaging of plant metabolites in intact tissues by using colloidal graphite-assisted laser desorption ionization mass spectrometry. Plant Journal, 2008. **55**(2): p. 348-360.

18. Mikawa, S., et al., Imaging of phosphatidylcholines in the adult rat brain using MALDI-TOF MS. Neuroscience Letters, 2009. **451**(1): p. 45-49.

19. Chaurand, P., et al., Profiling and imaging proteins in the mouse epididymis by imaging mass spectrometry. Proteomics, 2003. **3**(11): p. 2221-2239.

20. Stoeckli, M., et al., *Imaging of a β-Peptide Distribution in Whole-Body Mice Sections by MALDI Mass Spectrometry.* Journal of the American Society for Mass Spectrometry, 2007. **18**(11): p. 1921-1924.

21. Stoeckli, M., D. Staab, and A. Schweitzer, *Compound and metabolite distribution measured by MALDI mass spectrometric imaging in whole-body tissue sections.* International Journal of Mass Spectrometry, 2007. **260**(2-3): p. 195-202.

22. Trim, P.J., et al., Matrix-Assisted Laser Desorption/Ionization-Ion Mobility Separation-Mass Spectrometry Imaging of Vinblastine in Whole Body Tissue Sections. Analytical Chemistry, 2008. **80**(22): p. 8628-8634.

23. Brunelle, A. and O. Laprévote, *Lipid imaging with cluster time-of-flight secondary ion mass spectrometry.* Analytical and Bioanalytical Chemistry, 2008. **393**(1): p. 31.

24. Liu, Q., et al., Metabolite Imaging Using Matrix-Enhanced Surface-Assisted Laser Desorption/Ionization Mass Spectrometry (ME-SALDI-MS). Journal of the American Society for Mass Spectrometry, 2009. **20**(1): p. 80-88.

25. Chaurand, P., et al., Imaging Mass Spectrometry of Intact Proteins from Alcohol-Preserved Tissue Specimens: Bypassing Formalin Fixation. Journal of Proteome Research, 2008. **7**(8): p. 3543-3555.

26. Djidja, M.-C., et al., Detergent addition to tryptic digests and ion mobility separation prior to MS/MS improves peptide yield and protein identification for in situ proteomic investigation of frozen and formalin-fixed paraffin-embedded adenocarcinoma tissue sections. PROTEOMICS, 2009. **9**(10): p. 2750-2763.

27. Suits, F., et al., *Correlation Queries for Mass Spectrometry Imaging.* Analytical Chemistry, 2013. **85**(9): p. 4398-4404.

28. Palmer, A., Information Processing for Mass Spectrometry Imaging. 2014, University of Birmingham.

29. Palmer, A., D. Trede, and T. Alexandrov, *Where imaging mass spectrometry stands: here are the numbers.* Metabolomics, 2016. **12**(6): p. 1-3.

30. Han, X., *Imaging Mass Spectrometry of Lipids*, in *Lipidomics*. 2016, John Wiley & Sons, Inc. p. 259-280.

31. Weibel, D., et al., A C60 Primary Ion Beam System for Time of Flight Secondary Ion Mass Spectrometry: Its Development and Secondary Ion Yield Characteristics. Analytical Chemistry, 2003. **75**(7): p. 1754-1764.

32. Klerk, L.A., et al., *C60+ Secondary Ion Microscopy Using a Delay Line Detector.* Analytical Chemistry, 2010. **82**(3): p. 801-807.

33. Kaletas, B.K., et al., *Sample preparation issues for tissue imaging by imaging MS.* Proteomics, 2009. **9**(10): p. 2622-2633.

34. Ostrowski, S.G., et al., Secondary ion MS imaging to relatively quantify cholesterol in the membranes of individual cells from differentially treated populations. Analytical Chemistry, 2007. **79**(10): p. 3554-3560.

35. Wu, L.G., et al., *Imaging and differentiation of mouse embryo tissues by ToF-SIMS.* International Journal of Mass Spectrometry, 2007. **260**(2-3): p. 137-145.

36. Nygren, H., et al., *Imaging TOF-SIMS of rat kidney prepared by high-pressure freezing.* Microscopy Research and Technique, 2005. **68**(6): p. 329-334.

37. Jones, E.A., N.P. Lockyer, and J.C. Vickerman, *Mass spectral analysis and imaging of tissue by ToF-SIMS—The role of buckminsterfullerene, C60+, primary ions.* International Journal of Mass Spectrometry, 2007. **260**(2): p. 146-157.

38. Spengler, B., *Mass Spectrometry Imaging of Biomolecular Information.* Analytical Chemistry, 2015. **87**(1): p. 64-82.

39. Francese, S., et al., *MALDI Mass Spectrometry Imaging, from its Origins up to Today: The State of the Art.* Combinatorial Chemistry & High Throughput Screening, 2009. **12**(2): p. 156-174.

40. Takáts, Z., et al., Mass Spectrometry Sampling Under Ambient Conditions with Desorption Electrospray Ionization. Science, 2004. **306**(5695): p. 471-473.

41. Ifa, D.R., et al., Development of capabilities for imaging mass spectrometry under ambient conditions with desorption electrospray ionization (DESI). International Journal of Mass Spectrometry, 2007. **259**(1): p. 8-15.

42. Ellis, S.R., A.L. Bruinen, and R.M.A. Heeren, *A critical evaluation of the current state-of-the-art in quantitative imaging mass spectrometry.* Analytical and Bioanalytical Chemistry, 2014. **406**(5): p. 1275-1289.

43. Kertesz, V. and G.J. Van Berkel, *Improved imaging resolution in desorption electrospray ionization mass spectrometry.* Rapid Communications in Mass Spectrometry, 2008. **22**(17): p. 2639-2644.

44. Eberlin, L.S., et al., Nondestructive, Histologically Compatible Tissue Imaging by Desorption Electrospray Ionization Mass Spectrometry. Chembiochem, 2011. **12**(14): p. 2129-2132.

45. Eberlin, L.S., et al., Desorption Electrospray Ionization then MALDI Mass Spectrometry Imaging of Lipid and Protein Distributions in Single Tissue Sections. Analytical Chemistry, 2011. **83**(22): p. 8366-8371.

46. Perry, R.H., et al., *Characterization of MYC-Induced Tumorigenesis by in Situ Lipid Profiling.* Analytical Chemistry, 2013. **85**(9): p. 4259-4262.

47. Gerbig, S., et al., Analysis of colorectal adenocarcinoma tissue by desorption electrospray ionization mass spectrometric imaging. Analytical and Bioanalytical Chemistry, 2012. **403**(8): p. 2315-2325.

48. Wiseman, J.M., et al., *Desorption electrospray ionization mass spectrometry: Imaging drugs and metabolites in tissues.* Proceedings of the National Academy of Sciences, 2008. **105**(47): p. 18120-18125.

49. Spengler, B., M. Hubert, and R. Kaufmann. MALDI ion imaging and biological ion imaging with a new scanning UV-laser microprobe. in Proceedings of the 42nd Annual Conference on Mass Spectrometry and Allied Topics. 1994. Chicago, Illinois.

50. Gessel, M.M., J.L. Norris, and R.M. Caprioli, *MALDI imaging mass spectrometry: Spatial molecular analysis to enable a new age of discovery.* Journal of Proteomics, 2014. **107**(Supplement C): p. 71-82.

51. Lemaire, R., et al., MALDI-MS direct tissue analysis of proteins: improving signal sensitivity using organic treatments. Analytical Chemistry, 2006. **78**(20): p. 7145-7153.

52. Metz, B., et al., Identification of formaldehyde-induced modifications in proteins - Reactions with model peptides. Journal of Biological Chemistry, 2004. **279**(8): p. 6235-6243.

53. Carter, C.L., C.W. McLeod, and J. Bunch, *Imaging of Phospholipids in Formalin Fixed Rat Brain Sections by Matrix Assisted Laser Desorption/Ionization Mass Spectrometry.* Journal of the American Society for Mass Spectrometry, 2011. **22**(11): p. 1991-1998.

54. Goodwin, R.J.A., Sample preparation for mass spectrometry imaging: Small mistakes can lead to big consequences. Journal of Proteomics, 2012. **75**(16): p. 4893-4911.

55. Schwartz, S.A., M.L. Reyzer, and R.M. Caprioli, Direct tissue analysis using matrix-assisted laser desorption/ionization mass spectrometry: practical aspects of sample preparation. Journal of Mass Spectrometry, 2003. **38**(7): p. 699-708.

56. Chaurand, P., et al., *Monitoring mouse prostate development by profiling and imaging mass spectrometry.* Molecular & Cellular Proteomics, 2008. **7**(2): p. 411-423.

57. Goodwin, R.J.A., et al., Matrix-free mass spectrometric imaging using laser desorption ionisation Fourier transform ion cyclotron resonance mass spectrometry. Rapid Communications in Mass Spectrometry, 2011. **25**(7): p. 969-972.

58. Seeley, E.H., et al., Enhancement of protein sensitivity for MALDI imaging mass spectrometry after chemical treatment of tissue sections. Journal of the American Society for Mass Spectrometry, 2008. **19**(8): p. 1069-1077.

59. Norris, J.L. and R.M. Caprioli, Analysis of Tissue Specimens by Matrix-Assisted Laser Desorption/Ionization Imaging Mass Spectrometry in Biological and Clinical Research. Chemical Reviews, 2013. **113**(4): p. 2309-2342.

60. Cole, L.M., et al., Investigation of protein induction in tumour vascular targeted strategies by MALDI MSI. Methods, 2011. **54**(4): p. 442-453.

61. Chacon, A., et al., On-tissue chemical derivatization of 3-methoxysalicylamine for MALDI-imaging mass spectrometry. Journal of Mass Spectrometry, 2011. **46**(8): p. 840-846.

62. Börnsen, K.O., Influence of Salts, Buffers, Detergents, Solvents, and Matrices on MALDI-MS Protein Analysis in Complex Mixtures, in Mass Spectrometry of Proteins

and Peptides: Mass Spectrometry of Proteins and Peptides, J.R. Chapman, Editor. 2000, Humana Press: Totowa, NJ. p. 387-404.

63. Meriaux, C., et al., *Liquid ionic matrixes for MALDI mass spectrometry imaging of lipids.* Journal of Proteomics, 2010. **73**(6): p. 1204-1218.

64. Su, C.-L. and W.-L. Tseng, Gold Nanoparticles as Assisted Matrix for Determining Neutral Small Carbohydrates through Laser Desorption/Ionization Time-of-Flight Mass Spectrometry. Analytical Chemistry, 2007. **79**(4): p. 1626-1633.

65. Cha, S., et al., Direct profiling and imaging of plant metabolites in intact tissues by using colloidal graphite-assisted laser desorption ionization mass spectrometry. The Plant Journal, 2008. **55**(2): p. 348-360.

66. Peterson, D.S., *Matrix-free methods for laser desorption/ionization mass spectrometry.* Mass Spectrometry Reviews, 2007. **26**(1): p. 19-34.

67. Hillenkamp, F., MALDI MS : a practical guide to instrumentation, methods and applications / ed. by Franz Hillenkamp. 2. ed. ed. 2014, Weinheim: Weinheim : Wiley-Blackwell.

68. Gode, D. and D.A. Volmer, *Lipid imaging by mass spectrometry - a review.* Analyst, 2013. **138**(5): p. 1289-1315.

69. Landgraf, R.R., et al., Considerations for quantification of lipids in nerve tissue using matrix-assisted laser desorption/ionization mass spectrometric imaging. Rapid Communications in Mass Spectrometry, 2011. **25**(20): p. 3178-3184.

70. O'Connor, P.B. and F. Hillenkamp, *MALDI Mass Spectrometry Instrumentation*, in *MALDI MS*. 2007, Wiley-VCH Verlag GmbH & Co. KGaA. p. 29-82.

71. Carter, C.L., The Analysis and Imaging of Lipids from Complex Samples by Matrix-Assisted Laser Desorption/Ionisation Mass Spectrometry. 2011, School of Chemistry, University of Birmingham.

72. Qiao, H., V. Spicer, and W. Ens, The effect of laser profile, fluence, and spot size on sensitivity in orthogonal-injection matrix-assisted laser desorption/ionization time-of-flight mass spectrometry. Rapid Communications in Mass Spectrometry, 2008. **22**(18): p. 2779-2790.

73. Knochenmuss, R. and L.V. Zhigilei, Molecular dynamics simulations of MALDI: laser fluence and pulse width dependence of plume characteristics and consequences for matrix and analyte ionization. Journal of Mass Spectrometry, 2010. **45**(4): p. 333-346.

74. Dreisewerd, K., *The desorption process in MALDI.* Chemical Reviews, 2003. **103**(2): p. 395-425.

75. Karas, M., et al., *The initial-ion velocity as a marker for different desorption-ionization mechanisms in MALDI.* International Journal of Mass Spectrometry, 2003. **226**(1): p. 239-248.

76. Knochenmuss, R., A quantitative model of ultraviolet matrix-assisted laser desorption/ionization including analyte ion generation. Analytical Chemistry, 2003. **75**(10): p. 2199-2207.

77. Jaskolla, T.W. and M. Karas, Compelling Evidence for Lucky Survivor and Gas Phase Protonation: The Unified MALDI Analyte Protonation Mechanism. Journal of the American Society for Mass Spectrometry, 2011. **22**(6): p. 976-988.

78. Karas, M., M. Glückmann, and J. Schäfer, Ionization in matrix-assisted laser desorption/ionization: singly charged molecular ions are the lucky survivors. Journal of Mass Spectrometry, 2000. **35**(1): p. 1-12.

79. Karas, M. and R. Kruger, *Ion formation in MALDI: The cluster ionization mechanism.* Chemical Reviews, 2003. **103**(2): p. 427-439.

80. Knochenmuss, R., *The Coupled Chemical and Physical Dynamics Model of MALDI.* Annual Review of Analytical Chemistry, 2016. **9**(1): p. 365-385.

81. Zenobi, R. and R. Knochenmuss, *Ion formation in MALDI mass spectrometry.* Mass Spectrometry Reviews, 1998. **17**(5): p. 337-366.

82. Knochenmuss, R., MALDI ionization mechanisms: the coupled photophysical and chemical dynamics model correctly predicts 'temperature'-selected spectra. Journal of Mass Spectrometry, 2013. **48**(9): p. 998-1004.

83. Knochenmuss, R., *Ion formation mechanisms in UV-MALDI.* Analyst, 2006. **131**(9): p. 966-986.

84. Krüger, R., et al., Analyte Incorporation and Ionization in Matrix-Assisted Laser Desorption/Ionization Visualized by pH Indicator Molecular Probes. Analytical Chemistry, 2001. **73**(24): p. 5812-5821.

85. Knochenmuss, R. and A. Vertes, *Time-delayed 2-Pulse Studies of MALDI Matrix Ionization Mechanisms.* The Journal of Physical Chemistry B, 2000. **104**(23): p. 5406-5410.

86. Mukamel, S. and D. Abramavicius, Many-Body Approaches for Simulating Coherent Nonlinear Spectroscopies of Electronic and Vibrational Excitons. Chemical Reviews, 2004. **104**(4): p. 2073-2098.

87. Jungmann, J.H. and R.M.A. Heeren, *Emerging technologies in mass spectrometry imaging.* Journal of Proteomics, 2012. **75**(16): p. 5077-5092.

88. Schwartz, J.C., M.W. Senko, and J.E.P. Syka, *A two-dimensional quadrupole ion trap mass spectrometer.* Journal of the American Society for Mass Spectrometry, 2002. **13**(6): p. 659-669.

89. Cole, R.B., Electrospray and MALDI mass spectrometry : fundamentals, instrumentation, practicalities, and biological applications / ed. by Richard B. Cole. 2. ed. ed. Electrospray ionization mass spectrometry. 2010, Hoboken, N.J.: Hoboken, N.J. : Wiley.

90. Makarov, A., Electrostatic Axially Harmonic Orbital Trapping: A High-Performance Technique of Mass Analysis. Analytical Chemistry, 2000. **72**(6): p. 1156-1162.

91. Robichaud, G., et al., MSiReader: An Open-Source Interface to View and Analyze High Resolving Power MS Imaging Files on Matlab Platform. Journal of The American Society for Mass Spectrometry, 2013. **24**(5): p. 718-721.

92. Rübel, O., et al., OpenMSI: A High-Performance Web-Based Platform for Mass Spectrometry Imaging. Analytical Chemistry, 2013. **85**(21): p. 10354-10361.

93. Schramm, T., et al., imzML - A common data format for the flexible exchange and processing of mass spectrometry imaging data. Journal of Proteomics, 2012. **75**(16): p. 5106-5110.

94. Rompp, A., et al., imzML: Imaging Mass Spectrometry Markup Language: A Common Data Format for Mass Spectrometry Imaging, in Data Mining in Proteomics: From Standards to Applications, M. Hamacher, M. Eisenacher, and C. Stephan, Editors. 2011. p. 205-224.

95. Norris, J.L., et al., *Processing MALDI mass spectra to improve mass spectral direct tissue analysis.* International Journal of Mass Spectrometry, 2007. **260**(2–3): p. 212-221.

96. Hoffmann, E.d., *Mass spectrometry : principles and applications* 3ed, ed. V. Stroobant. 2007: Chichester [u.a.] : Wiley.

97. Alexandrov, T., MALDI imaging mass spectrometry: statistical data analysis and current computational challenges. Bmc Bioinformatics, 2012. **13**.

98. Fonville, J.M., et al., Robust Data Processing and Normalization Strategy for MALDI Mass Spectrometric Imaging. Analytical Chemistry, 2012. **84**(3): p. 1310-1319.

99. Burrell, M.M., C.J. Earnshaw, and M.R. Clench, Imaging Matrix Assisted Laser Desorption Ionization Mass Spectrometry: a technique to map plant metabolites within tissues at high spatial resolution. Journal of Experimental Botany, 2007. **58**(4): p. 757-763.

100. Deininger, S.-O., et al., *Normalization in MALDI-TOF imaging datasets of proteins: practical considerations.* Analytical and Bioanalytical Chemistry, 2011. **401**(1): p. 167-181.

101. Groseclose, M.R. and S. Castellino, A Mimetic Tissue Model for the Quantification of Drug Distributions by MALDI Imaging Mass Spectrometry. Analytical Chemistry, 2013. **85**(21): p. 10099-10106.

102. Nilsson, A., et al., Fine Mapping the Spatial Distribution and Concentration of Unlabeled Drugs within Tissue Micro-Compartments Using Imaging Mass Spectrometry. PLOS ONE, 2010. **5**(7): p. e11411.

103. Prideaux, B., et al., High-Sensitivity MALDI-MRM-MS Imaging of Moxifloxacin Distribution in Tuberculosis-Infected Rabbit Lungs and Granulomatous Lesions. Analytical Chemistry, 2011. **83**(6): p. 2112-2118.

104. Pirman, D.A., et al., Identifying Tissue-Specific Signal Variation in MALDI Mass Spectrometric Imaging by Use of an Internal Standard. Analytical Chemistry, 2013. **85**(2): p. 1090-1096.

105. Gustafsson, J.O.R., et al., Internal calibrants allow high accuracy peptide matching between MALDI imaging MS and LC-MS/MS. Journal of Proteomics, 2012. **75**(16): p. 5093-5105.

106. McDonnell, L.A., et al., *Mass spectrometry image correlation: Quantifying colocalization.* Journal of Proteome Research, 2008. **7**(8): p. 3619-3627.

107. McDonnell, L.A., et al., *Subcellular imaging mass spectrometry of brain tissue.* Journal of Mass Spectrometry, 2005. **40**(2): p. 160-168.

108. Vaysse, P.-M., et al., Mass spectrometry imaging for clinical research - latest developments, applications, and current limitations. Analyst, 2017. **142**(15): p. 2690-2712.

109. Robbe, M.-F., et al., *Software Tools of the Computis European Project to Process Mass Spectrometry Images.* European Journal of Mass Spectrometry, 2014. **20**(5): p. 351-360.

110. Deininger, S.O., M. Becker, and D. Suckau, Tutorial: Multivariate Statistical Treatment of Imaging Data for Clinical Biomarker Discovery, in Mass Spectrometry Imaging: Principles and Protocols, S.S. Rubakhin and J.V. Sweedler, Editors. 2010. p. 385-403.

111. Trede, D., et al., On the importance of mathematical methods for analysis of MALDI-imaging mass spectrometry data. J Integr Bioinform, 2012. **9**(1): p. 189.

112. Schwartz, S.A., et al., *Protein Profiling in Brain Tumors Using Mass Spectrometry.* Clinical Cancer Research, 2004. **10**(3): p. 981.

113. Chaurand, P., S.A. Schwartz, and R.M. Caprioli, *Assessing Protein Patterns in Disease Using Imaging Mass Spectrometry.* Journal of Proteome Research, 2004. **3**(2): p. 245-252.

114. Sköld, K., et al., *Decreased Striatal Levels of PEP-19 Following MPTP Lesion in the Mouse.* Journal of Proteome Research, 2006. **5**(2): p. 262-269.

115. Han, J. and K.L. Schey, *MALDI Tissue Imaging of Ocular Lens α-Crystallin.* Investigative Ophthalmology & Visual Science, 2006. **47**(7): p. 2990-2996.

116. Stoeckli, M., et al., Molecular imaging of amyloid beta peptides in mouse brain sections using mass spectrometry. Analytical Biochemistry, 2002. **311**(1): p. 33-39.

117. Hanrieder, J., et al., L-DOPA-induced dyskinesia is associated with regional increase of striatal dynorphin peptides as elucidated by imaging mass spectrometry. Pharmacological Reports, 2011. **63**(1): p. 264-264.

118. Schober, Y., et al., High-resolution matrix-assisted laser desorption/ionization imaging of tryptic peptides from tissue. Rapid Communications in Mass Spectrometry, 2012. **26**(9): p. 1141-1146.

119. Ljungdahl, A., et al., Imaging Mass Spectrometry Reveals Elevated Nigral Levels of Dynorphin Neuropeptides in L-DOPA-Induced Dyskinesia in Rat Model of Parkinson's Disease. PLOS ONE, 2011. **6**(9): p. e25653.

120. Acquadro, E., et al., Matrix-Assisted Laser Desorption Ionization Imaging Mass Spectrometry Detection of a Magnetic Resonance Imaging Contrast Agent in Mouse Liver. Analytical Chemistry, 2009. **81**(7): p. 2779-2784.

121. Huang, J.-T., et al., Molecular imaging of drug-eluting coronary stents: method development, optimization and selected applications. Journal of Mass Spectrometry, 2012. **47**(2): p. 155-162.

122. Sugiura, Y., et al., Visualization of the cell-selective distribution of PUFA-containing phosphatidylcholines in mouse brain by imaging mass spectrometry. Journal of Lipid Research, 2009. **50**(9): p. 1776-1788.

123. Hankin, J.A., et al., *MALDI Mass Spectrometric Imaging of Lipids in Rat Brain Injury Models.* Journal of The American Society for Mass Spectrometry, 2011. **22**(6): p. 1014.

124. Lee, D.Y., et al., Resolving brain regions using nanostructure initiator mass spectrometry imaging of phospholipids. Integrative Biology, 2012. **4**(6): p. 693-699.

125. Börner, K., et al., *Molecular imaging of lipids in cells and tissues.* International Journal of Mass Spectrometry, 2007. **260**(2): p. 128-136.

126. Koizumi, S., et al., Imaging mass spectrometry revealed the production of lyso-phosphatidylcholine in the injured ischemic rat brain. Neuroscience, 2010. **168**(1): p. 219-225.

127. Hayasaka, T., et al., Matrix-assisted laser desorption/ionization quadrupole ion trap time-of-flight (MALDI-QIT-TOF)-based imaging mass spectrometry reveals a layered distribution of phospholipid molecular species in the mouse retina. Rapid Communications in Mass Spectrometry, 2008. **22**(21): p. 3415-3426.

128. Marsching, C., et al., Imaging of complex sulfatides SM3 and SB1a in mouse kidney using MALDI-TOF/TOF mass spectrometry. Analytical and Bioanalytical Chemistry, 2011. **401**(1): p. 53-64.

129. Enomoto, H., et al., Visualization of phosphatidylcholine, lysophosphatidylcholine and sphingomyelin in mouse tongue body by matrix-assisted laser desorption/ionization imaging mass spectrometry. Analytical and Bioanalytical Chemistry, 2011. **400**(7): p. 1913-1921.

130. Veloso, A., et al., *Anatomical Distribution of Lipids in Human Brain Cortex by Imaging Mass Spectrometry.* Journal of The American Society for Mass Spectrometry, 2011. **22**(2): p. 329-338.

131. Willems, S.M., et al., Imaging mass spectrometry of myxoid sarcomas identifies proteins and lipids specific to tumour type and grade, and reveals biochemical intratumour heterogeneity. The Journal of Pathology, 2010. **222**(4): p. 400-409.

132. Liu, Y., et al., Elevation of sulfatides in ovarian cancer: An integrated transcriptomic and lipidomic analysis including tissue-imaging mass spectrometry. Molecular Cancer, 2010. **9**(1): p. 186.

133. Deeley, J.M., et al., *Sphingolipid distribution changes with age in the human lens.* Journal of Lipid Research, 2010. **51**(9): p. 2753-2760.

134. Chughtai, K., et al., Fiducial Markers for Combined 3-Dimensional Mass Spectrometric and Optical Tissue Imaging. Analytical Chemistry, 2012. **84**(4): p. 1817-1823.

135. Attia, Ahmed S., et al., Monitoring the Inflammatory Response to Infection through the Integration of MALDI IMS and MRI. Cell Host & Microbe, 2012. **11**(6): p. 664-673.

136. Li, H. and A.B. Hummon, *Imaging Mass Spectrometry of Three-Dimensional Cell Culture Systems.* Analytical Chemistry, 2011. **83**(22): p. 8794-8801.

137. Crecelius, A.C., et al., *Three-Dimensional Visualization of Protein Expression in Mouse Brain Structures Using Imaging Mass Spectrometry.* Journal of the American Society for Mass Spectrometry, 2005. **16**(7): p. 1093-1099.

138. Andersson, M., et al., Imaging mass spectrometry of proteins and peptides: 3D volume reconstruction. Nature Methods, 2008. **5**: p. 101.

139. Kompauer, M., S. Heiles, and B. Spengler, Autofocusing MALDI mass spectrometry imaging of tissue sections and 3D chemical topography of nonflat surfaces. Nature Methods, 2017. **14**: p. 1156.

140. Matusch, A., et al., Combined Elemental and Biomolecular Mass Spectrometry Imaging for Probing the Inventory of Tissue at a Micrometer Scale. Analytical Chemistry, 2012. **84**(7): p. 3170-3178.

141. Becker, J.S., et al., Bioimaging of metals by laser ablation inductively coupled plasma mass spectrometry (LA-ICP-MS). Mass Spectrometry Reviews, 2010. **29**(1): p. 156-175.

142. Schaumlöffel, D., et al., Novel Methods for Bioimaging Including LA-ICP-MS, NanoSIMS, TEM/X-EDS, and SXRF, in Metallomics. 2016, Wiley-VCH Verlag GmbH & Co. KGaA. p. 83-116.

143. Chughtai, S., et al., *A multimodal mass spectrometry imaging approach for the study of musculoskeletal tissues.* International Journal of Mass Spectrometry, 2012. **325-327**: p. 150-160.

144. Eberlin, L.S., et al., *Ambient mass spectrometry for the intraoperative molecular diagnosis of human brain tumors.* Proceedings of the National Academy of Sciences, 2013. **110**(5): p. 1611-1616.

145. Han, X., Lipidomics : comprehensive mass spectrometry of lipids / Xianlin Han, Sanford Burnham Prebys Medical Discovery Institute, Orlando, Florida. 2016, Hoboken, New Jersey: Hoboken, New Jersey : Wiley.

146. Brown, H.A. and R.C. Murphy, *Working towards an exegesis for lipids in biology.* Nature Chemical Biology, 2009. **5**: p. 602.

147. Fahy, E., et al., *Lipid classification, structures and tools.* Biochimica et Biophysica Acta (BBA) - Molecular and Cell Biology of Lipids, 2011. **1811**(11): p. 637-647.

148. Griffiths, W.J.W., Y., *Lipidomics in Metabolomics*, in *Comprehensive Biomedical Physics*, B.P. Anders Brahme, Editor. 2015, Elsevier B.V. p. 157-164.

149. Fuchs, B., et al., *Lipid analysis by thin-layer chromatography—A review of the current state.* Journal of Chromatography A, 2011. **1218**(19): p. 2754-2774.

150. Tang, B. and K.H. Row, *Development of Gas Chromatography Analysis of Fatty Acids in Marine Organisms.* Journal of Chromatographic Science, 2013. **51**(7): p. 599-607.

151. Goodridge, C.F., et al., ELISA for Monitoring Lipid Oxidation in Chicken Myofibrils through Quantification of Hexanal−Protein Adducts. Journal of Agricultural and Food Chemistry, 2003. **51**(26): p. 7533-7539.

152. Knothe, G. and J.A. Kenar, *Determination of the fatty acid profile by 1H-NMR spectroscopy.* European Journal of Lipid Science and Technology, 2004. **106**(2): p. 88-96.

153. Harkewicz, R. and E.A. Dennis, *Applications of Mass Spectrometry to Lipids and Membranes.* Annual Review of Biochemistry, 2011. **80**(1): p. 301-325.

154. Li, L., et al., *Mass Spectrometry Methodology in Lipid Analysis.* International Journal of Molecular Sciences, 2014. **15**(6): p. 10492.

155. Yang, K. and X. Han, *Lipidomics: Techniques, Applications, and Outcomes Related to Biomedical Sciences.* Trends in Biochemical Sciences, 2016. **41**(11): p. 954-969.

156. Murphy, R.C., J.A. Hankin, and R.M. Barkley, *Imaging of lipid species by MALDI mass spectrometry.* Journal of Lipid Research, 2009. **50**: p. S317-S322.

157. Ståhlman, M., et al., *High-throughput shotgun lipidomics by quadrupole time-of-flight mass spectrometry.* Journal of Chromatography B, 2009. **877**(26): p. 2664-2672.

158. Cajka, T. and O. Fiehn, Comprehensive analysis of lipids in biological systems by liquid chromatography-mass spectrometry. TrAC Trends in Analytical Chemistry, 2014. **61**: p. 192-206.

159. Han, X., et al., Metabolomics in Early Alzheimer's Disease: Identification of Altered Plasma Sphingolipidome Using Shotgun Lipidomics. PLOS ONE, 2011. **6**(7): p. e21643.

160. Jiang, X., et al., Alkaline methanolysis of lipid extracts extends shotgun lipidomics analyses to the low-abundance regime of cellular sphingolipids. Analytical Biochemistry, 2007. **371**(2): p. 135-145.

161. Wang, M., et al., *Novel advances in shotgun lipidomics for biology and medicine.* Progress in Lipid Research, 2016. **61**: p. 83-108.

162. Han, X., K. Yang, and R.W. Gross, Multi-dimensional mass spectrometry-based shotgun lipidomics and novel strategies for lipidomic analyses. Mass Spectrometry Reviews, 2012. **31**(1): p. 134-178.

163. Guo, X. and E. Lankmayr, Multidimensional approaches in LC and MS for phospholipid bioanalysis. Bioanalysis, 2010. **2**(6): p. 1109-1123.

164. Li, M., et al., *Analytical Methods in Lipidomics and Their Applications.* Analytical Chemistry, 2014. **86**(1): p. 161-175.

165. Dill, A.L., et al., *Mass spectrometric imaging of lipids using desorption electrospray ionization.* Journal of Chromatography B, 2009. **877**(26): p. 2883-2889.

166. Malmberg, P., et al., *Imaging of Lipids in Human Adipose Tissue by Cluster Ion TOF-SIMS.* Microscopy Research and Technique, 2007. **70**(9): p. 828-835.

167. Almeida, R., et al., Quantitative Spatial Analysis of the Mouse Brain Lipidome by Pressurized Liquid Extraction Surface Analysis. Analytical Chemistry, 2015. **87**(3): p. 1749-1756.

168. Sud, M., et al., *LMSD: LIPID MAPS structure database.* Nucleic Acids Research, 2007. **35**(suppl_1): p. D527-D532.

169. Smith, C.A., et al., *METLIN: A Metabolite Mass Spectral Database.* Therapeutic Drug Monitoring, 2005. **27**(6): p. 747-751.

170. Wishart, D.S., et al., *HMDB 3.0—The Human Metabolome Database in 2013.* Nucleic Acids Research, 2013. **41**(D1): p. D801-D807.

171. Palmer, A., et al., FDR-controlled metabolite annotation for high-resolution imaging mass spectrometry. Nat Meth, 2017. **14**(1): p. 57-60.

172. Miller, R.P., et al., *Mechanisms of Cisplatin Nephrotoxicity.* Toxins, 2010. **2**(11): p. 2490-2518.

173. Todd, R.C. and S.J. Lippard, *Inhibition of transcription by platinum antitumor compounds.* Metallomics, 2009. **1**(4): p. 280-291.

174. Pabla, N. and Z. Dong, *Cisplatin nephrotoxicity: Mechanisms and renoprotective strategies.* Kidney International, 2008. **73**(9): p. 994-1007.

175. Moreno-Gordaliza, E., et al., Elemental Bioimaging in Kidney by LA-ICP-MS As a Tool to Study Nephrotoxicity and Renal Protective Strategies in Cisplatin Therapies. Analytical Chemistry, 2011. **83**(20): p. 7933-7940.

176. Ognjanovic, B.I., et al., Lipid Peroxidative Damage on Cisplatin Exposure and Alterations in Antioxidant Defense System in Rat Kidneys: A Possible Protective Effect of Selenium. International Journal of Molecular Sciences, 2012. **13**(2): p. 1790-1803.

177. Zemski Berry, K.A., et al., *MALDI Imaging of Lipid Biochemistry in Tissues by Mass Spectrometry.* Chemical Reviews, 2011. **111**(10): p. 6491-6512.

178. Muller, L., et al., Lipid imaging within the normal rat kidney using silver nanoparticles by matrix-assisted laser desorption/ionization mass spectrometry. Kidney International, 2015. **88**(1): p. 186-192.

179. Ruh, H., et al., MALDI imaging MS reveals candidate lipid markers of polycystic kidney disease. Journal of Lipid Research, 2013. **54**(10): p. 2785-2794.

180. Rao, S., et al., *Early lipid changes in acute kidney injury using SWATH lipidomics coupled with MALDI tissue imaging.* American Journal of Physiology - Renal Physiology, 2016. **310**(10): p. F1136-F1147.

181. Porta, T., et al., Quantification in MALDI-MS imaging: what can we learn from MALDI-selected reaction monitoring and what can we expect for imaging? Analytical and Bioanalytical Chemistry, 2015. **407**(8): p. 2177-2187.

182. Esteban-Fernandez, D., et al., *SEC-ICP-MS and ESI-MS as tools to study the interaction between cisplatin and cytosolic biomolecules.* Journal of Analytical Atomic Spectrometry, 2007. **22**(9): p. 1113-1121.

183. Jensen, M., et al., *Cisplatin interaction with phosphatidylserine bilayer studied by solid-state NMR spectroscopy.* JBIC Journal of Biological Inorganic Chemistry, 2010. **15**(2): p. 213-223.

184. Portilla, D., et al., *Metabolomic study of cisplatin-induced nephrotoxicity*. Kidney International, 2006. **69**(12): p. 2194-2204.

185. Naleskina, L.A., et al., Alteration in lipid composition of plasma membranes of sensitive and resistant Guerin carcinoma cells due to the action of free and liposomal form of cisplatin. Experimental oncology, 2013. **35**(3): p. 192-197.

186. Marsching, C., et al., Imaging of complex sulfatides SM3 and SB1a in mouse kidney using MALDI-TOF/TOF mass spectrometry. Analytical and Bioanalytical Chemistry, 2011. **401**(1): p. 53-64.

187. Grove, K.J., et al., Diabetic nephropathy induces alterations in the glomerular and tubule lipid profiles. Journal of Lipid Research, 2014. **55**(7): p. 1375-1385.

188. Kaneko, Y., et al., Imaging mass spectrometry analysis reveals an altered lipid distribution pattern in the tubular areas of hyper-IgA murine kidneys. Experimental and Molecular Pathology, 2011. **91**(2): p. 614-621.

189. Mora, L.D., et al., *The effects of oral glutamine on cisplatin-induced nephrotoxicity in rats.* Pharmacological Research, 2003. **47**(6): p. 517-522.

190. Garrett, T.J. and R.A. Yost, Analysis of intact tissue by intermediate-pressure MALDI on a linear ion trap mass spectrometer. Analytical Chemistry, 2006. **78**(7): p. 2465-2469.

191. Khaselev, N. and R.C. Murphy, *Electrospray ionization mass spectrometry of lysoglycerophosphocholine lipid subclasses.* Journal of the American Society for Mass Spectrometry, 2000. **11**(4): p. 283-291.

192. Vance, J.E. and G. Tasseva, *Formation and function of phosphatidylserine and phosphatidylethanolamine in mammalian cells.* Biochimica Et Biophysica Acta-Molecular and Cell Biology of Lipids, 2013. **1831**(3): p. 543-554.

193. Zhang, L., B.L. Peterson, and B.S. Cummings, The effect of inhibition of Ca2+-independent phospholipase A(2) on chemotherapeutic-induced death and phospholipid profiles in renal cells. Biochemical Pharmacology, 2005. **70**(11): p. 1697-1706.

194. Li, Y.B., et al., Metabonomics study on nephrotoxicity induced by intraperitoneal and intravenous cisplatin administration using rapid resolution liquid chromatography coupled with quadrupole-time-of-flight mass spectrometry (RRLC-Q-TOF-MS). Rsc Advances, 2014. **4**(16): p. 8260-8270.

195. De Matteis, M.A., C. Wilson, and G. D'Angelo, *Phosphatidylinositol-4-phosphate: The Golgi and beyond (vol 35, pg 612, 2013).* Bioessays, 2013. **35**(8): p. 756-756.

196. Kuwana, H., et al., The phosphoinositide-3 kinase gamma-Akt pathway mediates renal tubular injury in cisplatin nephrotoxicity. Kidney International, 2008. **73**(4): p. 430-445.

197. Khatib-Shahidi, S., et al., Direct molecular analysis of whole-body animal tissue sections by imaging MALDI mass spectrometry. Analytical Chemistry, 2006. **78**(18): p. 6448-6456.

198. Bunch, J., M.R. Clench, and D.S. Richards, Determination of pharmaceutical compounds in skin by imaging matrix-assisted laser desorption/ionisation mass spectrometry. Rapid Communications in Mass Spectrometry, 2004. **18**(24): p. 3051-3060.

199. Rauser, S., et al., Classification of HER2 Receptor Status in Breast Cancer Tissues by MALDI Imaging Mass Spectrometry. Journal of Proteome Research, 2010. **9**(4): p. 1854-1863.

200. Deininger, S.-O., et al., MALDI Imaging Combined with Hierarchical Clustering as a New Tool for the Interpretation of Complex Human Cancers. Journal of Proteome Research, 2008. **7**(12): p. 5230-5236.

201. Benabdellah, F., et al., In Situ Primary Metabolites Localization on a Rat Brain Section by Chemical Mass Spectrometry Imaging. Analytical Chemistry, 2009. **81**(13): p. 5557-5560.

202. Moreno-Gordaliza, E., et al., MALDI-LTQ-Orbitrap mass spectrometry imaging for lipidomic analysis in kidney under cisplatin chemotherapy. Talanta, 2017. **164**: p. 16-26.

203. Baluya, D.L., T.J. Garrett, and R.A. Yost, *Automated MALDI matrix deposition method with inkjet printing for imaging mass spectrometry.* Analytical Chemistry, 2007. **79**(17): p. 6862-6867.

204. Hoesl, S., et al., Development of a calibration and standardization procedure for LA-ICP-MS using a conventional ink-jet printer for quantification of proteins in electro- and Western-blot assays. Journal of Analytical Atomic Spectrometry, 2014. **29**(7): p. 1282-1291.

205. Moraleja, I., et al., Printing metal-spiked inks for LA-ICP-MS bioimaging internal standardization: comparison of the different nephrotoxic behavior of cisplatin, carboplatin, and oxaliplatin. Analytical and Bioanalytical Chemistry, 2016. **408**(9): p. 2309-2318.

206. Kallback, P., et al., Novel mass spectrometry imaging software assisting labeled normalization and quantitation of drugs and neuropeptides directly in tissue sections. Journal of Proteomics, 2012. **75**(16): p. 4941-4951.

207. Humanes, B., et al., Cilastatin protects against cisplatin-induced nephrotoxicity without compromising its anticancer efficiency in rats. Kidney International, 2012. **82**(6): p. 652-663.

208. Garrett, T.J., et al., Imaging of small molecules in tissue sections with a new intermediate-pressure MALDI linear ion trap mass spectrometer. International Journal of Mass Spectrometry, 2007. **260**(2-3): p. 166-176.

209. Fahy, E., et al., *Lipid classification, structures and tools.* Biochimica Et Biophysica Acta-Molecular and Cell Biology of Lipids, 2011. **1811**(11): p. 637-647.